MEASUREMENT OF THE STATIC AND DYNAMIC FORCE PERFORMANCE OF A TILTING PAD JOURNAL BEARING WITH (a) STEEL-PADS AND (b) COPPER-PADS

A Thesis

by

HUSSAIN KAIZAR

Submitted to the Office of Graduate and Professional Studies of
Texas A&M University
in partial fulfillment of the requirements for the degree of

MASTER OF SCIENCE

Chair of Committee,	Luis A. San Andrés
Committee Members,	Adolfo Delgado
	Stefan Hurlebaus
Head of Department,	Andreas A. Polycarpou

May 2019

Major Subject: Mechanical Engineering

ABSTRACT

High speed turbomachinery uses tilting pad journal bearing (TPJB) to support rotor loads (static and dynamic). Over the years, continuous efforts has produced machines operating at increasing operating speeds and specific loads. Large specific loads and high shaft surface speeds increase the bearing drag power loss, pad metal temperatures, and lubricant temperature. These high temperatures pose a bearing design limit when it comes to pad material properties. Thus, experimental data presenting solely the effect of pad material on the performance of TPJBs is highly beneficial.

The thesis presents and compares the static and dynamic force performance measurements of the copper-pads bearing (C-PB) and the steel-pads bearing (S-PB). Both bearings have the same geometric configuration and differ only by pad backing material (copper vs. steel). The bearing geometry includes: five pads, 101.6 mm bearing nominal diameter, 12.3 mm pad thickness, 0.4 *L/D* ratio, ball-in-socket pivot type, 50 % pivot offset, 63.5 µm nominal bearing radial clearance (C_b) and average pad preload (m) of 0.42. The bearings operate at four shaft speeds ranging from 6 krpm (32 m/s) to 14 krpm (74 m/s) and multiple bearing specific loads ranging from (0.17 MPa to 2.1 MPa). ISO VG 32 oil, at a supply temperature of 49 ºC, lubricates the bearings under a flooded lubrication configuration.

A comparison of the performance parameters for the C-PB and the S-PB show that the steel-pads bearing shaft operates with a 37 % higher eccentricity than the copper-pads bearing. The attitude angle is low (< 10º) for both bearings thus indicating low cross-coupling destabilizing forces. The oil temperature rise in the bearings is similar with maximum difference of up to 6 ºC. Further, the drag power loss measurement show that the steel-pads bearing has a low drag power loss and is ~ 5 % less than that of the copper-pads bearing. The maximum pad temperature rise is higher for the steel-pads bearing for all the operating conditions. However, it varies depending upon operating speed and bearing specific load. The difference in temperature between the S-PB and the C-PB ranges from 5 ºC to 16 ºC over the range of operating conditions.

The thesis also presents the dynamic load characteristics of the bearing. Over the range of operating conditions, the C-PB direct stiffness K_{YY} is up to 30 % larger than the S-PB stiffness. Further, the difference in direct stiffness K_{XX} between the C-PB and the S-PB ranges from 60 % to 90%. Moreover, the static load derived direct stiffness K_{STAT} of the S-PB is ~ 25-35% smaller than the dynamic load derived stiffness K_{YY} whereas the C-PB K_{STAT} is ~ 15-30% smaller than the C-PB K_{YY}.

Similar to the stiffnesses results, the copper-pads bearing yields a high direct damping along both the loaded (C_{YY}) and orthogonal directions (C_{XX}). The C_{YY} is up to 25 % high and C_{XX} is up to 40 % higher for the C-PB. However, both bearings show high C_{XX} and C_{YY} symmetry. The virtual mass coefficients of both bearings are low (< 1.0).

DEDICATION

To my parents, siblings.

ACKNOWLEDGEMENTS

First of all, I would like to thank my fiancée, parents and siblings who were always there for me through my thick and thin and without whose support I wouldn't have come this far.

Secondly, I would like to thank my professor Dr. Luis San Andrés for advising and helping me out throughout my stay at the Turbomachinery Laboratory. His constant guidance and support helped me to complete my research study and lead me to graduate. I am glad, I had an opportunity to work under such a knowledgeable and hardworking research advisor.

Further, I would like to thank Dr. Adolfo Delgado and Dr. Stefan Hurlebaus for taking their time out for my thesis defense and being in my defense committee. I appreciate the kind nature of Dr. Delgado to help any students whether he/she works under him or not. He was always there to help the Turbo-Lab students.

Last but not the least, I would like to express my sincere gratitude to my colleague Hardik Jani who was a constant support during my stay at the Turbo-Lab. Also, I would like to thank Jonathan Toner and Rachael Bolen for all the support and help in completing the Elliott project. Moreover, heartfelt thanks to Xieuliang Lu, Tincheng Wu, Jose Barajas, Jonathan Thiele, Scott Tran, Wonbae Jung and Rasool Koosha for all their help and encouragement.

CONTRIBUTORS AND FUNDING SOURCES

This work was supervised by a thesis committee consisting of Dr. Luis San Andres (advisor) and Dr. Adolfo Delgado of the Department of Mechanical Engineering and Dr. Stefan Hurlebaus of the Department of Civil Engineering.

The experimental data was acquired with the help Turbo-Lab colleagues including Hardik Jani, Jonathan Toner and Rachael Bolen. All other analysis and written work was completed independently by the student.

This work was possible from a funding for a commercial project sponsored by Elliott Corporation.

TABLE OF CONTENTS

LIST OF FIGURES

LIST OF TABLES

NOMENCLATURE

a_{sx}, a_{sy}	Measured bearing housing acceleration along the *x* and *y* directions [m/s^2]
A_{sx}, A_{sy}	Discrete Fourier Transform of the bearing housing accelerations [m/s^2]
C_b	Bearing radial clearance [m]
C_{gr}	Groove mixing coefficient
C_{ij}	Direct and cross-coupled damping coefficients [Ns/m] $i,j=X,Y$
c_{ij}	Dimensionless damping coefficients, $c_{ij} = \frac{C_{ij}\, C_b\, \Omega}{W}$ $i,j= x,y$
C_p	Pad radial clearance [m]
c_p	Lubricant specific heat [J/Kg ºC]
C_{sxx}, C_{syy}	Structure damping coefficients along the *x* and *y* directions [Ns/m]
D	Bearing nominal diameter [m]
D_s,D_b	Socket and ball diameter [m]
D_x, D_y	Discrete Fourier Transform of the rotor-bearing relative displacements [m]
e	Shaft eccentricity [m]
E_b, E_s	Ball elastic modulus [GPa]
e_x, e_y	Shaft eccentricity along the *x* and *y* directions [m]
f_{bx}, f_{by}	Bearing reaction forces along the *x* and y directions [N]
f_{ex}, f_{ey}	Applied dynamic force along the *x* and *y* directions [N]
F_{ex}, F_{ey}	Discrete Fourier Transform of the excitation forces [N]
f_{sxx}, f_{syy}	Structure reaction forces along the x and y directions [N]
H_{ij}	Complex dynamic stiffness [N/m], $H_{ij} = \left(K_{ij} - \omega^2 M_{ij}\right) + j\left(\Omega C_{ij}\right) \quad i,j = x,y$
i	Imaginary unit [$\sqrt{-1}$]
K_{ij}	Direct and cross-coupled stiffness coefficients [N/m] $i,j=X,Y$
k_{ij}	Dimensionless stiffness coefficients, $k_{ij} = \frac{K_{ij}\, C_b}{W}$ $i,j=x,y$
K_{loader}	Static loader spring stiffness [N/m]

K_p	Calculated pivot stiffness [N/m]
K_{pad}	Bearing pad stiffness [N/m]
K_{STAT}	Bearing static stiffness [N/m]
K_{stat}	Dimensionless bearing static stiffness
K_{sxx}, K_{syy}	Structure stiffness coefficients along the x and y directions [N/m]
L	Bearing axial length [m]
m	Pad preload
μ	Lubricant viscosity [Pa s]
M_{ij}	Direct and cross-coupled virtual mass coefficients [kg] $i,j=X,Y$
m_{ij}	Dimensionless virtual mass coefficients, $m_{ij} = \frac{M_{ij}\, C_b\, \Omega^2}{W}$ $i,j=x,y$
M_s	Mass of bearing housing [kg]
N	Shaft running speed [Rev/sec]
n_p	Number of pads
ϕ	Attitude angle [degree]
P^*	Dimensionless drag power loss [W]
$P_{baseline}$	Measured drive power without the oil running through the test bearing [W]
$P_{bearing}$	Measured drive power with the oil running through the test bearing [W]
P_{drag}	Net measured power loss [W], $P_{drag} = P_{bearing} - P_{baseline}$
$P_{analytical}$	Theoretical power loss [W], $P_{analytical} = \frac{\Omega^2 D^3 L\, \mu_{eff}}{8\, C_b}\ (n_p\ \theta_p)$
$P_{estimated}$	Estimated drag power loss [W]
$\dot{Q}$	Lubricant supply flow rate [m^3/s]
ρ	lubricant density [kg/m3]
R_b	Bearing radius [m]
R_e	Reynolds Number for shear flow, $R_e = \frac{\rho\ \Omega\ R\ C_b}{\mu_{eff}}$
R_{e^*}	Modified Reynolds Number, $R_{e^*} = \frac{\rho\ \Omega\ C_b^2}{\mu_{eff}}$
R_p	Pad radius [m]
R_s	Shaft radius [m]

S	Sommerfeld Number
$T_{baseline}$	Measured torque without the oil running through the test bearing [Nm]
$T_{bearing}$	Measured torque with the oil running through the test bearing [Nm]
T_{DE},T_{NDE}	Oil discharge temperature at the drive end and the non-drive end [ºC]
$T_{discharge}$	Arithmetic average of the drive end and non-drive end discharge oil temperatures [ºC]
T_{in}	Oil supply temperature [ºC]
T_{pad}	Measured sub-surface pad temperature [ºC]
v_s,v_b	Socket and ball poisson ratio
W	Static load [N]
x_b, y_b	Bearing center coordinates [m]
x_s,y_s	Shaft center coordinates [m]
α_{vis}	Viscosity coefficient [1/ºC]
δ	Pivot displacement [m]
δ_p	Calculated pivot deflection [m]
Δx, Δy	Relative displacements between the rotor and the bearing pad [m]
$\Delta\dot{x}$, $\Delta\dot{y}$	Relative velocities along the x and y directions [m/s]
$\Delta\ddot{x}$, $\Delta\ddot{y}$	Relative acceleration along the x and y directions [m/s^2]
$\acute{\eta}$	Ratio of the measured steel-pads bearing and copper-pads bearing pad-pivot stiffness
θ	Dimensionless pad defect temperature, $\theta = \frac{T_{pad}-T_{in}}{T_{discharge}-T_{in}}$
$\Delta\theta$	Difference in θ; $\Delta\theta = \theta_{max} - \theta_{min}$
θ_p	Pad arc length [degree]
ψ	Ratio of the estimated power loss and measured power loss
Ω	Shaft rotating frequency [Hz,rpm]
ω	Excitation frequency [Hz]
κ_T	Pad thermal conductivity [W/(m ºC)]

ASTM	American Society for Testing and Materials
CC	Cold clearance
C-PB	Copper-pads bearing
Cu	Copper
DE	Drive-End
DFT	Discrete Fourier Transform
DFT	Discrete Fourier Transform
HC	Hot clearance
LBP	Load between Pad
LEG	Leading-Edge-Groove
LOP	Load on Pad
NDE	Non-Drive-End
PEEK	Polyether-Ether-Ketone
PTFE	Poly-Tetra-Fluro-Ethylene
S-PB	Steel-pads bearing
TEHD	Thermo-Elasto-Hydrodynamic
THD	Thermo-Hydrodynamic
TPJB	Tilting Pad Journal Bearing

1. INTRODUCTION

A fluid film bearing is a component of rotating machinery such as gearboxes, pumps, turbines, compressors and generators. Apart from providing lateral rotor support, bearings have a significant impact on the rotordynamics and stability of the rotating machine. The operating speed of many high speed machines is usually above the first natural frequency of the rotor-bearing system and bearings could potentially generate destabilizing forces due to a phenomenon known as oil whirl/oil whip [1]. A tilting pad journal bearing (TPJB) geometry delivers an inherent stable configuration compared to a fixed geometry bearing. TPJB have low or insignificant cross-coupling stiffnesses when installed as under a load-on-pad (LOP) or a load-between-pad (LBP) configurations [2]

Figure 1 displays a typical five-pad tilting pad journal bearing with a load-on-pad (LOP) configuration. The shaft rotating with speed (Ω) pushes the lubricant into the converging wedge between the shaft and the bearing pads to generate a hydrodynamic pressure field which supports the rotor load (W). A pivot allows each pad to tilt such that the film induced pad force passes through a pivot and the net moment is zero. Thus, when operated under a LOP or a LBP the tilting motion of the pads reduces the generation of cross-coupling destabilizing forces and eliminates the chance of an oil whirl or an oil whip instability [1].

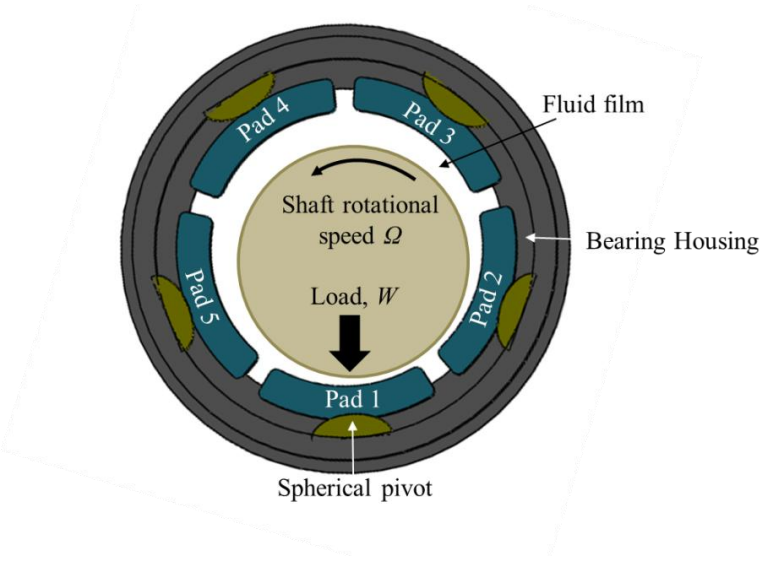

Figure 1 Schematic view of a five-pad, spherical pivot tilting pad journal bearing.

Depending upon the application, tilting pad journal bearings encounter various design configurations. Refs. [3-6] report that the static and dynamic properties of TPJBs are a strong function of bearing clearance[1] (C_b), pad preload[2] (m), shown in Figure 2, load configuration, number of pads and bearing length to diameter ratio (L/D). Figure 3 displays three common types of tilting pads journal bearing: a spherical pivot (ball-in-socket), a rocker-backed, and a flexure pivot. The main purpose of the pivots is to ensure or allow the necessary tilt of the pads so that the net fluid film reaction force passes through each pivot. As shown in Figure 3 (a), a spherical pivot allows the pad to tilt along both the axial and circumferential directions. A rocker-backed pad pivot, see Figure 3 (c), shows tilt due to line contact about the pivot. Thus, a rocker-back pivot allows rotation in the circumferential direction only. Experimental results from Wygant [7, 8] and Coghlan [9] show a small positive shaft attitude angle and a small cross-coupling stiffness in the tested spherical pivot bearings. Wygant [7] states that the sliding friction between a pad and its pivot hinders the tilting and generates a positive (13°-33°) attitude angle. The flexure pivot bearing, as shown in Figure 3 (b), has a slender structural web that enables both radial and rotational stiffnesses to support the rotor load and allow the necessary pad tilt [10]. Thus, a flexure pivot does produce a reaction moment about the pivot. The major advantage of a flexure pivot bearing is that it eliminates wear and tear due to pivot friction and reduces the need for tight manufacturing tolerances.

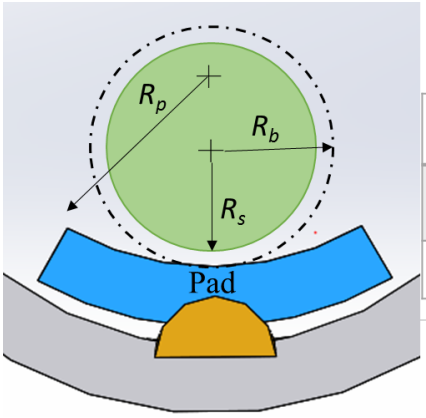

Bearing Clearance (C_b)	Bearing Radius (R_b)-Shaft Radius (R_s)
Pad Clearance (C_p)	Pad Radius (R_p)- Shaft Radius (R_s)
Preload (m)	1- C_b/C_p

Figure 2 Schematic view of tilting pad and rotor defining bearing clearance (C_b), pad clearance (C_p) and bearing preload (m).

[1] Bearing Clearance (C_b) = Bearing Radius (R_b) – Shaft Radius (R_s)
[2] The bearing preload (m) = (C_p –C_b)/C_p, where the pad clearance (C_p) = Pad Radius (R_p)–Shaft Radius(R_s)

Besides pad configuration and disposition, the performance of a tilting pad bearing depends on its geometry, lubricant viscosity and density, shaft rotational speed (Ω) and static shaft load (W). The static load (W) capacity of the bearing depends on the lubricant viscosity which is a strong function of the lubricant film temperature which increases with the shear induced drag power loss in the bearing [11]. The temperature change of the film induces a thermal gradient in the bearing pads and changes the geometric features of the bearing elements (pads, pivots, bearing housing). As discussed by Simmons [6] in 1994, changes in geometric parameters of a bearing highly affect the static performance parameters such as pad temperature, bearing clearance (C_b) depicted in Figure 3, drag power loss and shaft static eccentricity. Dmochowski [4] further discusses the effects of changes in the bearing geometric parameters on the dynamic force coefficients of a TPJB.

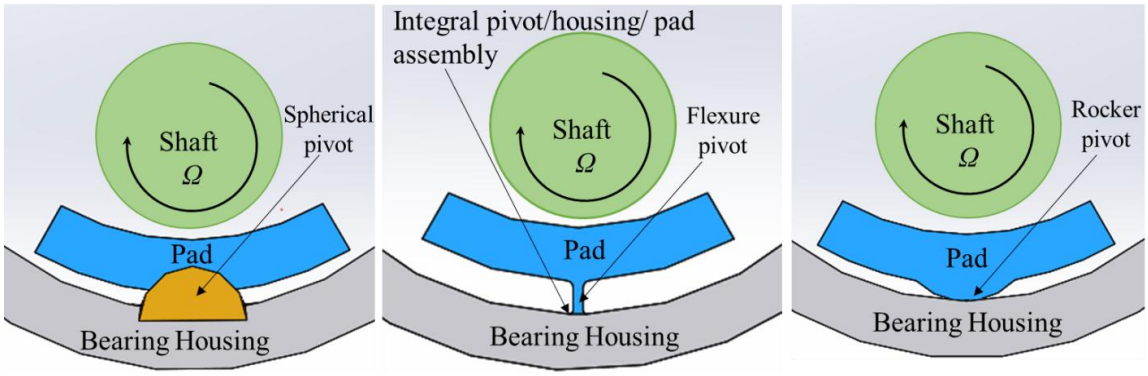

Figure 3 Schematic views of (a) spherical pivoted pad (left), (b) flexure pivoted bearing (middle) and (c) rocker pivoted bearing (right).

Apart from bearing geometry, a pad backing material also affects the bearing operating temperature. The pad babbitt material has limitations of compressive load and temperature [12]. Heat generated through shear drag from the rotor should be carried by the lubricant and also conducted through the pads to keep the babbitt temperature below its material failure limit. Distinct pad materials have different thermal conductivity which affect the heat transfer rate and consequently the ensuing pad temperature [13]. Thus, experimental investigations to study the effect of pad material on a TPJB forced performance, static and dynamic, are vital.

2. OBJECTIVE AND TASKS

The main objective of the research is to experimentally investigate and compare the static and dynamic force performance of a five pad tilting pad journal bearing with pads made of (a) steel and (b) copper. The bearings differ by pad material with one having steel-backed pads and the other having copper-backed pads. All the other geometric parameters including the lubricant (ISO VG 32) are identical for both bearings. Table 1 and 2 detail the bearing geometric parameters and test matrix, respectively. The comparison of the bearing with either steel or copper backed pads will be made through a series of performance parameters noted below. The main tasks of the study are:

- To measure and compare the static load characteristics of the bearings. These are drag power loss, shaft eccentricity and attitude angle, oil exit temperature, and bearing pads temperatures. The operating conditions include shaft speed ranging from 6,000-14,000 rpm (32 to 75 m/s), specific load from 0.69 to 2.07 MPa, speed-dependent oil flowrate at a constant inlet oil (ISO VG 32) temperature of 49°C.
- To measure the dynamic force coefficients of the test bearings over a range of excitation frequencies (10- 250 Hz). The dynamic parameters include bearings stiffness, damping, and virtual mass coefficients.

To compare the experimental results against the bearing performance prediction from XLTPJB® [14] bearing model.

Table 1 Test bearing geometric parameters and operating conditions

Number of pads	5
Shaft diameter, D	101.590 ± 0.005 mm
Bearing axial length, L	40.64 mm
Pad thickness	12.3 mm
Babbitt thickness	~ 0.8 mm
Pad arc length	63°
Pad material	Steel-backed Babbitt/ Copper-backed Babbitt

Table 1 continued

Pivot type	Ball-in-Socket
Pivot offset	50%
Preload	0.39-0.45
Load Configuration	Load-On-Pad
Nominal pad radial clearance (C_p)	112 µm
Nominal bearing radial clearance (C_b)	63.5 µm
Lubricant supply configuration	Orifices/Flooded
Oil Type	ISO- VG 32
Oil inlet temperature	49℃ (120 °F)

Table 2 Test matrix for proposed research (*)

Speed (rpm)→	**6000**	**9000**	**12000**	**14000**
Shaft surface speed	32	48	64	74
Load (MPa) ↓				
0.69	☑	☑	☑	☑
1.03	☑	☑	☑	☑
1.38	☑	☑	☑	☑
1.72	☑	☑	☑	
2.07	☑	☑	☑	

☑ = static results only

☑ = static + dynamic results

(*) removed flow rate as per sponsor requirement

3. PAST LITERATURE REVIEW

Over the years TPJBs have under gone steady design improvements to enable operation at high shaft surface speeds and under ever increasingly large specific loads. Modern bearings are designed to have a smaller footprint, to operate with a minimum of lubricant flow, and to ensure reduced drag power losses. The following literature review discusses the experimental research conducted to date to advance tilting pad journal bearing performance. Table 3 summarizes the most notable experimental works relevant to this thesis i.e. papers having similarity in bearing geometry and operating conditions were selected. The table lists bearing geometry, operating conditions and pad material of the test bearings used to assess the effect of bearing geometry preload (m), bearing clearance (C_b), pivot offset, bearing slenderness ratio (L/D) and pivot types on the static and dynamic properties of the bearing.

Table 3 Past experimental work on TPJBs detailing the influence of geometry on bearing static and dynamic force performance[3].

	Fillon et al. [5] 1992	Dmochowski and Brockwell, [11] 1993	Simon and Dixon, [6] 1994	Wygant et al.[7, 8] 1999	Pettinato and De Choudhury, [15, 16] 1999	Wygant et al. [17, 18] 2004	Hageman n et al. [19, 20] 2013	Coghlan et al.[21] 2017	Present study
Number of pads	4	**5**	**5**	**5**	**5**	**5**	**5**	4	5-Pad
Pivot type	Rocker	x	Rocker	**Ball-in-Socket** & Rocker	**Ball-in-Socket** & Rocker	Rocker	Rocker	**Ball-in-Socket**	Ball-in-socket
Load orientation	LBP	LBP	**LOP** & LBP	**LOP**	LBP	**LOP** & LBP	LBP	LBP	LOP
Pad arc length (deg)	75	54	**60**	**60**	**65 &55.5**	52	56	72	63
Preload, *m*	0.47 & 0.68	0,0.2,0.4 & 0.6	0.52 & 0.22	0.35 & 0.30	0.35 &0.35	-0.33 – 0.54	0.23	0.3	0.43
Pivot offset	**50**	x	**50**	**50**	**50**	**50**	60	**50**	50
Mean dia. bearing clearance, C_b (mm)	0.158 & 100	0.127	0.23 & 0.36	x	0.193	0.163	0.6	0.18	0.13
Length, *L* (mm)	70 & 69.7	57 & 35	80	52.5	38.1	52.5	350	61	40.6
Shaft diameter, *D* (mm)	100 & 99.6	76	200	70	126.9	70	500	101.6	101.6
L/D ratio	0.7	0.75 & 0.46	0.4	0.75	0.3	0.75	0.7	0.7	0.4
Pad lining	Babbitt	Babbitt	Babbitt		Babbitt		Babbitt	Babbitt	Babbitt
Backing material	**Steel**	x	x	Bronze &**Steel**	**Steel**	**Steel**	x	Steel	**Steel & Copper**
Lubrication method	**Flooded**	**Flooded**	**Flooded**	**Flooded**	**Flooded**	**Flooded**	Spray-bar, **Flooded**	**Flooded**, LEG, SBB and SB	Flooded
Inlet Lubricant Temperature (°C)	40	**50**	43	x	**49**	52	50	50	49
Lubricant	**ISO VG 32**	**ISO VG 32**	**ISO VG 32**	**x**	**ISO VG 32**	**ISO VG 32**	**ISO VG 32**	ISO VG 46	ISO VG 32

[3] Bearing design parameters and operating conditions similar to the present study are displayed in red color

Table 3 continued

	Fillon et al. [5] 1992	Dmochowski and Brockwell, [11] 1993	Simon and Dixon, [6] 1994	Wygant et al.[7, 8] 1999	Pettinato and De Choudhury, [15, 16] 1999	Wygant et al. [17, 18] 2004	Hageman n et al. [19, 20] 2013	Coghlan et al.[21] 2017	Present study
Max. operating surface speed (m/s)	21	14.3	105	8	72	8	**79**	**85**	85
Max. specific load (MPa)	1.4	1.5	4.14	0.7	1.7	0.7	**2.5**	2.9	2.1
Comparison of pad backing material	x	x	x	✓	x	x	x	x	✓

In 1985 Tripp and Murphy [22] conduct an early research on TPJBs to measure rotor eccentricity for operation at speed ranging from 300 to 3000 rpm (10 m/s max.) and a unit load[4] ranging from 3 kPa to 63 kPa. The speed and load test points combination correspond to Sommerfeld[5] numbers (*S*) between 0.2 and 0.3. The results show that an increase in *S* produces a decrease in shaft eccentricity. Further, comparison of calculated and measured eccentricities shows a difference of 4 % to 15 %

In 1992, Fillon et al. [5] report test results for two four-pad steel-backed TPJB having a diameter of 100 mm, 0.7 *L/D* ratio, and preloads of 0.47 and 0.68. The main aim of the tests is to study the effect of pad preload (*m*) on bearing performance. The operating conditions include rotor speed from 0-4 krpm (max. shaft speed 21 m/s) and unit loads up to 1.4 MPa. The test results show that an increase in pad preload increases the pads maximum temperature and displaces the maximum pad temperature location towards the center of a pad. The pad temperature shows a ~ 12 °C temperature rise with an increase in pad preload from 47 % to 68 %.

In 1994, Simon and Dixon [23] extend early work of Fillon et al. [5] to test a 200 mm diameter five-pad babbitt lined TBJB having 0.4 *L/D* ratio, 0.52 and 0.22 preload (*m*), and 0.23 mm and 0.36 mm diametrical clearances. Compared to test results in Ref. [5], the maximum shaft operating surface speed increases to 105 m/s and unit load up to 4.14 MPa. Within the limits of the test data, the change in pad preload does not significantly alter the pads maximum temperature or drag power loss in the bearing. A change in bearing clearance has an insignificant impact on bearing performance, yet the pads' maximum temperature drops by 8°C and the power loss by 5 kW. A change in load direction affects the pads temperature significantly; for operation at 75 m/s and 2.76 MPa and LOP configuration, the maximum pad temperature is 10°C hotter than for the LBP configuration.

In 1995, Dmochowski and Brockwell [4] discuss dynamic load testing of two 0.076m diameter centrally pivoted five-pad tilting pad bearing. One bearing has 0.46 *L/D* ratio and

[4] Unit Load= *W/(L*D)* where *W*=static bearing load, *L*= bearing pad length and *D* = bearing diameter

[5] The Sommerfeld number is a dimensionless number used in bearing design, i.e. $S = \frac{\mu N L D}{W} \left(\frac{R}{C_b}\right)^2$ where μ= lubricant viscosity, *N*= shaft speed.

m=0 while the other bearing has 0.75 *L/D* ratio with pad preload ratios *m* = 0, 0.2, 0.4 and 0. The dynamic load test results show a slight change in direct stiffness with a change in preload; At low speeds (900 rpm to 2000 rpm) the direct damping coefficient decreases by 60% with the increase in pad preload. Further, keeping all the operating conditions constant, both theoretical predictions and experimental results show that an increase in *L/D* ratio from 0.46 to 0.75 decreases the bearing direct stiffnesses.

In 1999 Wygant and et.al [7, 8] present comparisons of static and dynamic load test results for 70 mm spherical pivot TPJB and a rocker backed pivot TPJB. Both bearings have 50% pivot offset, 0.75 *L/D* ratio, preload *m*=0.32, and pad radial clearance C_p equal to 113 µm. The operating condition includes shaft speed ranging from 900 to 2,250 rpm (max. shaft surface speed is 8 m/s) and unit loads from 0.06 MPa to 0.7 MPa. For operation at *S*=0.1 to 2.0, the shaft follows a straight locus for the bearing with a rocket backed pivot. Conversely, for the spherical pivot bearing, the attitude angle changes from 13° to 33°. For both bearings, the dynamic load test results show similar trends for both the direct stiffness and damping coefficients. Over the range of operating speeds, the cross-coupling stiffnesses for the rocker-backed bearing are very small (~ < 20% of direct stiffness) and insignificant. For the spherical pivot bearing, the cross-coupling stiffness (K_{xy} and K_{yx}) have the same sign for operation at low Sommerfeld number but the sign changes for *S*>0.8. The authors state the pivot type is the primary reason for the detected cross-coupling stiffnesses. The pad tilt in the spherical pivot (ball-in-socket) depends on the sliding friction (0.4 coefficient of friction) between ball and socket whereas for the rocker-pivot pad it relies the rolling friction (0.006 coefficient of friction). The authors present a hypothesis that an increased sliding friction hinders a pad tilt for the spherical pivot bearing and thus induces the cross-coupling stiffnesses.

In 1999, Pettinato and De Choudhury [15, 16] present static and dynamic load test results of a key-seat[6] TPJB and a spherical pivot TPJB. Both bearings have a diameter = 127 mm, 0.3 *L/D* ratio, 0.19 mm diametrical bearing clearance, 0.35 preload, and steel pad material. The operating conditions include shaft speed of 5, 7 and 12 krpm (max. shaft

[6] The bearing pad rest on a key-seat pivot forming a line contact between the pad and pivot. Similar to a rocker-pivot bearing, key-seat bearing pads can tilt in circumferential direction only

surface speed 80 m/s) with unit loads from 126 kPa to 1,724 kPa. The test results show that the spherical pivot bearing has higher drag power loss and higher eccentricity (maximum 53 % higher) and produce slightly greater pads temperature compared to the key-seat bearing. The attitude angles are positive for both bearing types though the spherical pivot bearing shows a higher angle indicating presence of cross-coupled forces. The dynamic load test results show that both the horizontal and vertical stiffnesses and damping coefficients of the key seat bearing are higher than those of the spherical seat bearing. The authors also measure the pivot stiffness by loading the shaft (without rotation) and recording the deflection at the bearing centerline. The pivot stiffness magnitudes are identical for both the key-seat and spherical pivot. Note, the pivot stiffness is three to four times greater than the measured film stiffnesses

In 2004, Wygant and et al. [17, 18] conduct experiments to study the effect of pad preload on the static and dynamic load characteristics of a TPJB. The tests include multiple 70 mm diameter five-pad tilting pad journal bearings having 0.75 *L/D* ratio, 0.5 pivot offset, assembled radial clearance of 81 µm, and rocker-backed steel-pads. The bearings pads have a pad preload (m) ranging from -0.33 to 0.540. The operating conditions include shaft speeds of 900, 1,650 and 2,250 rpm (max. shaft surface speed 8 m/s), and unit loads ranging from 36 kPa to 726 kPa for both LOP and LBP load configurations. Over the operating range, the pad temperature rise is relatively insignificant. Considering the uncertainty in measurements, the pads' preload moderately affects the shaft eccentricity as it slightly decreases with the increase in preload. Moreover, the attitude angle results show negligible dependency on pad preload, and small values indicate negligible cross-coupling stiffness. The authors use synchronous force excitations (15, 27.5 and 37.5 Hz) to acquire the dynamic force coefficients. For both LOP and LBP configurations, the direct stiffness (K_{xx} and K_{yy}) decrease mildly with a decrease in preload. The effect of preload and load direction on the bearing cross-coupling stiffness and damping coefficients is negligible and the coefficients' magnitudes are significantly lesser than the direct stiffness and damping coefficients.

In 2013, Hagemann et al. [19, 20] report test results for a large 0.5m diameter five pad tilting pad journal bearing loaded in a load between pad configuration. The *L/D*=0.7 bearing has a *m*=0.23 pad preload and 60 % pivot offset. The operating conditions include

a maximum shaft surface of 79 m/s and unit loads between 1.0 and 2.5 MPa. The film thickness and pressure profile results from an advanced predictive code show good agreement with the measured data. To extract the dynamic force coefficients, the authors excite the system with both synchronous and asynchronous frequency (ω) resulting in forced excitations ratios (excitation frequency/shaft speed frequency) of 1.0 to 2.0 while measuring the film pressure around the bearing. The differences between the experimental and numerical predictions go up to 70 % for the direct stiffness coefficients and 40 % for the damping coefficients. For the majority of the test cases, the computational results over predict the stiffness coefficients and under predict the damping coefficients. The authors conclude the discrepancy in the data to be the result of post-processing errors, neglecting the pad inertia effects, and the uncertainty in the data acquisition.

In 2017 Coghlan and Childs [21] present static load test results of a four-pad, steel-backed, spherical pivot TPJB supplied with distinct lubrication feed methods: single-orifice, leading-edge-groove (LEG), spray-bar (SB) and spray-bar blocker (SBB). The bearing is the same during the entire test program: 50% pivot offset, 0.6 *L/D* ratio, and 101.6 mm diameter. The shaft operates at a maximum shaft surface speed of 85 m/s and the bearing unit loads are up to 2.9 MPa. With a direct lubrication and an evacuated housing, the test results show a maximum pad temperature reduction of 13°C for a spray-bar feed, 14°C for LEG feed, and 10°C for spray-bar blocker feed. Coghlan and Childs compare the experimental results against prediction using XLTPJB® [14]. Compared to measured data, predicted results yield higher temperatures at both the trailing and leading edges of a pad and lower temperatures at the loaded pad 75% arc length position. The maximum temperature difference between the predicted and measured temperature is 14°C.

3.1 About pad materials

Typically (compressor) bearing pads have a 0.5-1.5 mm layer of white metal alloy (Babbitt) [24]. Babbitt or white metal has excellent corrosion resistance, embedability, and anti-seizure properties. In case of any failure or loss of lubricant the babbitt layer melts and protects the shaft. A bearing pad surface coated with tin or lead based babbitt have a temperature limitation [12]. Table 4 shows the material composition, load capacity and melting temperature of a commonly used ASTM B-23 white metal alloy (babbitt). Based on

the material composition, the melting temperature of a babbitt ranges from 223°C to 240°C. But depending upon the operating load and pad temperatures for safe operation, the babbitt temperatures should be well below the material yield point.

Since at a high temperature a babbitt layer tends to creep and loses its compressive strength, the maximum allowable temperature limit of a bearing is kept below 160°C for design and operation purposes [12]. Further, for safety reasons, bearing manufacturers choose to set the continuous operation temperature limit to 130°C.

Drag power losses in a hydrodynamic bearing largely influence the pad temperature rise. Keeping all other operating parameters constant an increase in shaft speed increases the drag power loss to increase the bearing pads temperatures. For an identical pad geometry and bearing operating condition, the pad material conductivity affects the temperature across the bearing pad. The heat flow transfer across the pad is directly proportional to the thermal conductivity of the pad. Having a high thermal conductivity will result in a large heat flow transfer rate and will consequently lower the pad temperature. Table 5 details material properties of some of the commonly used pad backing and facing materials. Copper and steel are widely used as pad backing material in TPJBs. As shown in the table, compared to steel, copper has a high thermal conductivity (324 W/m k), thus heat flow through a copper pad would be easier than in a steel pad thus resulting in lower pad temperatures. Figure 4 shows the pad maximum temperature vs. surface speed of a 267 mm diameter eight shoe tilting pad thrust bearings. The bearing operates at a unit load of 3.0 MPa and surface speed ranging from 15 m/s to 135 m/s. The figure clearly shows the steel pad temperature is higher than in a chrome-copper alloy pad. The maximum temperature difference is ~20°C for operation at a surface speed of 85 m/s.

Table 4 Composition and material properties of commonly used ASTM-B-23 white metal alloy (babbitt) [25].

ASTM B-23 Alloy No.	Nominal Alloy (Babbitt) composition %			Yield point MPa		Melting point °C
	Tin	Antimony	Copper	@ 20 °C	@ 100 °C	
1	91	4.5	4.5	30	18	223
2	89	7.5	3.5	42	21	241
3	84	8.0	8.0	46	22	240

Table 5 Material properties of commonly used pad backing and liner materials stated in Ref. [26, 27].

	Steel (AISI 4140)	Chromium Copper	Babbitt	Polytetrafluroethylene (PTFE)
Young modulus	205	117	52	0.5
Poisson ratio	0.29	0.3	-	-
Density (kg/m^3)	7,861	8,885	7,470	2,200
Thermal expansion	12.2 x 10^{-6}	17.6 x 10^{-6}	-	115 x 10^{-6}
Thermal	42.6	323.6	51.9	0.25

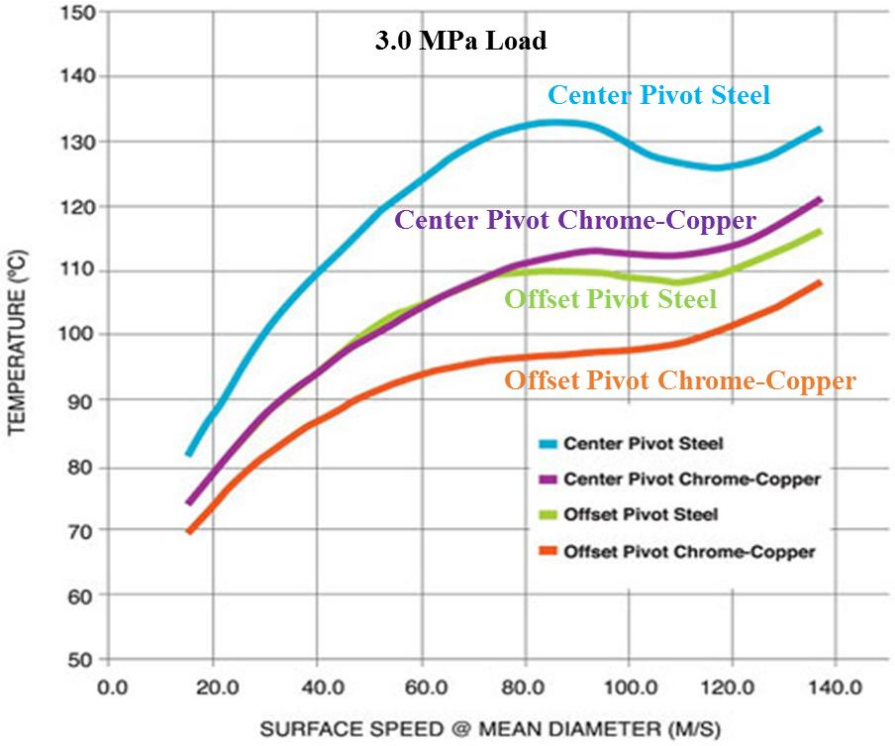

Figure 4 Reprinted from https://www.kingsbury.com/how-to-estimate-babbitt-temperature [28]. Temperature of steel and chrome-copper alloy pads (unknown Babbitt thickness) for operation at surface speed ranging from 15 m/s to 135 m/s.

Over the years, an increasing demand for high power, high speed turbomachinery has pushed industry to find ways to reduce pad temperatures so that the bearings can run at even higher surface speeds. Refs. [4-22] discusses several test results on the influence of bearing geometry (preload, bearing clearance, load configuration, pivot offset) on the pads temperatures. Table 6 summarizes the scant past experimental work conducted to solely study the effect of pad material on TBJB performance.

Table 6 Past experimental work on TPB detailing the influence of pad backing and facing material on static force performance of the bearing[7].

	Gardner [29] 1975	Mikula [30] 1988	Bouchoule et al. [31] 1995	Edney [32] 1995	Glavatskih [33] 2003	J.Nicholas [13] 2003	Zhou et al. [34] 2015	Present study
Bearing Type	Thrust	Thrust	Journal	Journal	Thrust	Journal	Thrust	Journal
Number of pads	6	6	**5**	4 **& 5**	6	6	8	5-Pad
Pivot type	x	x	**Ball-in-Socket** & Rocker	Rocker	**Spherical**	**Ball-in-Socket**	x	Ball-in-socket
Load orientation	x	x	LBP	LBP	x	X	x	LOP
Preload, *m*	x	x	x	0.122-0.433	x	X	x	0.43
Pivot offset	**50** & 60	x	**50**, 55 & 60	**50**	60	65	60	50
Mean dia. bearing clearance, C_b (mm)	x	x	0.29	0.152-0.302	x	X	x	0.13
Length, *L* (mm)	x	x	160	76.2 & 95.3	x	152.4	x	40.6
Bearing inner dia. (mm)	76	133	*N/A*	*N/A*	114.3	*N/A*	152	*N/A*
Bearing outer dia. (mm)	152	267	*N/A*	*N/A*	228.6	*N/A*	279	*N/A*
Shaft diameter, *D* (mm)	x		160	**101.6** & 127	X	152.4	**101.6**	101.6
Pad thickness (mm)	x	31.8	22	x	28.58 (1.5 mm PTFE)			
Pad facing material	Babbitt & Cu-Pb	See Table 7	Babbitt	Babbitt	Babbitt & PTFE	Babbitt	Babbitt & PEEK	Babbitt
Backing material	**Steel**, Cu & Al	See Table 7	Steel & **copper-bronze**	Steel & **copper**	**Steel**	**Chrome-copper**	Steel	**Steel & Copper**
Lubrication method	**Flooded**	**Flooded**	**Flooded**	**Flooded**	**Flooded**	Evacuated, spray-bar blocker, bypass cooling	Direct lubrication	Flooded
Inlet oil temperature (°C)	**49**	**47**	**50** & 72	**49**	**50**	**48**	**49**	49

[7] Bearing design parameters and operating conditions similar to the present study are displayed in red color.

Table 6 Continued

	Gardner [29] 1975	Mikula [30] 1988	Bouchoule et al. [31] 1995	Edney [32] 1995	Glavatskih [33] 2003	J.Nicholas [13] 2003	Zhou et al. [34] 2015	Present study
Lubricant	**ISO VG 32**	**ISO VG 32**	**ISO VG 32**	**ISO VG 32**	ISO VG 46	X	**ISO VG 32**	ISO VG 32
Max. operating surface speed (m/s)	95.5	146	100	93	36	128	124	85
Max. specific load (MPa)	3.5	14.83	3.5	.46	2	3.2	16.2	2.1
Comparison of pad backing material	✓	✓	✓	✓	✓	X	✓	✓

In 1975 Gardner [29] conducts experiments on a tilting pad thrust bearing with pads made of various materials and compares their performance. The materials are babbitt on a steel pad, Cu-Pb on a steel pad, babbitt on a copper pad, and solid aluminum pads. The test bearings have six pads, 152 mm outer diameter, 76 mm inner diameter, and 116 cm^2 of net surface area. The operating conditions include a maximum shaft speed of 12 krpm (max. surface speed is 96 m/s) and a unit load of 3.5 MPa. The comparison of pads' maximum temperature at 10 k rpm and 3.5 MPa show that the babbitt-on-copper pad bearing operates ~ 11°C cooler than the babbitt-on-steel pad bearing. As shown in Table 5, copper having a high thermal conductivity of 324 W/m K compared to 43 W/m K for steel leads to an easier heat flow and lower pad temperatures.

In 1988 Mikula [30] conducts a similar study and tests a series of six-pad tilting pad thrust bearings having 267 mm OD, 133 mm ID, and 32 mm of pad thickness. The shaft operating speed is max. 14 krpm (shaft surface speed is 146 m/s), and the maximum applied unit loads is 4.83 MPa. The bearings' material includes carbon steel, 70% copper+lead+tin, 98% copper+chromium, and 99% copper+silver. Similar to Gardner is test results [29], as shown in Table 7, the copper-backed pads having high thermal conductivity operate cooler than the steel backed pads. At a low specific load (0.69 MPa), the maximum temperature difference between the steel-pads and copper-pads bearing is 10 °C. Note the difference in pad temperatures increases with an increase in load and shaft speed. For operation at 12,000 RPM (126 m/s) and 4.83 MPa, the copper-pads bearing operates 35 °C cooler than the steel pad bearing.

Table 7 Thermal conductivity of TBJBs' pad facing and backing material tested by Mikula [30].

Test Bearing #	Material		Thermal Conductivity W/m K	Tensile Strength MPa	Pad Thickness mm
	Pad backing material	Pad facing material			
1.	Low Carbon Steel	Babbitt	52	379.5	32
2.	70% Copper +	Not	41	165.6	32
3.	98%	Babbitt	322	365.7	32
4.	99 % Copper +Ag+	Babbitt	389	248.4	32

In 1995, Bouchoule et al. [31] present extensive experimental results on the pads' temperatures of three five-pad tilting pad journal bearings, shown in Table 8, having 0.16

m diameter, 1.0 *L/D* ratio, and 22 mm pad thickness. Bearings A and B have steel backed pads with 50% and 55% pad pivot offset and rocker back pivots. Bearing C has copper-bronze alloy backed pads: All pads have a 60% offset and rest on spherical pivots. The test setup operates from 2.7 krpm to 12 krpm (max. shaft speed 100 m/s) with unit load ranging up to 3.5 MPa. Comparison of test results show a maximum pad temperature difference between bearing A and B to be 15°C at 100 m/s and 3.5 MPa. This indicates that a 5% offset difference can lead to a large temperature difference at high speed and load operating conditions. Moreover, compared to bearing A, bearing C (copper-backed) pads' temperature differ by 21 °C at the same operating condition. The temperature difference could be the result of pad material, as copper has high thermal conductivity (324 W/m k) compared to steel pad (43 W/ m k) but as shown in Table 8, bearing C differs by bearing A in terms of pivot offset (0.6 vs 0.5), pad material (copper vs steel) and pivot type (spherical vs rocker). Thus, the temperature difference cannot be solely attributed to just one parameter. At a shaft surface speed > 90 m/s, the authors also observe a reduction in pad temperature indicating a change in flow regime from laminar to turbulent. Further, the authors compare experimental results to predictions. Predictions using only a thermal deformation (THD) model do not produce adequate bearing performance results. Including both the elastic and thermal deformations (TEHD) yields results comparable to the experimental data.

Table 8 Pad material, pivot type and pivot offset for bearings tested by Bouchoule et al. [31].

	Pivot	Pad material	Pivot offset
Bearing A	Rocker back	Steel	50 %
Bearing B	Rocker back	Steel	55 %
Bearing C	Spherical	Copper-bronze	60 %

In 1999 Edney [32] presents experimental results investigating the effect of oil flowrate, bearing geometry, bearing clearance, shaft speed and pad material on the static performance parameters of multiple TPJBs. The bearings include four and five pad assemblies having spherical pivots, 101.6 mm and 127 mm shaft diameter and 0.5 and 0.75 *L/D* ratios. The bearings operate at a maximum shaft surface speed of 93 m/s and under a specific load of 460 kPa. Within the limits of the experimental data, for any operating

condition, there is an optimum value for oil flow rate below which the pad temperature increases and above which the drag power loss increases. Similar to Bouchoule et. al results [31], the copper-backed pad experiences a lower temperature and power loss at high speed as compared to the steel pad bearing. At any operating point, the copper-pads run cooler than the steel-pads. The maximum pads' temperature difference between copper and a steel pad is ~ 10 ℃ at 13 krpm (86 m/s shaft surface speed). Since copper has high thermal conductivity than steel, thus heat transfer through copper-pads would be larger than steel pad resulting in lower pad temperatures of the copper-pads. But the author uses a copper-pad bearing having a slightly larger clearance (208 µm), compared to a 180 µm clearance for the steel-pads. Thus, for this test, a large temperature difference between steel and copper pad does not solely depends on the pad material.

To study the effect of a tilting pad bearing pad facing material on pad temperatures and power loss, Glavatskih [33] in 2003 conducts experiments on self-equalizing tilting pad thrust bearings with a metal babbitt and a polytetrafluroethylene (PTFE) composite liner. The test bearings include six pad thrust bearings with 229 mm outer dia., 114 mm inner dia., 60 % pivot position, and spherical type pivot. The pads are 28.6 mm thick with ~ 1.5 mm of PTFE composite coating. The operating conditions include a maximum static load of 2 MPa, and shaft speed ranging from 1,500 rpm to 3,000 rpm (max. shaft surface speed 36 m/s). Thermocouples placed 4mm below the PTFE surface and 3mm below the babbitt layer record pad temperatures of the bearings. As shown in Table 5, with a thermal conductivity of just 0.5 W/(m K) PTFE shows good insulating properties compared to metal babbitt (52 W/m K). Test results show PTFE lined pads have low temperatures compared to babbitted pads. The maximum pads' temperature difference between the two bearing pad is ~ 28°C. Moreover, along the circumference of a pad (0 to 50º arc length), there's negligible (~1°C) temperature difference for PTFE-bearings. Thus, high insulation and a negligible temperature gradient along the circumference of the pad eliminates the problem of thermal crowning that can lead to pad wiping[8] and a reduction in bearing load capacity.

[8] Rubbing or smearing of bearing pad due to insufficient lubrication, excessive load during start-up, misalignment or operational overload.

Further, In 2003 Nicholas [13] discusses the development and application of spherical-seated TPJBs supplied with a spray-bar. The pads have a by-pass cooling[9]. The static load and shaft surface speed range from 2.4 to 3.2 MPa and 76 to 128 m/s, respectively. The main aim of the work is to describe a series of design changes towards reducing pads temperatures. Considering the change in pad material, the author details the usage of 150 mm diameter bearing having chrome-copper-pads in a high speed gear box. However, the bearings also have spray-bar blockers, evacuated bearing housing, 65 % pivot offset and by-pass cooling. Thus, the stand-alone impact of pad backing material on the pads' temperature cannot be easily deduced.

In 2003, Ettles et. al [26] present experimental results and predictions comparing pad temperatures of a copper-PTFE- faced and copper babbitt-faced thrust bearing. As shown in Table 9, the experiment includes two sets of bearings. Bearing #1 has 8 pads with 464 mm mean pitch diameter, 5 mm layer of Polytetrafluoroethylene (PTFE), and 40 mm overall pad thickness. On the other hand, bearing #2 has 912 mm mean pitch diameter, 8 pads, 2 mm PTFE layer and 38 mm overall pad thickness. The maximum operating specific load for the bearing sets is 10.1 MPa. The maximum operating sliding speed for set #1 is 41 m/s while for set # 2 is 28 m/s. Table 9 lists the thermal conductivities of each of the pads' backing and facing materials. PTFE having a low thermal conductivity (0.24 W/m ºC) acts as an insulator and allows less heat transfer through the pad surface compared to a copper babbitted-face (40 W/m ºC) pad. Measurements 21 mm below a pad surface show a significant temperature (25ºC) difference between a Cu-PTFE pad and a copper babbitted pad. Further, the temperature measurements in the oil film show a negligible difference. For bearing set #1 the maximum difference between the two pads is ~ 3ºC. Figure 5, taken from Ref [29], shows predictions of temperature distribution across the Cu-PTFE pads and babbitted pads for operation with load at 5 MPa and 300 rpm (14 m/s). The large temperature gradient across the PTFE layer validates the insulating property of PTFE. The low temperature gradient across the Cu layer (100 W/m ºC) comes from its high thermal conductivity. Since Babbitt

[9] By-pass cooling pad have circumferential heat transfer chamber on the back of the pads. Cool oil directed at the back of the pad helps to reduce the overall pad temperature.

(40 W/m ºC) and steel (51 W/m ºC) have a similar thermal conductivity, the temperature gradient is consistent across the pad thickness.

Table 9 Operating conditions, pad material thermal conductivity and geometric parameters of bearings tested by Ettles et. al [26].

	Bearing set # 1		Bearing set #2	
Mean pitch diameter (mm)	464		912	
Thickness PTFE (mm)	5		2	
Overall pad thickness (mm)	40		38	
No. of thrust pads	8		8	
Specific load, MPa	10.2		10.2	
Sliding speed, m/s	41		24	
	Steel	Babbitt	Copper matrix	Unfilled PTFE
Thermal Conductivity (W/m.	51	40	100	0.24

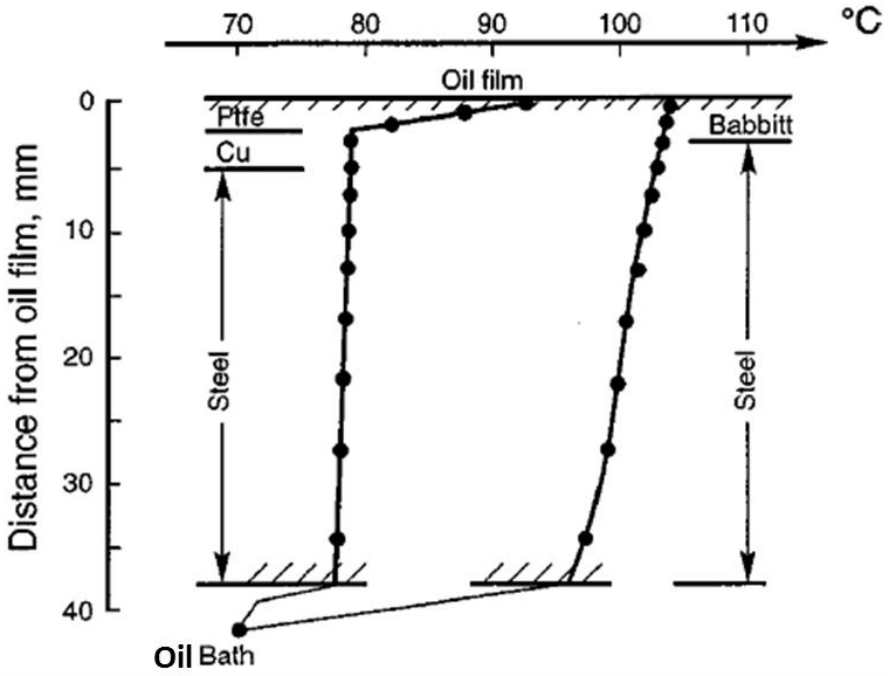

Figure 5 Reprinted from Ref. [29].Predictions for temperature distribution across PTFE and babbitted pads at 5 MPa and 300 rpm (14 m/s)

In 2015, Zhou et al. [34] present an experimental results comparing the static force performance of two eight-pad tilting pad thrust bearings. The bearings differ by pad face material with one being babbitted while the other is coated with polyether ether ketone (PEEK). Both bearings are steel backed having 152 mm pad inner dia., 279 mm pad outer dia., 60 % pivot offset, 62.5 mm pad size and one *L/D* aspect ratio. The operating conditions include shaft speed of 11,000 rpm (124 m/s) and 6,000 rpm (68 m/s) and maximum specific load of 16.2 MPa. The main aim of the work is to study the effect of pad facing material on bearing load capacity, maximum pad temperature, lubricant outlet temperature, and load capacity. As shown in Table 10, PEEK having a high tensile strength (140 MPa), melting point (343°C), and low thermal conductivity (0.87 W/mK) compared to babbitt (77 MPa, 241°C, and 55 W/mK) has the capability to bear more load than babbitt. Moreover, having a low thermal conductivity (0.87 W/mK) compared to babbitt (55 W/mK), PEEK acts as an insulator ensuring a low sub-surface pad temperature. The insulation property of PEEK and its high load capacity is evident from the test results. Test results show signs of bearing distress[10] for babbitt layered bearing at 9.6 MPa load and 11,000 rpm (124 m/s) while PEEK-bearing successfully operate upto 14.5 MPa without any bearing distress. Moreover, for the same operating conditions, the difference between the power loss of the bearings is insignificant. Furthermore, the variation in pad temperatures over the range of applied loads is small, the PEEK bearing pads show a 6 °C variation compared to 41 °C for the Babbitt-bearing pads.

Table 10 Properties of babbitt and PEEK materials for test bearing in Ref. [34].

Properties	Babbitt	PEEK
Density, kg/m^3	7400	1450
Modulus, GPa	52	12
Tensile Strength (20°C) MPa	77	140
Melting Point, °C	241	343
Thermal Conductivity,	55	0.87
Specific Heat, kJ/KgK	0.23	1.8

[10] Bearing distress include marks of babbitt wear or oil coking on the pad surface.

The literature reviews experimental investigations conducted to quantify the effects of bearing geometry [4-22] on the static and dynamic forced response characteristics of TPJBs. Refs. [27-34] discuss several test results assessing the effect of pad facing and backing materials on the performance of TPBs. Most tests have been conducted on tilting pad thrust bearings (TPTBs). The literature review shows that experiments to study the effect of pad material of tilting pad journal bearing (TPJB) performance are scant, in particular when it comes to using copper and steel as a pad backing material. One of the reasons there's more research on the effect of pad material on performance of TPTB compared to TPJB is evident from the literature review. The literature review shows that TPTBs operate at significantly higher surface speeds (max. 146 m/s) and specific loads (max. 16 MPa) compared to TPJBs (max. specific load is 4 MPa and max. surface speed is 105 m/s). Thus, thrust bearings operate at significantly higher pad temperatures compared to journal bearings. This drives the demand for research on pad material for TPBs.

With the increasing demand for high power turbomachinery (high speed and large loads), experimental data presenting solely the effect of pad material on the performance of TPJBs would be highly beneficial. Moreover, no author in the literature review discusses about the effect of pad material on TPJB dynamic force coefficients. The reason might be that a change of backing material, from steel to copper, has little effect on the bearing force coefficients. Thus validation of this assumption is warranted. This further motivates a thorough test research program and comparison of static and dynamic properties of the steel-pads and copper-pads tilting pad journal bearings.

4. TEST RIG DESCRIPTION

The following section summarizes a description of some of the major components of the bearing test rig. The test rig underwent major modifications in 2017 which led to increasing the shaft operational speed from 8000 rpm to 16000 rpm, and the inclusion of an in-line torque meter to directly measure the drag torque in the bearing.

4.1 Mechanical Test Section

As shown in Figure 6, the main section of the test rig sets on a solid steel base. Two 457 mm apart steel pedestals rest on the steel base and support the test shaft. The test shaft made of AISI 4140 steel, shown in Figure 7, has a machined diameter of 101.590 ± 0.003 mm. A bellow coupling connects the test shaft with a torque meter and a 65-kW air drive motor which operates on compressed air (8 bar). The maximum operating speed of the turbine is 17,000 rpm and the maximum torque the torque meter can record is 100 Nm. Two high precision ceramic ball bearings oriented in back-to-back orientation, spaced approximately 450 mm apart, support the test shaft. A separate oil-mist lubrication system lubricates the two angular contact ball bearings.

As shown in Figures 6 and 7, air buffer seals attached at each end of the pedestals separate the test bearing discharge oil from entering the ball bearings chamber and mixing with the oil-mist. The discharge oil is collected in collection chambers, shown in Figure 6, and drains into the oil return line through discharge ports.

To hold the test bearing, the test rig utilizes a split bearing housing, shown in Figure 6, which clamps on to the test bearing. The bearing housing has connections for all the sensors, hydraulic shaker stingers and pitch stabilizers. Six pitch stabilizers, spaced 120º apart on each side of the bearing housing connect the housing with the pedestals. The pitch stabilizers also allow yaw and pitch adjustments of the bearing housing.

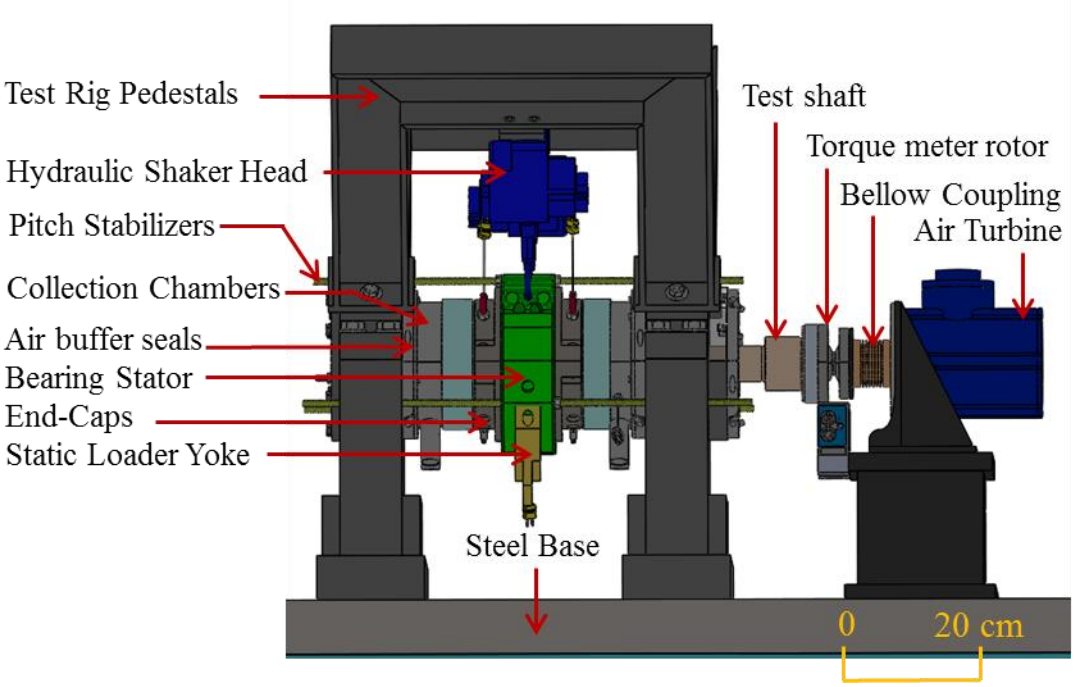

Figure 6 Schematic view of bearing test rig.

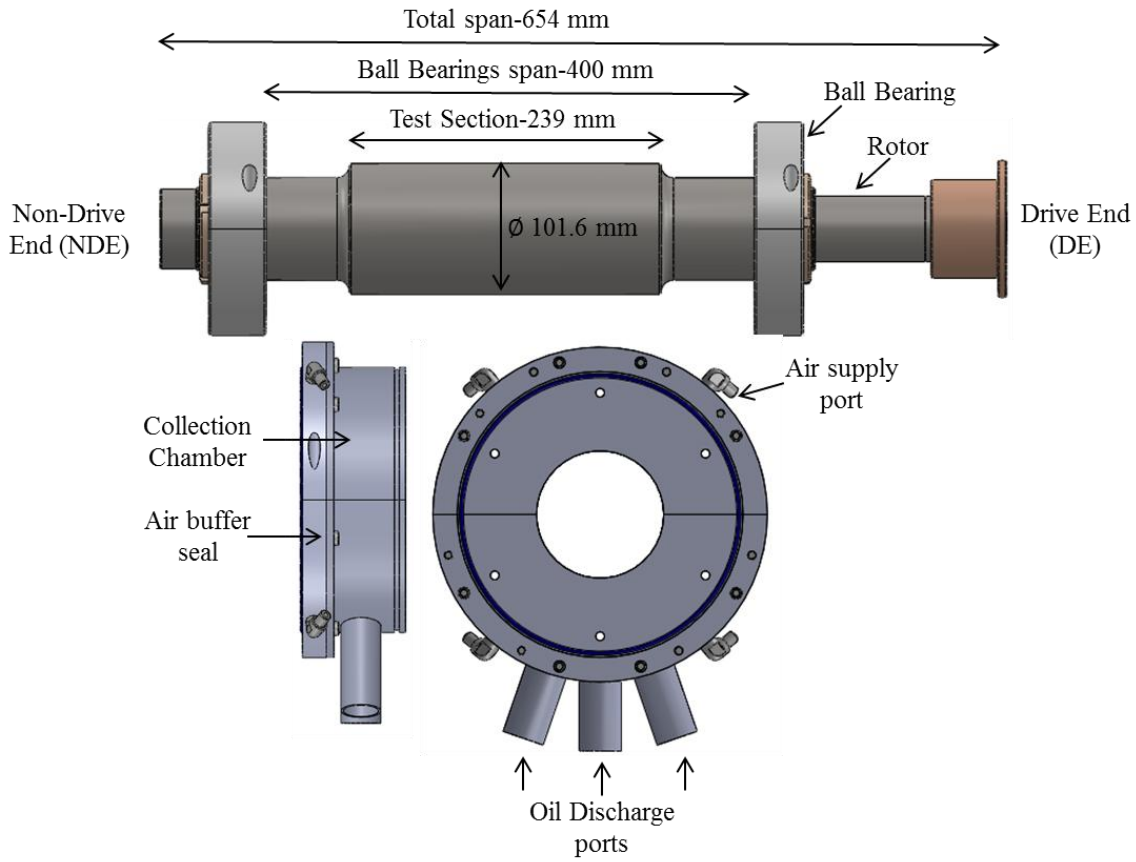

Figure 7 Schematic views of test shaft, ball bearings, air buffer seal, and collection chamber.

4.1.1 Static and Dynamic Loading Systems

As shown in Figure 8, a pneumatic static loader applies a unidirectional static load to the bearing housing. The loading assembly comprises of a pulley and yoke to ensure that the load is applied only along the (-) y-direction. A soft spring (K_{loader} = 0.26 MN/m) attached between the yoke and pneumatic loader avoids transmissibility of the test vibration to the pneumatic loader. A load cell (max. 22,000 N) attached to the pulling cable records the applied static load.

While the pneumatic loader applies the static load, two-orthogonally attached hydraulic shakers (*X*, *Y*) apply dynamic loads to the bearing. Each hydraulic shaker head comprises of a displacement transducer (Linear Variable Differential Transformer) and a

solenoid valve. Two separate hydraulic pump powers each shaker head through 20 MPa of hydraulic oil. The shakers can dynamically excite the system with excitation frequencies ranging up to 1 kHz at low dynamic load (~ 100 N) and can provide a maximum force of 4.45 kN at low frequencies (< 200 Hz). As shown in Figure 8, each shaker head transmits the force through a string of load cell and stingers. The thin steel stingers having a length to diameter ratio of ~ 12 isolate the shaker heads from the test structure vibrations.

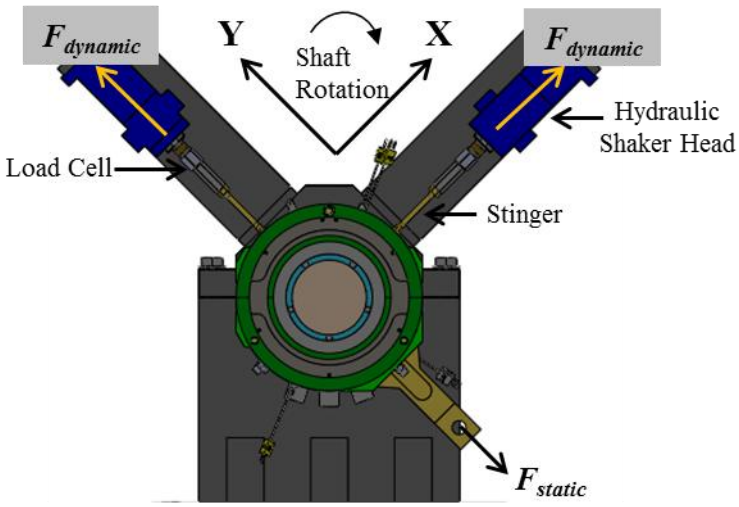

Figure 8 Hydraulic shaker and static loader setup for bearing static and dynamic load excitation.

4.2 Instrumentation[11]

Figure 9 shows the schematic view of the bearing stator housing and end-cap detailing the typical sensors used in the bearing test. The test-rig has four proximity sensors to measure relative displacement along *X* and *Y* directions between the rotor and the test bearing. Figure 9 display four locations of the proximity probe, two sensors mounted orthogonally at two different axial planes, on the outer diameter (OD) of the bearing end caps. This arrangement also helps to monitor the bearing housing's axial pitch.

As shown in Figure 9 two accelerometers, orthogonally mounted (*X, Y*) on the OD of the bearing housing records acceleration of the bearing housing.

[11] Adapted from internal Turbo Lab memo provided to sponsor [35]

The housing mounts three pressure transducers to measure lubricant pressure in the test bearing. One sensor, installed at the top of the bearing housing, measures the inlet lubricant pressure to the bearing while the other two, installed at the bottom of both the end caps, measures the exit pressure.

Three J-Type thermocouples measure temperature (rated up to 220°C) of the lubricant supplied to the test bearing. Figure 9 show thermocouples location on the bearing housing. One thermocouple, installed at the bottom of the bearing hosing, measures inlet lubricant temperature while the other two, installed at the top of both the end caps, measures the exit temperature.

Two load cells, attached with the shaker-stinger assembly, measures dynamic loads (up to 4500 N) whereas another load cell (not shown), attached with the static loader, measures applied static load (up to 22000 N) to the bearing housing. The flowmeter (not shown) measures lubricant flow rate (up to 100 GPM) supplied to the test bearing.

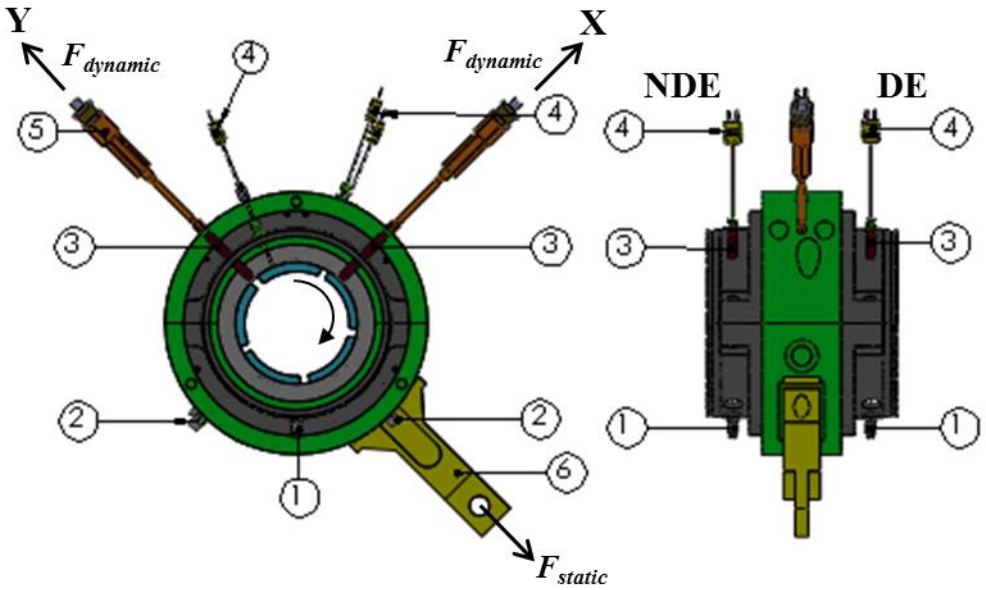

ITEM No.	PART	QTY.
1	Pressure Transducer	3
2	Accelerometers	2
3	Proximity Probes	2
4	Thermocouples	3
5	Shaker Load Cell	2
6	Static Loader	1

Figure 9 Sensor locations on the bearing stator housing. Stator housing side view (top left) and top view (top right).

4.3 Oil flow loop system [12]

Figure 10 & 11 depict schematic diagrams of the oil flow loop system delivering lubricant to the test rig.

4.3.1 Internal (test-cell) oil flow loop

Table 11 details some of the major component of the internal oil flow loop. Figure 10 shows the internal (cell) oil loop for supplying and controlling the oil flow. A positive

[12] Adapted from internal Turbo Lab memo provided to sponsor [36]

displacement gear pump (max 55 GPM) delivers oil from the main tank into the test bearing article. The system includes a pneumatically operated control valve (38 mm) for flow control, a turbine-type flow meter, a three micron filter, and a collection of ball valves. The control valve also sets the oil pressure into the test rig. A turbine type flow meter continuously measures the delivered flow-rate. Further downstream, a three-micron oil filter strains off suspended dirt particles and delivers clean oil to the test bearing. The collection chambers then collect the discharge oil and release it into the supply line.

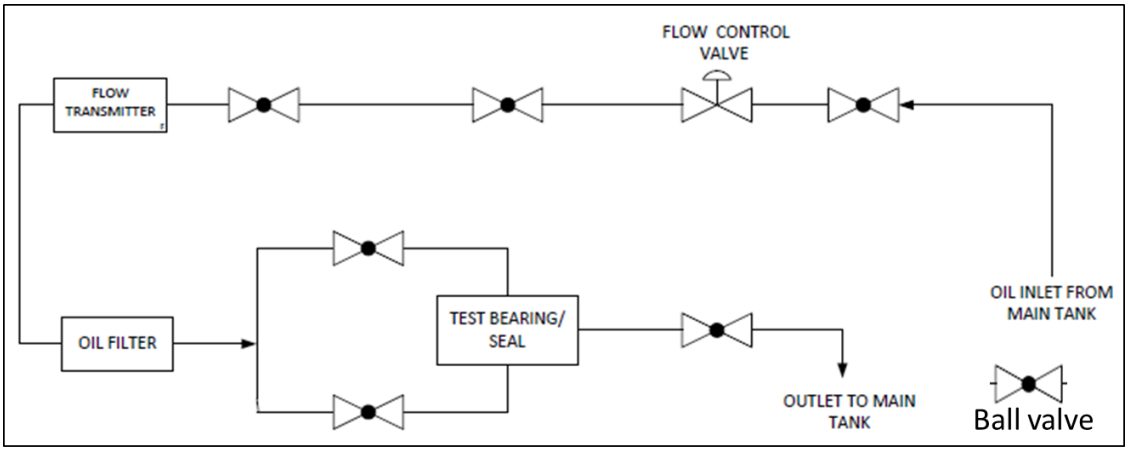

Figure 10 Schematic diagram of oil flow loop for test rig.

Table 11 List of components in the internal oil flow loop.

Component	**Operating Range/Rating**
Low Flow control valve	ANSI Class 300
Flow Transmitter	0-100 GPM
Oil filter	3 µm, 6000 psi

4.3.2 External (Outdoors) Oil Flow Loop

Located outside the test-cell, Figure 11 shows the oil heating and cooling loop system. The installation controls and maintains the oil temperature at a set magnitude. The heating and cooling loops contain a 15.8 kW electric heater, a sump tank (100 gallon), a main oil tank (215 gallon), an air cooler, and flow control valves. Table 12 lists some of the major components of the heating and cooling loop system. The heating loop with a 15.8 kW heater, delivering flow at a rate of 8 GPM, raises the lubricant temperature to the desired temperature quickly as per a test requirement, while the cooling loop helps to prevent the oil temperature from rising further as it maintains the test conditions. For VG 32 oil, whose specific heat is 2,150 J/kg K and density equal to 820 kg/m^3, the heater rises the temperature of 8 gallons oil by 19°C in ~one minute. With this flow rate, the oil temperature in the sump tank (100 gallons) increases by 19°C in about 15 min. The oil temperature in the main tank (215 gallons) increases the same amount in about 30 minutes. Without the heating loop, it would be necessary to operate the test rig continuously, for about a couple of hours, to meet the desired temperature for a test.

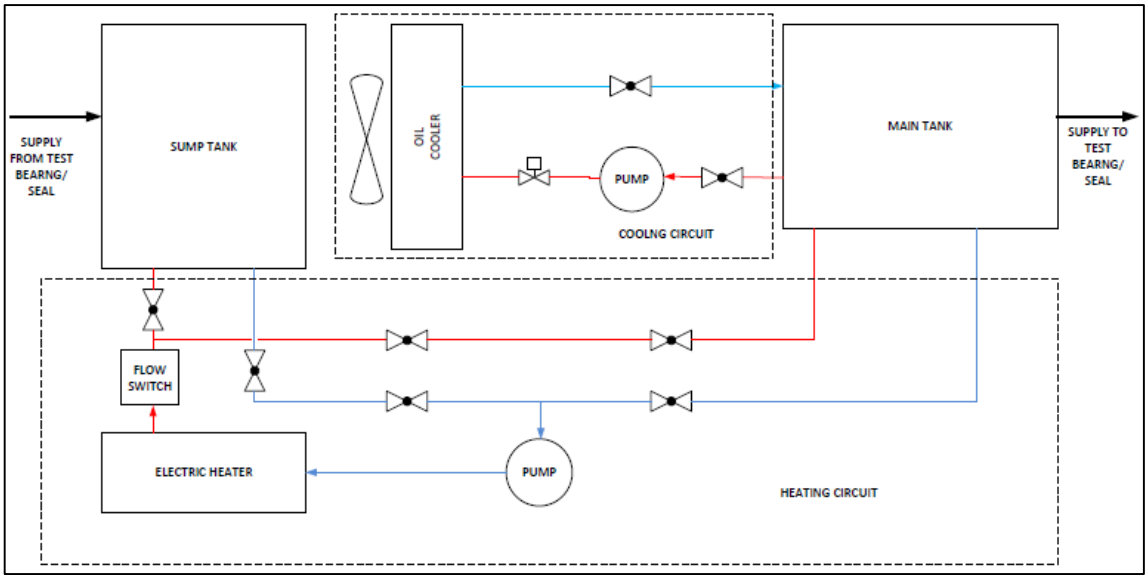

Figure 11 Schematic diagram of oil flow heating and cooling circuit components.

Table 12 List of Components in the external oil flow loop.

S.No	Component	Operating Range/Rating
1	Oil flow control valve	ANSI 600 class
2	Heater	15,800 W
3	Heating Pump	8 GPM
4	Air Cooler	200 psi @ 300 °F

4.4 Bearing Description

Table 1 in Chapter 2 details the bearing geometry for the two test bearings. The bearings differ only in terms of their pad backing material, i.e. one has steel-backed pads, and the other has copper-backed pads. Both bearings have five pads, 0.4 *L/D* ratio, spherical (ball-in-socket) pivots, 12 mm pad thickness, 50 % pivot offset, and ~ an 0.8 mm of babbitt thickness. Both bearings operate under a Load-On-Pad (LOP) configuration and with a flooded[13] lubricant supply condition.

The bearing design radial clearance is 61 μm (2.4 mils) whereas the average assembled radial clearance (at 25°C) for both bearings is C_b = 63.5 μm (2.5 mils). The clearance to shaft diameter ratio (C_b/D) ~0.0013.

Figure 12 shows a schematic view of a half TPJB. In the figure, the bearing housing includes feed holes and two side end seals. As shown in Figure 13, each bearing pad includes four K-type thermocouples along the circumferential direction and two thermocouples along the axial direction at 75% arc length of the pad. Altogether each bearing has thirty K-type thermocouples. A thermocouple tip is ~ 2.5 mm below the pad surface (~ 1.7 mm below babbitt).

[13] The flooded bearing configuration includes a bearing housing with oil feed holes (7.94 mm dia.) between each set of pads and end seals (0.29 mm radial clearance) at the sides. The end seals restrict the exit lubricant flow and aid to pressurize the bearing housing; thus, keeping the bearing flooded with oil.

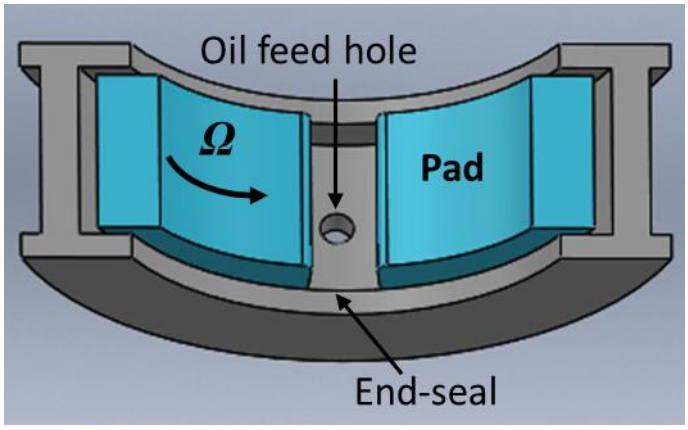

Figure 12 Schematic view of half journal bearing with oil supply hole and end seals.

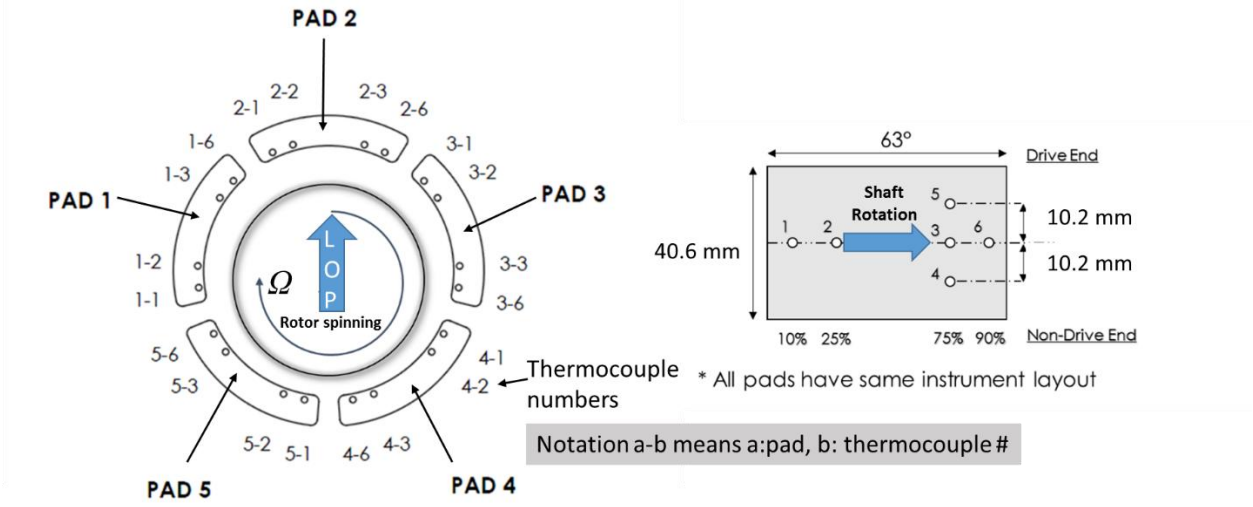

Figure 13 Bearing pads' thermocouple layout in the circumferential and axial directions.

5. EXPERIMENTAL PROCEDURE

5.1 Bearing Clearance

Before supplying oil to a test bearing and turning on the air motor, the first task is to measure the *cold* clearance of the bearing. This '*cold*' clearance refers to a measurement at room temperature (25°C) with no oil in the system and no shaft rotation.

The measurement involves swaying the bearing housing assembly around the stationary (fixed) shaft. As shown in Figure 8, a pair of hydraulic shaker orthogonally attached to the bearing housing push and pull the bearing housing assembly with a load of ~ 400 N. The eddy current sensors, shown in Figure 9, record the relative motion between the shaft and bearing and deliver the clearance boundary of the bearing pads. The resulting shape for a five pad TPJB is a pentagon, as depicted in Figure 14. Recall, both bearings operate under a LOP configuration with pad # 2 being the loaded pad. Each side of the pentagon shows a pad of the TPJB and the mid-point of each side represents the pivot location of a 50% offset pad bearing. The coordinates of each corner (vertex) are acquired from the pentagon. Through geometry and using the vertex coordinates, the mid-point (pivot) of each side is calculated. A best-fit circle including all the five points gives the nominal bearing diametrical clearance (C_d). Table 13 lists the measured individual and nominal pad diametrical clearances of the steel-pads bearing and copper-pads bearing at 25 ºC. The nominal diametrical clearance of the copper-pads bearing is 127 µm ($2C_b$) whereas for the steel-pads bearing it is 130 µm.

As the heat generated through shear drag from the rotor heats up the bearing, the operating clearance changes due to thermal expansion of both the rotor and the bearing. Thus, an estimate of the operating '*hot*' clearance (HC) is also determined. A '*hot* clearance' refers to the measurement taken at an elevated rotor-bearing temperature immediately after shutting off the drive motor. Decelerating the rotor speed, shutting off the test rig and measuring the hot clearance takes a total of approximately 10 minutes. The process to measure the clearance takes ~ 2 min. Figure 14 shows the HC of the steel-pads bearing and the copper-pads bearing recorded immediately after operating the test rig at 14 krpm (74 m/s). The HC of both bearings indicates unequal thermal expansion of the shaft-bearing

system. The average HC of the copper-pads bearing reduces by ~18 % to 104 µm whereas the average HC of the steel-pads bearing reduces by ~ 9 % to 118 µm. The clearance of the copper-pads bearing's pad two (loaded pad) reduces from 124 µm to 96 µm (28 um difference). Thus, indicating a higher thermal growth of pad # 2 due to the heat generated from oil shear drag.

A comparison of the HC for pad # two (loaded one) in both bearings shows that the C-PB has a HC = 96 µm while S-PB has a HC = 113 µm. As compared to the S-PB, the C-PB has a larger pad temperature (71 °C vs. 66 °C) and a larger thermal expansion coefficient (17.6 x 10^{-6} 1/°C vs. 12.2 x 10^{-6} 1/ °C). The larger pad temperature and expansion coefficient produce a larger thermal growth of the C-PB, and thus result in the smaller HC for the C-PB. Similar to pad # 2, the other four pads of C-PB have a HC smaller than those of the S-PB. Table 13 further lists the individual *hot* pad clearances. The steel-pads deviates a maximum of 6 µm from the mean magnitude (118 µm), whereas the copper-pads deviate by 8 µm from a mean of 104 µm. For the S-PB, the standard deviation of the *hot* pad clearances from the mean value is 3.8 µm. However, for the C-PB, the *hot* pad clearances standard deviation is 6.9 µm.

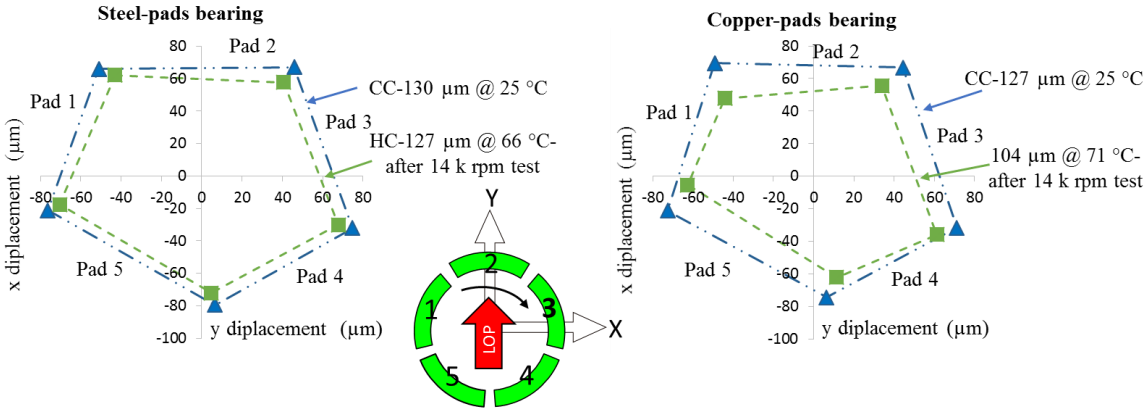

Figure 14 Bearing clearance for (left) steel-pads bearing and (right) copper-pads bearing. Measurement conducted at 25°C and at an elevated temperature (66°C and 71°C) after a test at 14 krpm shaft speed.

Table 13 Measured diametrical pad clearance of a copper-pads bearing and a steel-pads bearing at 25 °C, 71°C, and 66°C, respectively. Deviation of the hot and cold clearance of the copper-pads bearing and the steel-pads bearing.

Pad number	'*Hot*' diametrical clearance @ 71℃ (μm)- Copper-pads	'*Cold*' diametrical clearance @ 25℃ (μm)- Copper-pads	'*Hot*' diametrical clearance @ 66℃ (μm)- Steel-pads	'*Cold*' diametrical clearance @ 25℃ (μm)- Steel-pads
1	110	135	124	136
2	96	124	113	127
3	114	127	120	132
4	102	127	118	131
5	98	122	115	127
Average (nominal)	104 **μm**	127 **μm**	118 **μm**	130 **μm**
Standard deviation	**6.9 μm**	**4.4 μm**	**3.8 μm**	**3.4 μm**

5.2 Structure Baseline Test Data and Parameter Identification Model

5.2.1 Fluid Film Model

For small rotor perturbations about an equilibrium position, as shown in Figure 15, the fluid-film bearing reaction load is modelled as a linearized system with spring, mass and damping force coefficients.

$$-\begin{bmatrix} f_{bx} \\ f_{by} \end{bmatrix} = \begin{bmatrix} K_{xx} & K_{xy} \\ K_{yx} & K_{yy} \end{bmatrix} \begin{bmatrix} \Delta x \\ \Delta y \end{bmatrix} + \begin{bmatrix} C_{xx} & C_{xy} \\ C_{yx} & C_{yy} \end{bmatrix} \begin{bmatrix} \Delta \dot{x} \\ \Delta \dot{y} \end{bmatrix} + \begin{bmatrix} M_{xx} & M_{xy} \\ M_{yx} & M_{yy} \end{bmatrix} \begin{bmatrix} \Delta \ddot{x} \\ \Delta \ddot{y} \end{bmatrix} \quad (1)$$

where f_{bx} and f_{by} are the bearing reaction forces along the x and y directions. The x denotes the unloaded direction and y denotes the loaded direction. Δx and Δy indicate the relative displacements between the rotor and the bearing pad. Similarly,$\Delta \dot{x}$, $\Delta \dot{y}$ show relative velocities and $\Delta \ddot{x}$, $\Delta \ddot{y}$ show relative accelerations. The terms K_{ij}, C_{ij} and M_{ij}, $i=j$, represent

the direct stiffness, damping and virtual mass coefficients along the orthogonal x and y directions whereas for $i \neq j$ the terms represent the cross-coupled stiffness, damping and virtual mass coefficients along the orthogonal x and y directions.

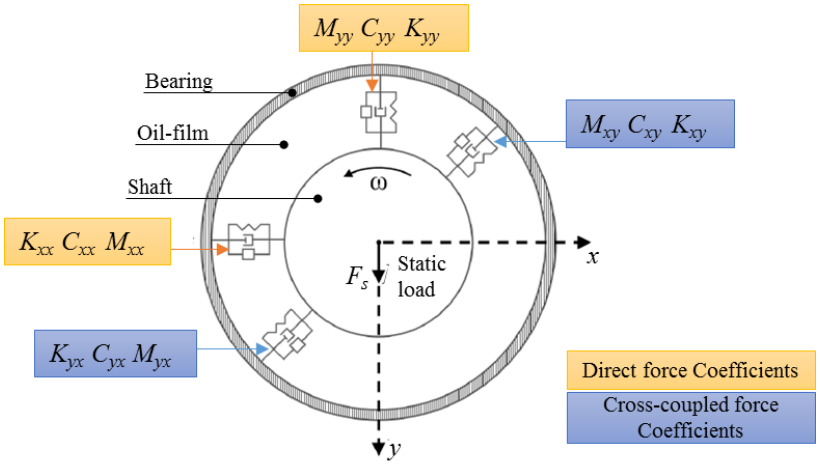

Figure 15 Fluid film bearing modelled as an equivalent linear system with spring, mass and damping force coefficients.

5.2.2 Parameter identification

Childs and Hale [37] present a mathematical model to analyze and extract the force coefficients of a fluid film bearing from test dynamic data. As shown in Figure 15, Childs & Hale method assumes the bearing as a two-degree of freedom system with motion along the x and y directions. The EOM of the bearing housing is

$$\begin{bmatrix} f_{bx} \\ f_{by} \end{bmatrix} + \begin{bmatrix} f_{ex} \\ f_{ey} \end{bmatrix} + \begin{bmatrix} f_{sx} \\ f_{sy} \end{bmatrix} = M_s \begin{bmatrix} a_{sx} \\ a_{sy} \end{bmatrix} \quad (2)$$

Here M_s (~25 kg) is the mass of the housing+bearing, (f_{bx}, f_{by}) are fluid film reaction forces, (f_{ex}, f_{ey}) are external dynamic forces applied by the hydraulic shakers, (f_{sx}, f_{sy}) are the reaction forces from the structure (baseline), and (a_{sx}, a_{sy}) are the measured housing absolute accelerations along the x and y directions, respectively.

The baseline or structure reaction forces (f_{sx}, f_{sy}) are modeled as

$$\begin{bmatrix} f_{sx} \\ f_{sy} \end{bmatrix} = \begin{bmatrix} K_{sxx} & 0 \\ 0 & K_{syy} \end{bmatrix} \begin{bmatrix} \Delta x \\ \Delta y \end{bmatrix} + \begin{bmatrix} C_{sxx} & 0 \\ 0 & C_{syy} \end{bmatrix} \begin{bmatrix} \Delta \dot{x} \\ \Delta \dot{y} \end{bmatrix} \tag{3}$$

Combining equations (1), (2), and (3) gives the final EOM for the bearing housing

$$\begin{aligned} &\begin{bmatrix} f_{ex} - M_s\, a_{sx} \\ f_{ey} - M_s\, a_{sy} \end{bmatrix} \\ &\quad = \begin{bmatrix} K_{xx} + K_{sxx} & K_{xy} \\ K_{yx} & K_{yy} + K_{syy} \end{bmatrix} \begin{bmatrix} \Delta x \\ \Delta y \end{bmatrix} \\ &\quad + \begin{bmatrix} C_{xx} + C_{sxx} & C_{xy} \\ C_{yx} & C_{yy} + C_{syy} \end{bmatrix} \begin{bmatrix} \Delta \dot{x} \\ \Delta \dot{y} \end{bmatrix} + \begin{bmatrix} M_{xx} & M_{xy} \\ M_{yx} & M_{yy} \end{bmatrix} \begin{bmatrix} \Delta \ddot{x} \\ \Delta \ddot{y} \end{bmatrix} \\ &\quad + \begin{bmatrix} f_{sx} \\ f_{sy} \end{bmatrix} \end{aligned} \tag{4}$$

A Discrete Fourier Transform (DFT) converts the measured time domain data of relative displacements, excitation forces and accelerations into the frequency domain yielding the algebraic equations

$$\begin{bmatrix} F_{ex} - M_s\, A_{sx} \\ F_{ey} - M_s\, A_{sy} \end{bmatrix} = \begin{bmatrix} H_{xx} & H_{xy} \\ H_{yx} & H_{yy} \end{bmatrix} \begin{bmatrix} D_x \\ D_y \end{bmatrix} \tag{5}$$

where (F_{ex}, F_{ey}) are the DFT of the excitation forces, (A_{sx}, A_{sy}) are the DFT of the bearing housing accelerations, and (D_x, D_y) are the DFT of the rotor-bearing relative displacements along the x and y directions. H_{ij} is the complex dynamic stiffness function

$$H_{ij} = \left(K_{ij} - \omega^2 M_{ij}\right) + j\left(\Omega C_{ij}\right) \quad i, j = x, y \tag{6}$$

The function incorporates the direct stiffness (K), damping (C) and virtual mass (M) coefficients and the cross-coupled stiffness, damping and virtual mass coefficients, respectively. The real part of the complex dynamic stiffness [Re (H_{ij})] = $\left(K_{ij} - \omega^2 M_{ij}\right)$ where ω is the excitation frequency. The force coefficients K_{ij} and M_{ij} are extracted from the intercept and quadrature of the curve fit of a linear function of ω^2 on Re (H_{ij}). The imaginary part [Im (H_{ij})] of the complex dynamic stiffness is$\left(\omega\, C_{ij}\right)$. The slope of the linear

curve fit to Im (H_{ij}) delivers the C_{ij} damping coefficients. Curve-fitting the Re (H_{ij}) and Im (H_{ij}) using the K-C-M model dictates frequency independency of the force coefficients.

Equation (5) gives only two complex equations and comprises of four H_{ij} complex stiffnesses. Exciting the bearing housing independently along the orthogonal *x* and *y* directions at a particular frequency yields four independent equations. A pseudo-random excitation to the bearing houses produces a complete set of H_{ij}.The excitation waveform sweeps from 10 Hz to 320 Hz with increments of 10 Hz. To determine the variability of the acquired data the excitation is performed 10 times along each *x* and *y* direction, respectively. Results with a high variability are neglected from the analysis. The four independent complex equations acquired through two independent excitations are:

$$\begin{bmatrix} F_{exx} - M_s\, A_{sxx} & F_{exy} - M_s\, A_{sxy} \\ F_{eyx} - M_s\, A_{syx} & F_{eyy} - M_s\, A_{syy} \end{bmatrix} = \begin{bmatrix} H_{xx} & H_{xy} \\ H_{yx} & H_{yy} \end{bmatrix} \begin{bmatrix} D_{xx} & D_{xy} \\ D_{yx} & D_{yy} \end{bmatrix} \tag{7}$$

where F_{eij}, D_{ij} and A_{sij} are the DFT of the excitation forces, rotor-bearing relative displacement and bearing housing acceleration. The subscripts ij correspond to the response in the *i* direction due to excitation along the *j* direction.

The complex dynamic stiffness function (H_{ij}) acquired during a test includes the force coefficients of both the fluid-film bearing and the test rig structure (pitch stabilizers, flexible pipes, static loader). A dry shake or dynamic excitation of the bearing housing i.e. with no oil and shaft rotation gives the baseline data. The baseline yields the force coefficients (K_{sij} and C_{sij}) of the test-rig structure. The net (without structure force coefficients) dynamic complex stiffness of the fluid-film bearing is

$$H_{ij-fluid\ film} = H_{ij} - H_{ij-baseline} \tag{8}$$

where $H_{ij}(i, j = x, y)$ denotes the complex dynamic stiffness functions acquired from a test with oil running through the test rig and $H_{ijbaseline}$ is the complex dynamic stiffness function acquired from a dry shake of the bearing housing.

Figure 16 (a) and (b) show the real and imaginary part of the complex dynamic stiffness acquired through a dry-shake of the bearing housing. Table 14 further shows the equivalent structure stiffness and damping coefficients and mass of the bearing housing (M_s). The bearing housing mass is acquired through an iterative input of mass magnitude in Equation (7) such that the slope of the Re($H_{ij-baseline}$) $\rightarrow (K_{sij} - \omega^2 M_{sij})$ equals zero. As shown in the table, the acquired housing mass ($M_{sx\ and}\ M_{sy}$) is larger than the actual mass (M_s). This difference is because the identified bearing mass $M_{sx,y}$ includes not just the housing mass but also the mass of the sensors, pitch stabilizers, stingers, and hydraulic hoses. These accessories are attached after assembling the bearing housing.

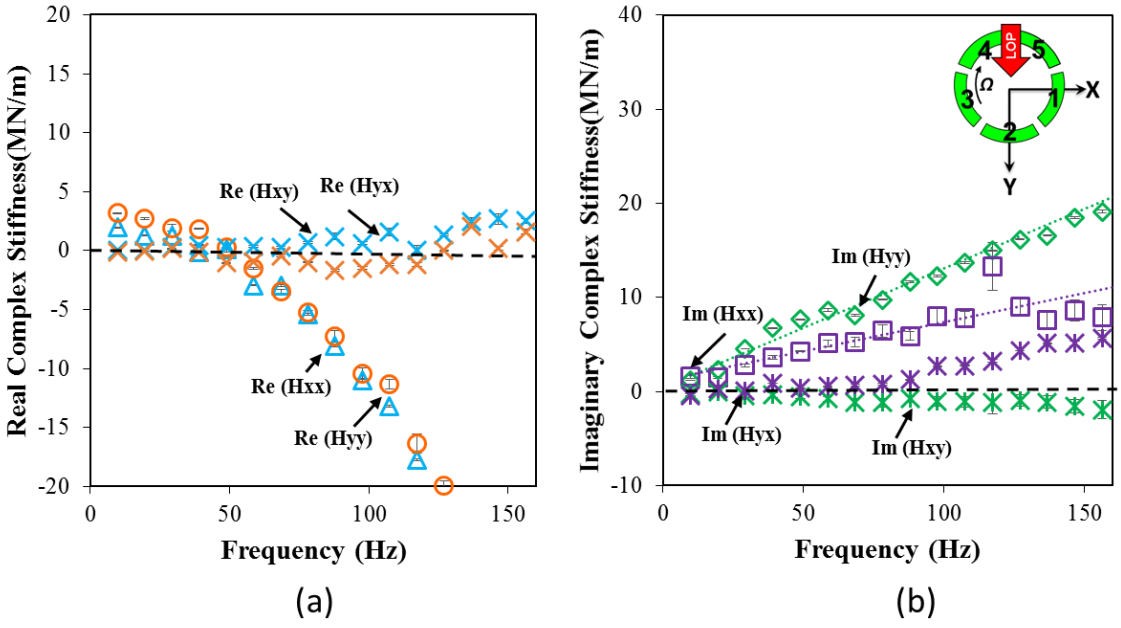

Figure 16 Experimentally derived (a) real and (b) imaginary parts of the complex dynamic stiffness of the test structure vs. excitation frequency. Dry system (no oil).

Table 14 Experimental structural force coefficients from dry shake.

K_{sxx}	1.3 ± 0.3 MN/m
K_{syy}	3.3 ± 1.2 MN/m
C_{sxx}	11= ± 5 KNs/m
C_{syy}	11 ± 4 KNs/m
M_{sx}	34 ± 4 kg
M_{sy}	34 ± 3 kg
Actual Stator Mass, M_s	25 kg

5.3 Input Data for Predictive Model

The tilting pad bearing performance program XLTPJ® [14] predicts the static and dynamic forced performance of a test bearing. The code implements both a thermohydrodynamic (THD) and a thermoelastohydrodynamic (TEHD) model to predict the static and dynamic force performance of a TPJB. The physical model accounts for both pad and pivot flexibilities. The program accepts a user defined load-deflection curve to account for pivot flexibility and for pad elasticity it acquires an ANSYS Finite-Element-Model specifying the pad material, pad thickness, pivot offset, and pad arc length. The model also accounts for fluid inertia effects, pressure and thermal induced deformations, and an advanced thermal fluid flow mixing model at the pad leading edge[14].

Table 15 details the bearing geometry and lubricant properties used in the predictive code. Table 16 further details the analysis options utilized for obtaining the predictions.

As shown later, the experimental results for the static and dynamic load conditions correlate best with predictions from a THD model rather than a TEHD model. The THD model accounts for pivot flexibility and does not include pad flexibility.

For example, consider the complex dynamic coefficients in Figure 42 for the S-PB, the real and imaginary part both correlate well with the experimental data.

The C_{gr} (groove mixing efficiency coefficient) ranges from 0.7 to 0.9 for better estimation of pad temperatures. A low C_{gr} value represents a low hot oil discharge efficiency, i.e. a high hot oil flow carry over from the upstream pad into the downstream pad.

[14] Abdollahi [12] improved the XLTPJB model incorporating an empirical parameter C_{gr} (0.7 to 0.9 used in the analysis) accounting for oil mixing in the oil supply groove.

Table 15 Bearing geometric and lubricant properties used in the predictive code XLTPJB®.

Bearing Geometry	
Rotor Diameter	101.6 mm
Bearing Length	40.6 mm
Pad preload	0.42 ± .04
Pad arc length	63º
Pad thickness	12.4 mm
Pad radial clearance	112 µm
Bearing radial clearance	63.5 µm
Individual pad mass	0.3 kg
Pad moment of inertia about pivot (50%) offset	1.14 kg.cm^2
Babbitt thickness	0.64 mm
Lubricant properties	
Lubricant type	ISO VG-32
Supply pressure	(7-50) kPa
Cavitation pressure	0 kPa
Oil supply temperature	49 ºC
Oil viscosity @ (49 ºC)	19.7 cP
Oil density	850 kg/m^3
Specific heat	1990 J/Kg ºC
Thermal conductivity	0.13 W/m ºC
Viscosity temperature coefficient	0.0405 1/ ºC

Table 16 Analysis options selected in the bearing prediction code XLTPJB®.

Analysis option			
Analysis Model		THD (thermohydrodynamic)	
Fluid Inertia Option (Yes Or No)		Yes	
Inputs for pivot flexibility			
Steel modulus of Elasticity and Poisson		207 GPa, ν = 0.29	
Copper modulus of Elasticity and Poisson		117 GPa, ν = 0.30	
Calculated pivot stiffness [43]		Steel-Pads Bearing (MN/m)	Copper-Pads Bearing
Load MPa	0.48	331	270
	1.0	419	339
	1.45	479	387
Inputs for thermal analysis			
Analysis Type		Haussen heat convection model	
Thermal conductivity κ_T	Steel pad	42.6 W/(m ºC)	
	Copper pad	323.6 W/(m ºC)	
Sump temperature range	Steel-pads bearing	58 – 72 ºC	
	Copper-pads bearing	58 – 62 ºC	
Oil supply flow rate		7.34 – 17.78 LPM (speed dependent-sponsor specified)	
Groove mixing efficiency (C_{gr})		0.7-0.9	

(*) some data not included as it is proprietary to sponsor.

6. BEARINGS' STATIC LOAD CHARACTERISTICS

During a typical test, the operator slowly accelerates the rotor to the required shaft speed (see the test matrix shown in Table 2) while maintaining the oil inlet temperature at T_{in} = 49±0.5 ºC and a supply flow rate as per the test requirement[15]. Two hydraulic shakers center the bearing with respect to the shaft. As soon as the system achieves the desired shaft speed, the hydraulic loader applies a static load on the bearing (LOP). Upon achieving thermal (steady state) equilibrium, the Data Acquisition System (DAQ) records data from all the sensors.

As shown in Figure 17, initially after a start-up, the test system achieves thermal equilibrium in about 45-60 minutes. After achieving thermal equilibrium (steady state) at a set shaft speed, the elapsed time reduces to ~ 15-20 minutes for subsequent load increments. As shown in the figure, the operators continuously monitor the pads' temperature waveforms for unsteady fluctuations and wait for the temperatures to stabilize towards achieving a thermal steady state. As the fluctuations reach a minute level, the operator triggers the DAQ system to acquire a steady state measurement point. In the figure, the vertical lines indicate the time instance at which the DAQ records a steady-state measurement.

[15] At each operating speed the oil supply flow rate is specified by the test bearing sponsor.

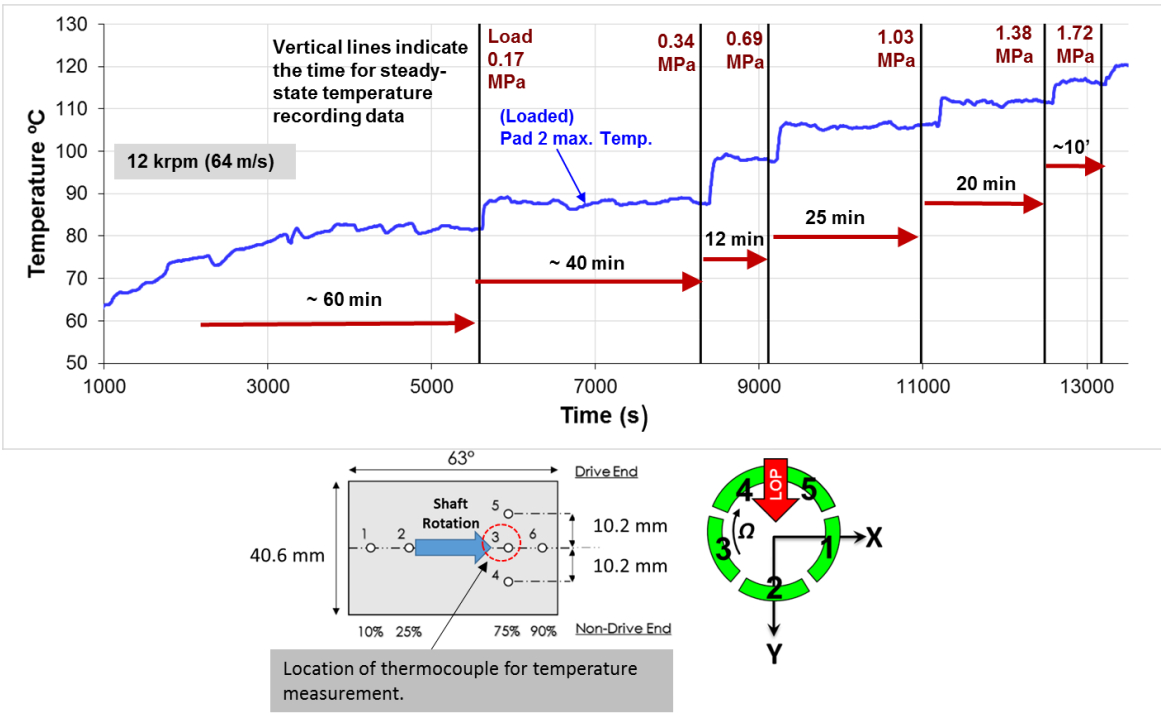

Figure 17 Steel-pads bearing's pad # 2 temperature (°C) vs. time (s) for operation at 64 m/s shaft surface speed and multiple specific loads (0.35 MPa to 1.72 MPa). Inset shows location of thermocouple.

6.1 Shaft Eccentricity

At each operating point the shaft attains an equilibrium position or journal eccentricity (e). As shown in Figure 18, the shaft eccentricity (e) is the relative distance between the shaft center (x_s,y_s) and the bearing center (x_b, y_b). That is

$$e = \sqrt{(x_b - x_s)^2 + (y_b - y_s)^2} = \sqrt{(e_x)^2 + (e_y)^2} \tag{9}$$

where $e_x = (x_b - x_s), e_y = (y_b - y_s)$

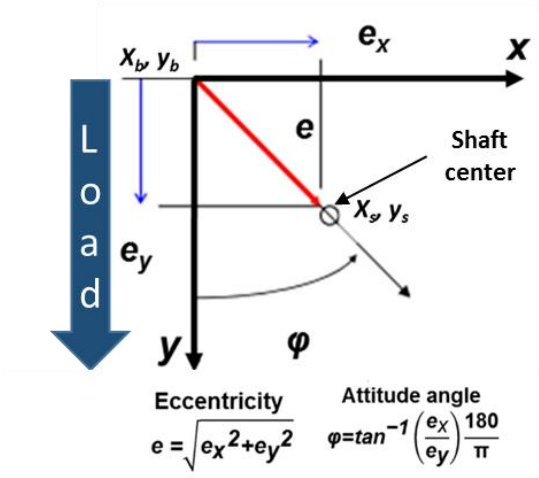

Figure 18 Schematic representation of shaft eccentricity and attitude angle.

Figure 19 shows the shaft eccentricity (*e*) of the steel-pads bearing and the copper-pads bearing as a function of applied specific load *W/(LD)* and an operating speed varying from 6 krpm (32m/s) to 14 krpm (75 m/s). The figure shows that *e* is a strong function of both shaft speed and specific load. The slope of the eccentricity vs. specific load curve gives the static flexibility of the fluid film and the pad-pivot structure.

The shaft eccentricity changes non-linearly with an increase in specific load at a constant speed; thus, indicating an increase in local stiffness. Consider the steel-pads bearing shaft eccentricity; keeping the 6 krpm shaft speed constant, the shaft eccentricity changes from 7 µm to 59 µm (~ 8 times) with an increase in specific load from 0.17 MPa to 2.1 MPa. Moreover, the shaft eccentricity decreases with an increase in shaft speed while keeping the load constant. For example, at 1.38 MPa specific load the shaft shows a decrease in eccentricity from 44 µm to 28 µm (37 % relative decrease) as the shaft speed increases from 6 krpm (32m/s) to 14 krpm (74 m/s). This result indicates that the stiffness of the fluid film increases with shaft speed.

An overall comparison of eccentricity (*e*) results for the steel-pads bearing and the copper-pads bearing shows that at any operating point, the steel-pads bearing (S-PB) reaches a higher shaft eccentricity than that of the shaft in copper-pads bearing (C-PB). For example, at 2.1 MPa and 6 krpm (35 m/s) the S-PB shaft eccentricity is 59 µm compared to a 37 µm for the C-PB shaft (37 % lesser than that in the S-PB). The higher eccentricity of the S-PB

might be due to a lower equivalent bearing stiffness or due to having a larger hot clearance as compared to the C-PB[16]. This outcome will be verified through the comparison of the dynamic force coefficients of both bearings (see Figure 48). Furthermore, a higher eccentricity for the S-PB means likely a lower film thickness and higher pad temperatures.

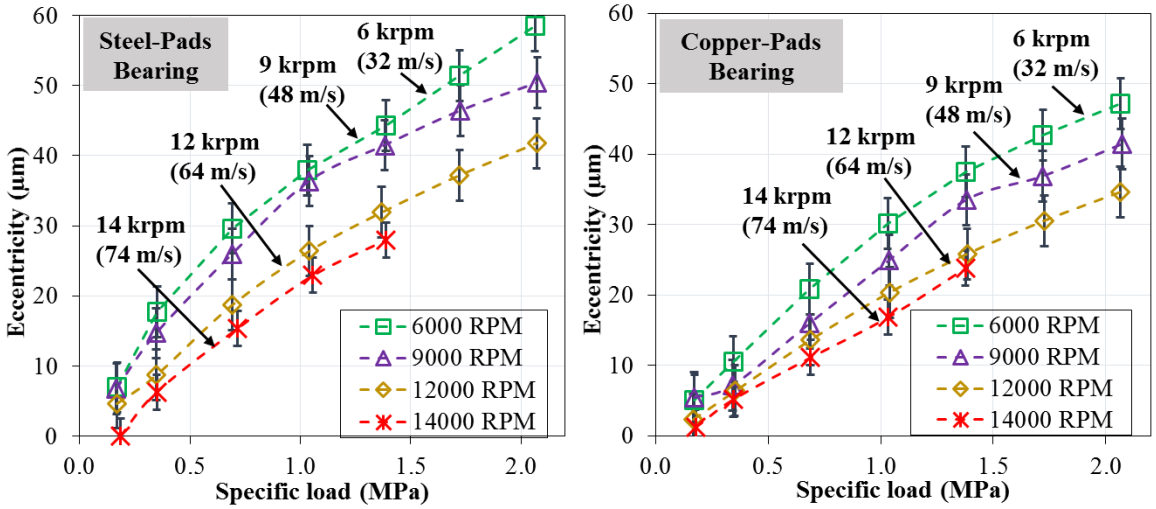

Figure 19 Measured shaft eccentricity (*e*) for (left) steel-pads bearing and (right) copper-pads bearing vs. specific load (0.17to 2.1 MPa) for operation at various shaft speeds (6 to 14 krpm). [Radial clearance C_b = 63.5µm].

The static stiffness of the bearing equals

$$K_{STAT} \cong \frac{\Delta W}{\Delta e} \tag{10}$$

where ΔW is a small change in applied static load and Δe is a change in shaft eccentricity.

Figure 20 shows the derived static stiffness (K_{STAT}) for the steel-pads bearing (S-PB) and the copper-pads bearing (C-PB) as a function of specific load $W/(LD)$ and operating shaft speed varying from 6 krpm (32m/s) to 14 krpm (75 m/s). Note, for both bearings, K_{STAT} shows a strong dependency on the specific load. For example at 6 krpm, the S-PB's static stiffness increases from 110 MPa to 181 MPa (65 % relative increase) with an increase in

[16] The measured hot diametrical clearance of the copper-pads bearing (104 µm) < steel-pads bearing (118 µm). The clearances are recorded immediately after operating the test rig at 14 krpm (74 m/s).

load from 0.6 MPa to 1.8 MPa. Similarly, at 12 krpm shaft speed, the C-PB stiffness increases from 250 MN/m to 333 MN/m (33 % relative increase) with an increase in load from 1.0 MPa to 2.0 MPa. However, at 14 krpm shaft speed, the C-PB static stiffness is constant over the range of load. As shown in Figure 19, the C-PB eccentricity vs. specific load at 14 krpm is linear hence yielding a constant static stiffness.

For shaft speeds > 6 krpm and specific loads > 1.0 MPa, the S-PB K_{STAT} does not change with speed. Figure 19 validates this stiffness independency on speed as the slope of the graphs are the same for shaft speed > 6 krpm and specific load > 1.0 MPa. In contrast to the S-PB, the C-PB static stiffness increases with both shaft speed and specific load.

Figure 20 shows that at 6 krpm and 12 krpm, the C-PB stiffness is 6-18 % higher than the S-PB stiffness. However at 9 krpm, the S-PB stiffness is just 4-10 % higher than the C-PB stiffness.

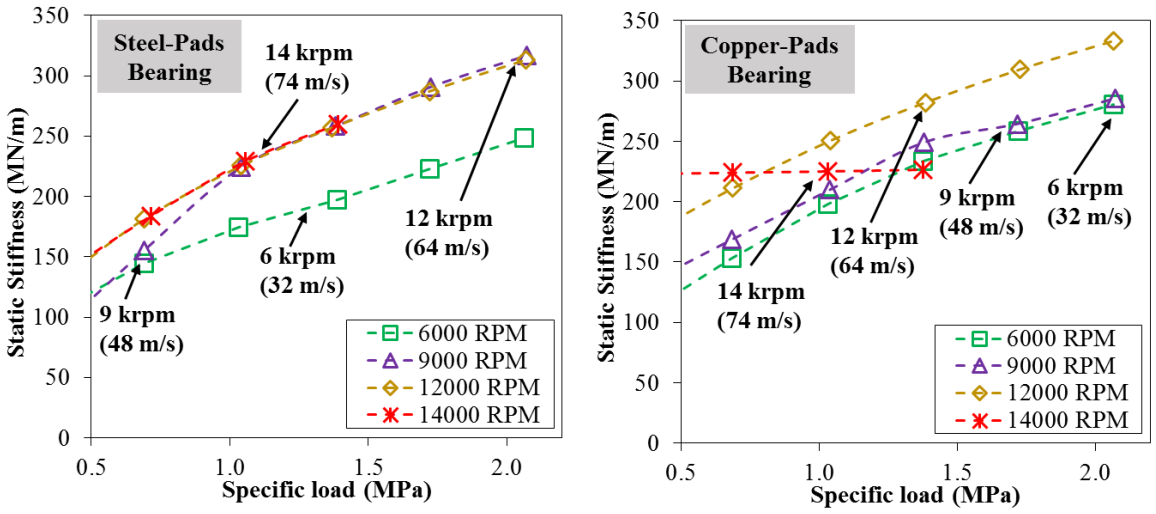

Figure 20 Derived (from static load) static stiffness (K_{STAT}) for (left) steel-pads bearing and (right) copper-pads bearing vs. specific load (0.17to 2.2 MPa) for operation at various shaft speeds (6 to 14 krpm).

Figure 21 shows the dimensionless eccentricity (e/C_b) of the copper-pads bearing (C-PB) and the steel-pads bearing (S-PB) as a function of the Sommerfeld number (S) defined as:

$$S = \frac{\mu_{eff}\, N\, L\, D}{W} \left(\frac{R}{C_b}\right)^2 \tag{11}$$

where μ_{eff} is the effective lubricant viscosity[17], N is the shaft speed in rev/s, $W/(LD)$ is the specific load, R is the shaft radius, and C_b = 63.5 µm is the bearing nominal radial clearance at 25ºC for both bearings.

A low Sommerfeld number represents a low shaft speed and/or a high specific load whereas a high Sommerfeld number represents a high shaft speed and/or a low specific load. The typical trend shown in Figure 21 shows that with an increase in S, the shaft eccentricity (e/C_b) decreases. For the S-PB, the e/C_b is large (>0.5) for low S (<1.0). S <1.0 includes test points with low shaft speed (< 9 krpm) and high specific load (> 1 MPa).

Note the C-PB operates with a lower eccentricity ratio as compared to the S-PB. For example, at the lowest value of S = 0.4, the C-PB operates at 0.75 eccentricity ratio while the S-PB operates at 0.95 eccentricity ratio. This result means that the steel-pads bearing has a smaller film thickness compared to that in the copper-pads bearing. A smaller film thickness results in higher drag sheer and higher pad temperatures.

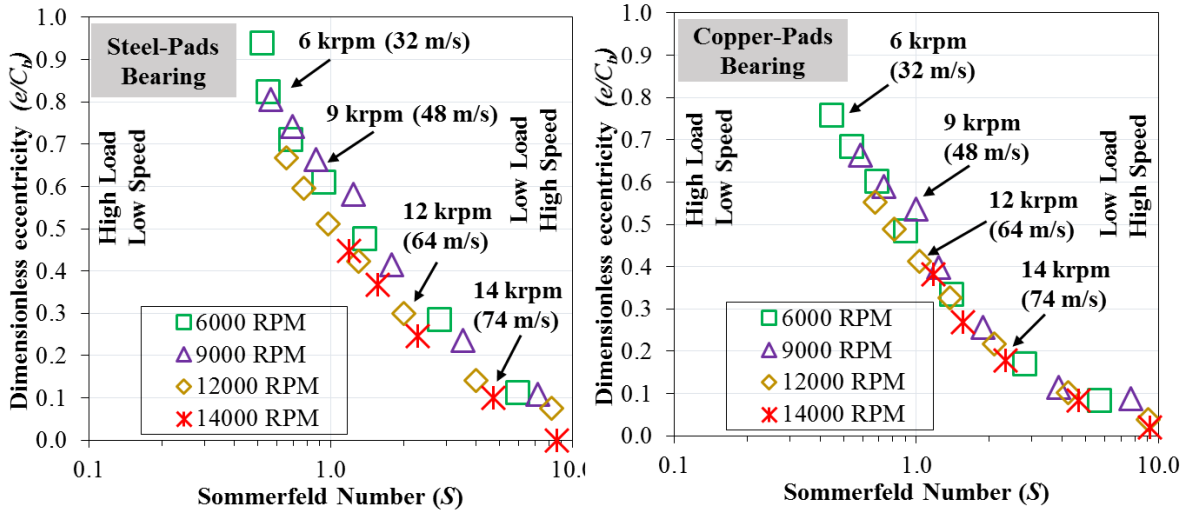

Figure 21 Measured shaft eccentricity (e/C_b) for (left) steel-pads bearing and (right) copper-pads bearing vs. Sommerfeld Number (S) for operation at various specific loads (0.17 to 2.1 MPa) and shaft speeds (6 to 14 krpm).

[17] $\mu = \mu_{ref}\, e^{-\alpha_{vis}(T_{eff} - T_{ref})}$, $T_{eff} = T_{in} + 0.75(T_{discharge} - T_{in})$

Figure 22 presents both the measured and predicted shaft eccentricity (e) for the steel-pads bearing (S-PB) and the copper-pads bearing (C-PB). The graphs showcase e as a function of shaft speed varying from 6 krpm (32 m/s) to 14 krpm (74 m/s) and as a function of specific load ranging from 0.17 to 2.1 MPa. The S-PB eccentricty follows the same trend for both the predicted and measured results, i.e with an increase in speed, at a constant load, the shaft eccentricity decreases. However, with an increase in load at a constant shaft speed, the shaft eccentricity increases.

A comparison of the measured and predicted S-PB eccentricity (e/C_b) results show that for operation at 6 krpm and 9 krpm the computational code slightly under predicts the test results. The percentage difference between the results varies from 4 % to 16%. At shaft speeds of 64 m/s (12 krpm) and 74 m/s (14 krpm), over the range of applied specific loads, the predictions overestimate the shaft eccentricity. The percentage difference ranges from 3% to 25%. Also, for a high load operation (>1.03 MPa) and shaft speed ranging from 32 m/s to 74 m/s, the percentage difference between the predicted and measured results is < 10 %.

A comparison of the C-PB predicted and measured shaft eccentricity (e/C_b) yields similar trends as the S-PB. The predicted shaft eccentricity is lower than the measured shaft eccentricity for operation at shaft speeds of 6 krpm and 9 krpm and specific load ranging from 0.17 MPa to 2.1 MPa. For the majority of the test conditions the predicted results are 5 % to 30% lesser than the test result. Low loads (< 1.03 MPa) produce a high percentage difference because e is low. At high loads (> 1.03 MPa) and shaft speed varying from 9 krpm to 14 krpm, the percentage difference between the predicted and experimental results is < 20%. At 12 krpm and 2.1 MPa, the predicted eccentricity is 33 µm whereas the one measured is 35 µm (~ 6 % difference). Similarly, at 6 krpm and 2.1 MPa, the difference in predicted and measured eccentricity is ~ 20%. The uncertainty in measured (e) is ~ ± 3.5 µm.

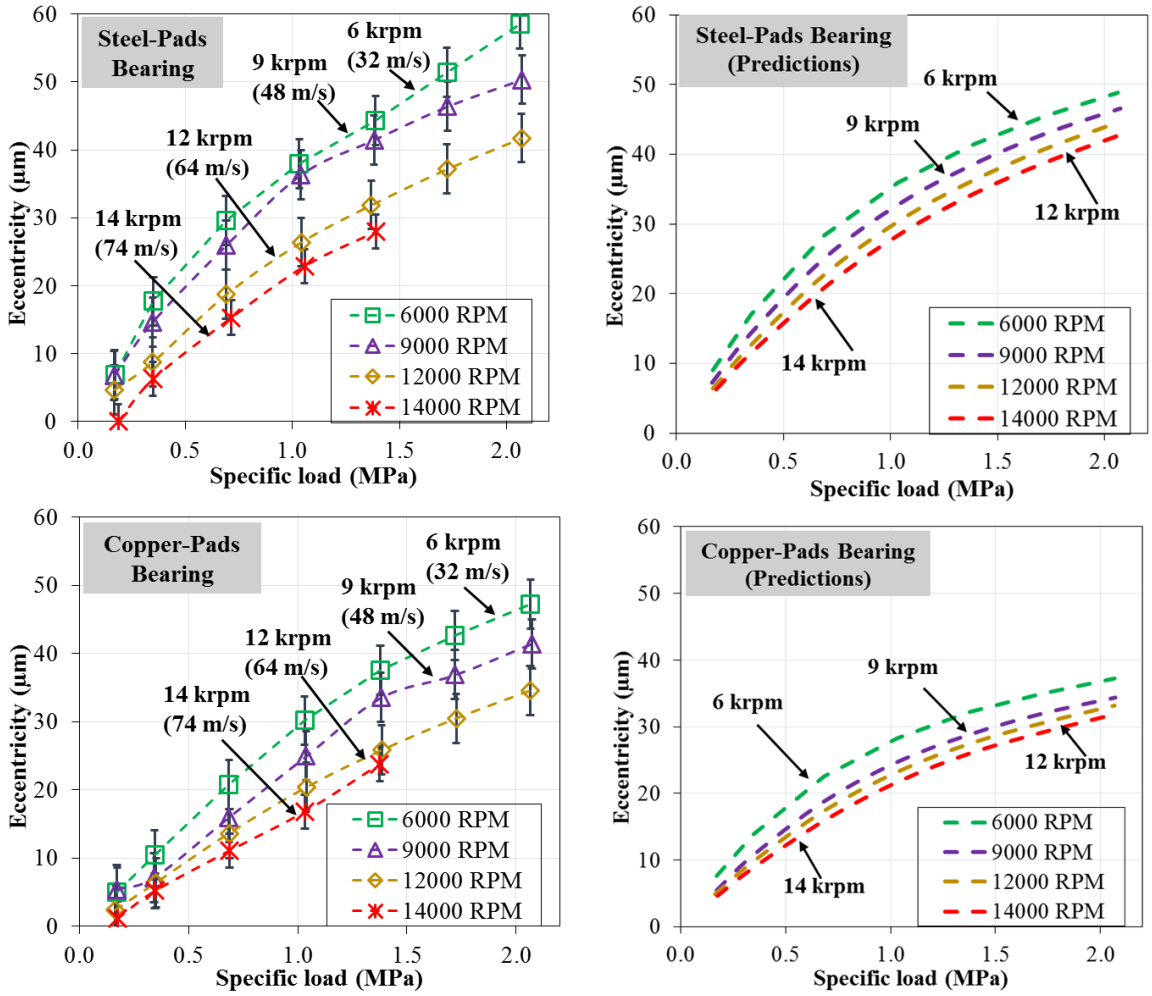

Figure 22 Measured and predicted shaft eccentricity (*e*) for (top) steel-pads bearing and (bottom) copper-pads bearing vs. specific loads (0.17 to 2.1 MPa) for operation at shaft speeds (6 to 14 krpm). Left graphs: test data, right graphs: predictions.

6.2 Shaft loci

Figure 23 presents loci of shaft position for the steel-pads bearing (S-PB) and the copper-pads bearing (C-PB). The graphs showcase the ececentricity (*e*) as a function of shaft speed, varying from 6 krpm (32 m/s) to 14 krpm (74 m/s), and as a function of specific load that ranges from 0.17 to 2.1 MPa. For both bearings the shaft displaces mainly along the +*y* (load) direction with an increase in specific load. Both bearings show small shaft displacements along the *x*-direction which indicates a small attitude angle and negligible cross-coupling stiffnesses.

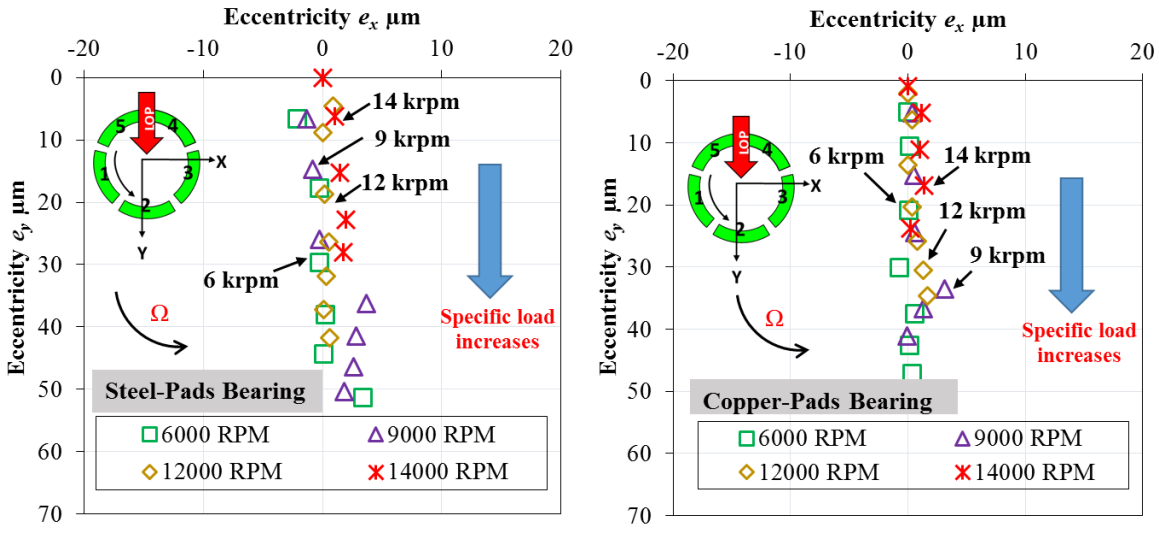

Figure 23 Shaft center loci for the (left) steel-pads bearing and (right) copper-pads bearing. Operation at various specific loads (0.17 to 2.1 MPa) and shaft speeds (6 to 14 krpm). [Cold radial clearance C_b = 63.5µm].

6.3 Attitude angle

As illustrated in Figure 18, the attitude angle (ϕ) equals:

$$\phi = \tan^{-1}\left(\frac{e_y}{e_x}\right) \tag{12}$$

where $e_x = (x_b - x_s), e_y = (y_b - y_s)$

Figure 24 shows ϕ for the steel-pads bearing (S-PB) and the copper-pads bearing (C-PB) as a function of specific load, 0.17 MPa to 2.1 MPa. The shaft operating speed ranges from 6 krpm (32 m/s) to 14 krpm (75 m/s). The attitude angle for both bearings is low (< 10º) for the specific operating conditions. At low loads (< 0.5 MPa), due to small e_x and e_y, the uncertainties are large i.e ~ ± 15°. Considering large (> 1.0 MPa) specific loads, the largest attitude angle for the S-PB is 10º at operating speed of 6 krpm (32 m/s) and 2.1 MPa specific load. For the C-PB, the largest angle is -11º at 9 krpm (48 m/s) and 1.03 MPa. Further, a low attitude angle indicates small or negligible presence of cross-coupling destabilizing forces in the TPJB.

Both S-PB and C-PB show a small attitude angle. However, at 9 krpm the C-PB operates with a relatively large attitude angle compared to that of the S-PB. At 0.7 MPa and 9 krpm, the S-PB operates at -1º while the C-PB operates at -18º. The large value of the attitude angle at low load is due to the measurement uncertainty.

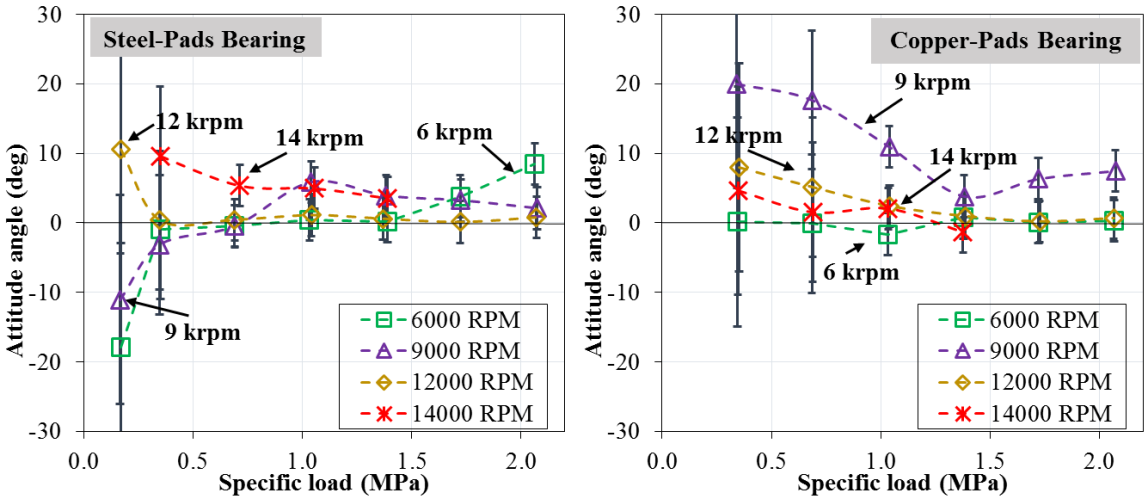

Figure 24 Measured attitude angle (degree) for (left) steel-pads bearing and (right) copper-pads bearing vs. specific load (0.17 to 2.1 MPa) for operation at various shaft speeds (6 to 14 krpm).

Figure 25 shows the predicted ϕ for the steel-pads bearing and the copper-pads bearing vs. specific loads and various speeds. The bearing operating conditions include four shaft speeds ranging from 32 m/s to 74 m/s and seven specific loads from 0.17 MPa to 2.1 MPa. Similar to the experimental results, the predicted ϕ for bearings is less < 10º.

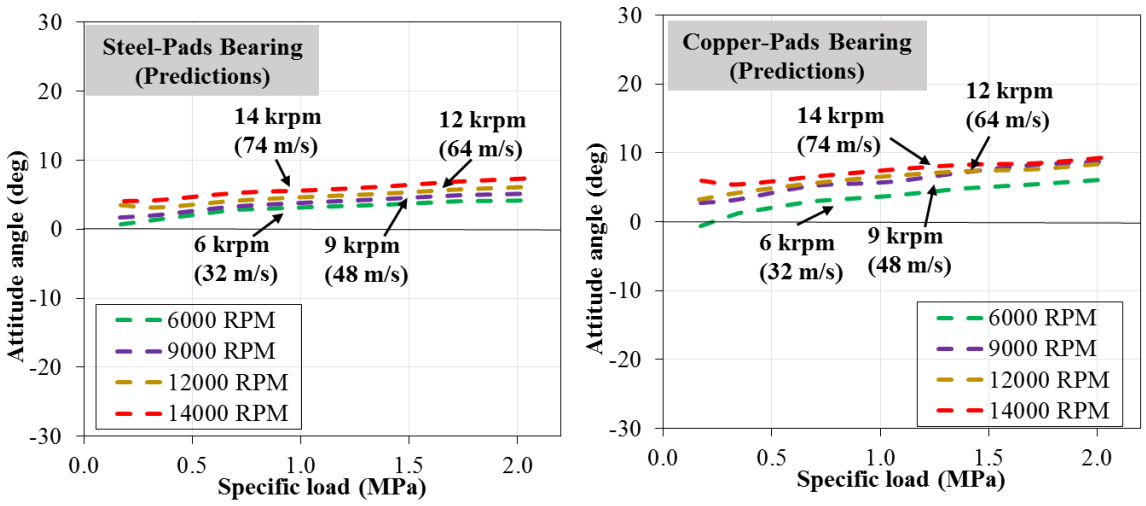

Figure 25 Predicted attitude angle (degree) for (left) steel-pads bearing and (right) copper-pads bearing vs. specific load (0.17 to 2.1 MPa) for operation at various shaft speeds (6 to 14 krpm).

6.4 Discharge Oil Temperature Rise

As shown in Figure 9, thermocouples mounted on both the drive end (DE) side and non-drive end (NDE) side of the bearing record the discharge oil temperature. The temperature rise in the DE (T_{DE}) and in the NDE (T_{NDE}) discharge oil temperature equals

$$\Delta T_{DE} = T_{DE} - T_{in} \tag{13}$$

$$\Delta T_{NDE} = T_{NDE} - T_{in} \tag{14}$$

where T_{in} = oil supply temperature (49.0 ±0.5 ºC), T_{DE} = oil discharge temperature at the drive end and, T_{NDE} = discharge temperature at the non-drive end. Figure 26 and Figure 27 show the DE and NDE oil temperature rises for the steel-pads bearing (S-PB) and the copper-pads bearing (C-PB) vs. specific load and three shaft speeds. The operating condition include shaft speeds from 6 krpm to 12 krpm (32 m/s to 64 m/s), and specific load from 0.17 MPa to 2.1 MPa. The figures show that for both bearings the oil temperature rise does not change significantly with an increase in specific load at a constant shaft speed. For example, at 9 krpm the maximum change in S-PB DE oil temperature rise is ~2ºC with an increase in load from 0.17 MPa to 2.1 MPa. However, at any specific load, the oil exit temperature raises

considerably with an increase in shaft speed. For example, at 0.69 MPa the S-PB DE oil temperature increases from 18 ºC to 24 ºC (33% relative increase) as the shaft speed increases from 9 krpm (48 m/s) to 12 krpm (48 m/s). At the same operating condition, the C-PB DE oil temperature increases from 16 ºC to 22 ºC (38 % increase) with an increase in shaft speed.

A comparison of the DE oil temperature rises for the S-PB and the C-PB shows that the S-PB runs hotter than the C-PB. As the shaft speed increases, the difference in DE oil temperature rise for the S-PB and the C-PB increases. Over the range of loads and shaft speeds, the maximum temperature difference between the DE discharge oil temperatures for the S-PB and the C-PB is ~ 6 ºC at an operating speed of 12 krpm and a specific load of 2.1 MPa.

A comparison of the NDE oil temperature rises for the S-PB and the C-PB shows an insignificant difference between the two. The maximum temperature difference over the range of operating condition is ~ 2.5 ºC at 9 krpm and 1.4 MPa. Comparison of NDE and DE temperatures of the bearings shows a slight difference depending upon the operating load and shaft speed. The difference likely denotes a misalignment in the pads. This misalignment leads to an uneven film thickness along the axial direction which results in uneven NDE and DE discharge oil temperatures.

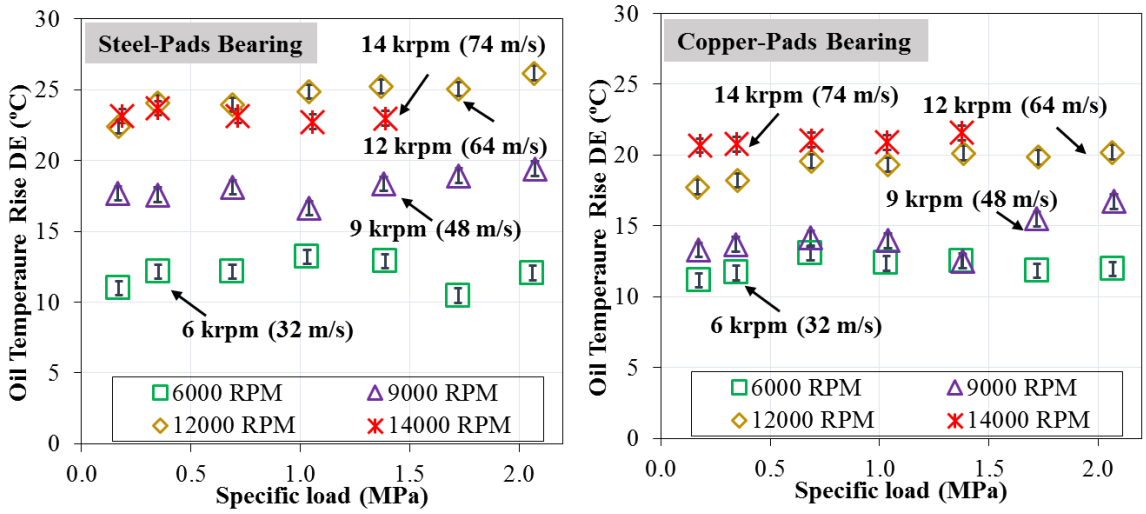

Figure 26 Measured discharge oil temperature rise (ºC) at drive-end (DE) side for (left) steel-pads bearing and (right) copper-pads bearing vs. specific load (0.17 to 2.1 MPa) for operation at various shaft speeds (6 to 14 krpm). Oil supply Temperature = 49°C.

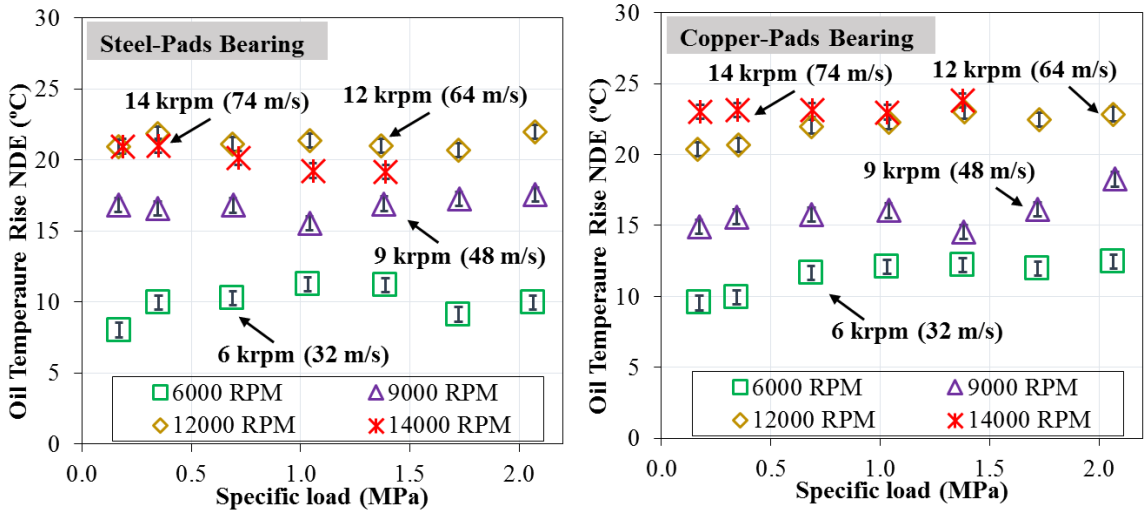

Figure 27 Measured discharge oil temperature rise (ºC) at non-drive end (NDE) side for (left) steel-pads bearing and (right) copper-pads bearing vs. specific load (0.17 to 2.1 MPa) for operation at various shaft speeds (6 to 14 krpm).Oil supply Temperature = 49°C.

6.5 Drag Power Loss

The measured power loss is derived from the product of the measured torque ($T_{bearing}$) and shaft speed (Ω). To obtain the net drag power loss in the bearing, a baseline power loss due to the frictional losses in the angular contact bearings is subtracted. The net drag power loss is given as:

$$P_{drag} = P_{measured} - P_{baseline} \tag{15}$$

$$= \left(T_{bearing} - T_{baseline}\right) \Omega$$

where $T_{bearing}$ is the torque (Nm) measured with the oil running through the test bearing. $P_{baseline}$ and $T_{baseline}$ are the drive power and torque of the shaft without the test bearing in place and without oil running through the system. Figure 28 shows the baseline torque vs. speed. It depicts that the torque magnitude is quite low (< 1 Nm). Thus, corresponding to a very low power loss from the ball bearings. The maximum torque is 0.8 Nm at 14 krpm, which gives a power loss of 1 kW. Due to a high synchronous vibration at the flexible coupling for operation at shaft speeds > 8 krpm, the torque measurements are conducted up to 8 krpm shaft speed. An assumed linear extrapolation of the baseline torque vs. speed graph yields the $T_{baseline}$ for operation at 9 krpm, 12 krpm, and 14 krpm.

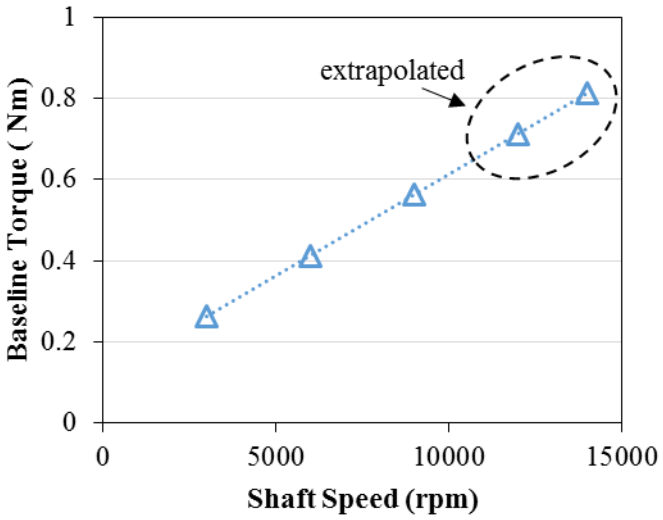

Figure 28 Measured drag torque (Nm) for operation at various shaft speeds (3 to 14 krpm) without the test bearing in place.

Figure 29 shows the measured drag power loss for the steel-pads bearing (S-PB) and the copper-pads bearing (C-PB) vs. specific load and various speeds. The operating conditions include shaft speeds from 6 krpm (32 m/s) to 14 krpm (75m/s) and specific loads from 0.17 MPa to 2.1 MPa. The power loss for both bearings shows an insignificant change with an increase in specific load. For example at 9 krpm, the drag power loss of the S-PB

changes from 5 kW to 5.7 kW with an increase in load from 0.17 MPa to 2.1 MPa (14 % increase). However, the drag power loss is a strong function of shaft speed (rotor surface speed). For example, at 0.7 MPa the drag power loss of the C-PB increases from 2.8 kW to 5.5 kW (~ 2 times) with an increase in speed from 6 krpm (32 m/s) to 9 krpm (75 m/s).

A comparison of the power loss for both bearings shows a small difference. Since both bearings have the same geometry and oil supply conditions, the measured power loss difference is expected to be insignificant. For example, at 0.35 MPa (low load) and 6 krpm (moderate speed), the power loss from the C-PB is 2.7 kW whereas that from the S-PB is 2.6 kW (~ 4% lesser). Similarly at 14 krpm (high speed) and 2.1 MPa (high load), the C-PB has 13.5 kW of power loss while the S-PB has 12.9 kW (~ 4.5% less).

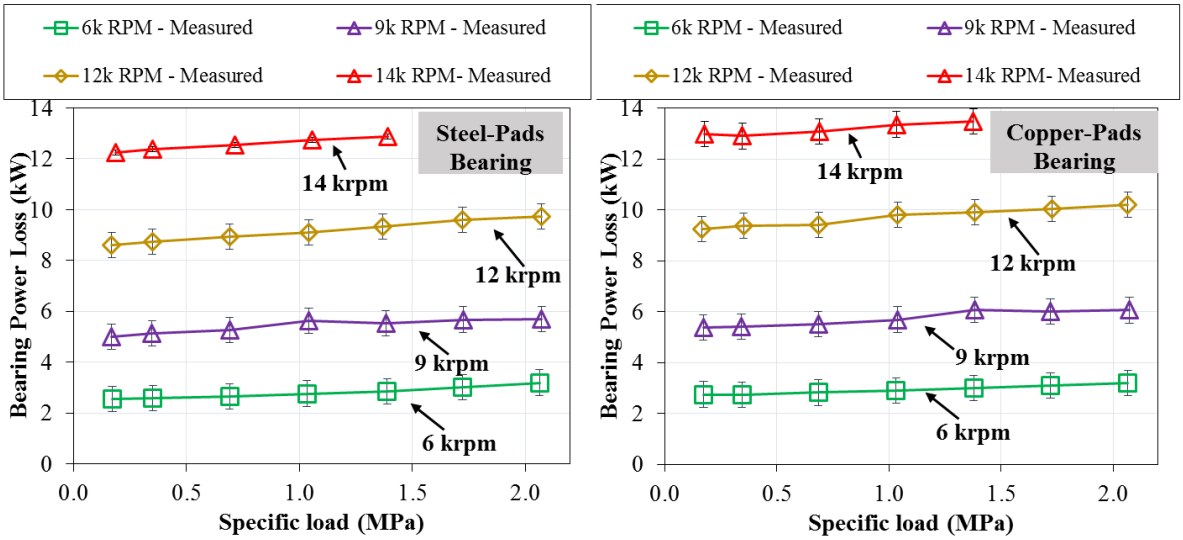

Figure 29 Measured drag power loss for (left) steel-pads bearing and (right) copper-pads bearing vs. specific load (0.17 to 2.1 MPa) for operation at various shaft speeds (6 to 14 krpm).

Figure 30 shows the estimated drag power loss for the steel-pads bearing and the copper-pads bearing vs. specific load (0.17 MPa to 2.1 MPa) for operation at multiple shaft speeds (6 krpm to 14 krpm). The estimated power loss is

$$P_{estimated} = \dot{Q}\,\Delta T_{avg}\,c_p\,\rho$$

where $\dot{Q}$ is the oil supply flow rate, ΔT_{avg} is the arithmetic average temperature of ΔT_{DE} and ΔT_{NDE}, c_p is the oil specific heat, and ρ is the oil density.

The estimated power loss of the bearings follow similar trends as compared to the measured power loss. The power loss increases with an increase in speed at a constant load and remains fairly constant with an increase in load at a specific shaft speed. For example, at 0.7 MPa the power loss in the C-PB increases from 2.6 kW to 11.6 kW (~ 3.5 times) as the shaft speed increases from 6 krpm to 14 krpm. In contrast at 14 krpm, the power loss increases from 11.2 kW to 11.4 kW (~2 % increase) as the load increases from 0.17 MPa to 2.1 MPa.

Further, a comparison of the estimated power loss of the bearings show an insignificant difference. For example at 0.7 MPa (low load) and 6 krpm (low speed), the C-PB power loss is 2.6 kW while the S-PB power loss is 2.3 kW (~ 11% relative difference). Similarly, at 1.7 MPa (high load) and 12 krpm (high speed), the difference in power loss is ~ 7%.

Figure 31 shows the ratio (ψ) of the estimated and the measured power loss for the S-PB and the C-PB. The ratio gives an empirical parameter to find the actual power loss based on the estimated power loss. The figure shows that for the C-PB ψ = ~ 0.9 for a majority of the test cases. Similarly, for the S-PB ψ ranges from 0.9 to 1.0. Thus, based on the test results, ψ = ~ 0.9 could be used.

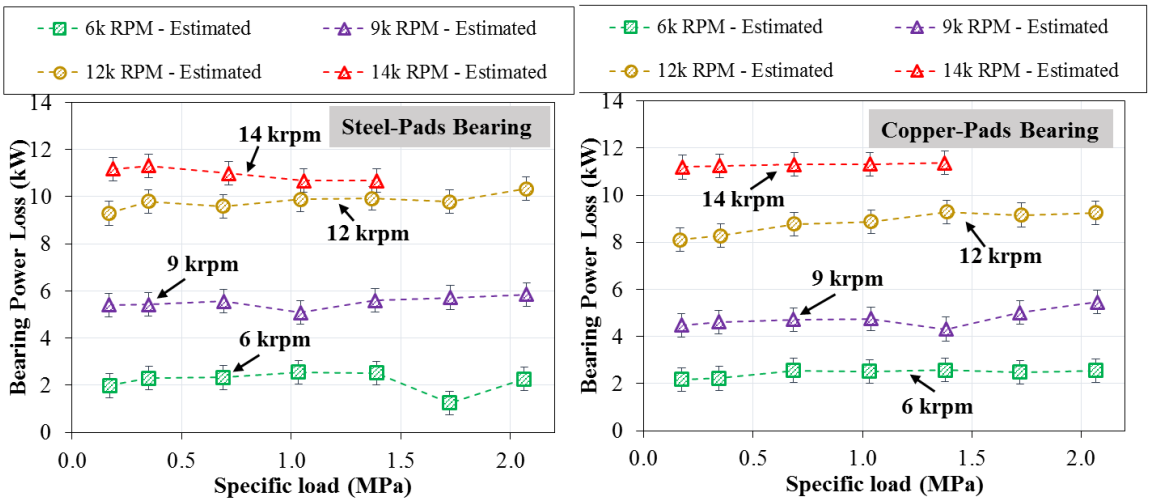

Figure 30 Estimated drag power loss for (left) steel-pads bearing and (right) copper-pads bearing vs. specific load (0.17 to 2.1 MPa) for operation at various shaft speeds (6 to 14 krpm)

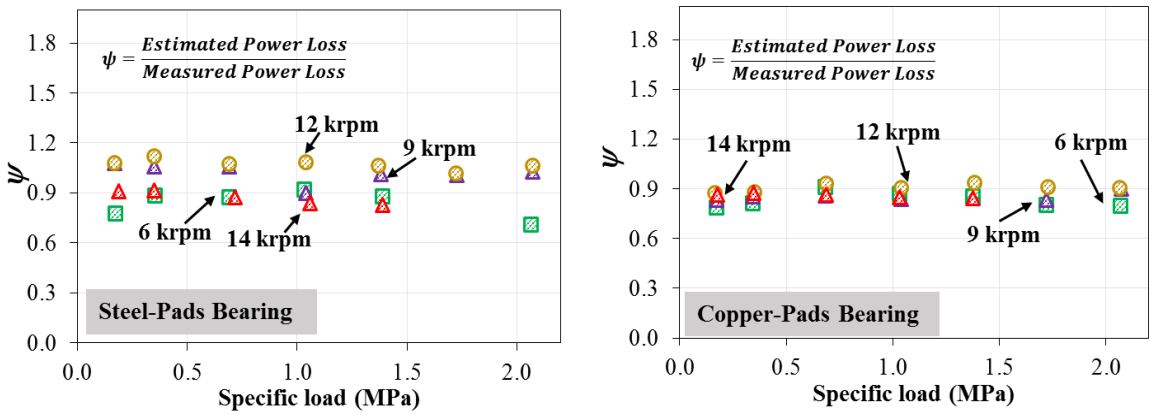

Figure 31 Ratio of estimated to measured power loss (ψ) for (left) steel-pads bearing and (right) copper-pads bearing vs. specific load (0.17 to 2.1 MPa) and various shaft speeds (6 to 14 krpm).

Figure 32 shows the dimensionless drag power loss at various shaft speeds (6 to 14 krpm) and specific loads (0.17 to 2.1 MPa). The dimensionless drag power loss, also discussed by Jani [38], is

$$P^* = \frac{P_{drag}}{P_{analytical}} \tag{16}$$

$$P_{analytical} = \frac{\Omega^2 D^3 L\, \mu_{eff}}{8\, C_b}\ (n_p\, \theta_p) \tag{17}$$

where, Ω is the shaft speed (rad/s), D is the shaft diameter, L is the bearing pad axial length, μ_{eff}[18] is the effective fluid viscosity at T_{ref}, n_p is the number of pads, θ_p is the pad arc angle (radians) and C_b is the nominal bearing radial clearance at 25 ºC.

P^* for both bearings ranges from 0.9-1.3. $P^* > 1$ means $P_{drag} > P_{analytical}$. The difference is likely because $P_{analytical}$ uses the cold bearing radial clearance (C_b = 63.5 µm) whereas the actual bearing clearance (*hot* clearance) during test is smaller than the nominal bearing clearance.

[18] $\mu = \mu_{ref}\, e^{-\alpha_{vis}(T_{eff} - T_{ref})}$, $T_{eff} = T_{in} + 0.75(T_{discharge} - T_{in})$

Further, a comparison of the C-PB and the S-PB power loss shows an insignificant difference. For example at 0.35 MPa (low load) and 6 krpm (low speed) the C-PB yields ~ 5% higher (dimensionless) power loss.

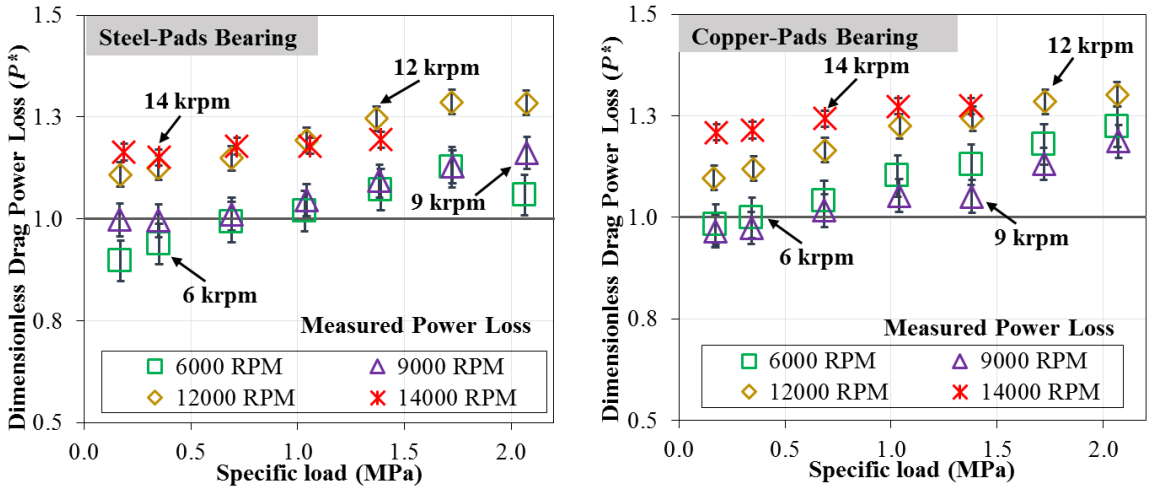

Figure 32 Dimensionless drag power loss for (left) steel-pads bearing and (right) copper-pads bearing vs. specific load (0.17 to 2.1 MPa) for operation at various shaft speeds (6 to 14 krpm).

6.6 Reynolds Number

The nominal circumferential Reynolds number (R_e) is

$$R_e = \frac{\rho\, \Omega\, R\, C_b}{\mu_{eff}} \tag{18}$$

where ρ is the fluid density at room temperature, Ω is the shaft speed, R is the shaft diameter, C_b is the bearing clearance measured at room (cold) temperature, and μ_{eff} is the effective lubricant viscosity[19] at an estimated effective temperature (T_{eff}). The oil density varies by ~ 1% with T_{eff} whereas the fluid viscosity varies by a maximum of 30 % over the range of T_{eff}.

The Reynolds number is the ratio of fluid inertial force to fluid viscous force. R_e >2,000 indicates a turbulent flow regime whereas R_e < 2,000 denotes a laminar flow regime [39]. Figure 33 shows the circumferential Reynolds number (R_e) for the steel-pads bearing and the copper-pads bearing vs. bearing specific load of (0.17 to 2.1 MPa) for operation at

[19] $\mu_{eff} = \mu_{ref}\, e^{-\alpha_{vis}(T_{eff}-T_{ref})}$, $T_{eff} = T_{in} + 0.75(T_{discharge} - T_{in})$

shaft speeds ranging from 32 m/s (6 krpm) to 74 m/s (14 krpm). Note R_e is a linear function of shaft speed.

For both the S-PB and the C-PB, the shear flow Reynolds number is well below 2,000; hence the flow regime within the bearing pads is laminar. Also note that C_b/R =0.0012, which produces a modified Reynolds number $R_e^* = R_e\,(C_b/R) < 1$.

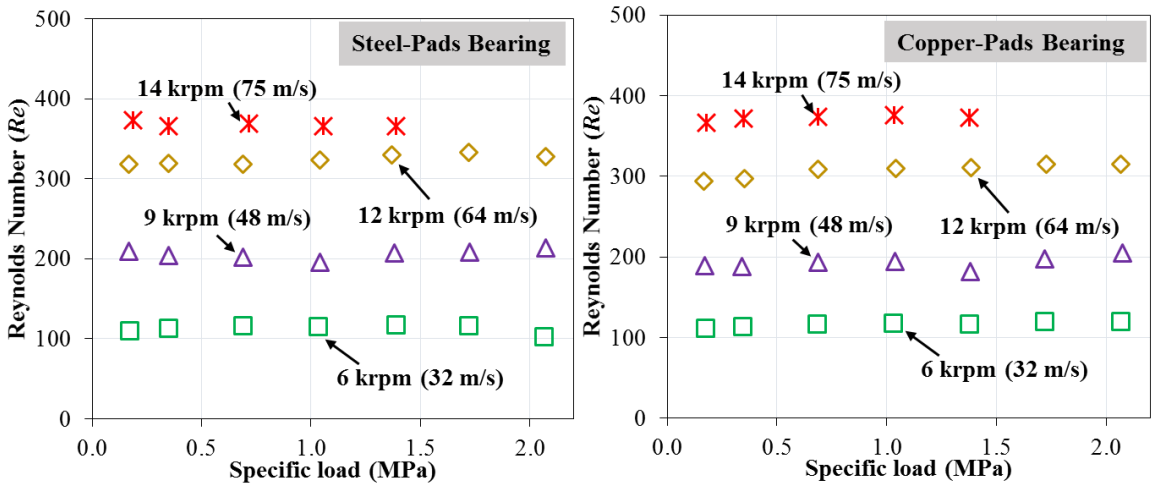

Figure 33 Circumferential Reynolds Number (R_e) for (left) steel-pads bearing and (right) copper-pads bearing vs. specific load (0.17 to 2.1 MPa) for operation at various shaft speeds (6 to 14 krpm). C_b/R =0.0012

6.7 Bearing Pad Temperatures

The dimensionless pad defect temperature (θ) is

$$\theta = \frac{T_{pad} - T_{in}}{T_{discharge} - T_{in}} = \frac{\Delta T_{pad}}{\Delta\, T_{oil}} \tag{19}$$

where T_{pad} is the recorded sub-pad surface (2.5 mm below) pad temperature, T_{in} is the oil supply temperature (49 ºC for all test conditions), and $T_{discharge}$ is the arithmetic average of the drive end (T_{de}) and non-drive end (T_{nde}) discharge oil temperatures.

The pad defect temperature (θ) gives the pad temperature rise (ΔT_{pad}) relative to the discharge oil temperature rise ($\Delta\, T_{oil}$). For example θ = 3 indicates that the pad temperature

rise is three times the oil discharge temperature rise. For θ = 3 and ΔT_{oil}= 20 ºC, the pad temperature rise ΔT_{pad} = 60 ºC.

As shown in Figure 13, 30 thermocouples installed ~ 2.5 mm below a pad surface record the temperatures. The figure shows that each pad has six thermocouples: four embedded circumferentially at 10%, 25%, 75 % and 90 % of the pad arc length and two located axially at 75 % pad arc length.

Figure 34 shows the circumferential defect temperatures (θ) for the steel-pads bearing and the copper-pads bearing. The dotted vertical lines enclose each pad with four thermocouples. The figure maps out the complete temperature profile of the bearing pads from 0º (pad #1 leading edge thermocouple) to 345º. Recall that pad # 2 is along the load direction. The operating conditions correspond to shaft speed from 6 krpm (32 m/s) to 14 krpm (74 m/s) and bearing specific load equal to 0.35 MPa.

For the steel-pads bearing, except for pad # 2, each of the pads' leading edge temperature (10% of arc length) is below one. Since cold oil is injected between each pair of pads, the leading edge of the pads has a low ΔT_{pad}. In each pad, the temperature continues to rise from the leading edge towards the trailing edge as the fluid is sheared between the spinning journal and the pad surface. Recall, Eq. (16) indicates that the bearing drag power loss, which produces the fluid and pad temperature rise, is propotional to Ω. Thus, with an increase in shaft speed, the pad temperature must increase. But as shown in Figure 34 (top graph), the defect temperature (θ) for operation at 6 krpm is higher for all steel-pads compared to those at other shaft speeds. The actual pad temperature is lower at 6 krpm, since ΔT_{oil} at 6 krpm = 11ºC compared to 15ºC, 19 ºC and 22 ºC for 9 krpm, 12 krpm and 14 krpm. As shown in Figure 34 (top graph), the maximum θ for the steel-pads bearing is at the 75% arc length of pad # 2 with θ_{max} = 2.5, 2.0, 1.7 and 2.0 for 6 krpm (32 m/s), 9 krpm (48 m/s), 12 krpm (64 m/s) and 14 krpm (74 m/s), respectively. This results in ΔT_{pad} = 28 ºC, 34 ºC, 39 ºC and 44 ºC for the corresponding shaft speeds. Further, it shows that an increase in shaft speed from 6 krpm (32 m/s) to 14 krpm (74 m/s) the maximum pad temperature increases by ~ 57%.

The copper-pads bearing temperature profile (see bottom graph in Figure 34) follows a similar trend as that in the steel-pads bearing. The temperature rises from the leading edge to the trailing edge of each pad. Pad # 2 has the highest θ as it is the loaded pad and experiences the largest lubricant shear (smallest film thickness). As both the steel-pads bearing and the copper-pads bearing have the same ΔT_{oil} at 6 krpm, a comparison for ΔT_{pad} can be directly made by comparing θ. For example, at 6 krpm, θ for the pad # 2 leading edge temperature (thermocouple at 10% arc length) is 1.4 for the copper-pads bearing and θ = 1.0 for the steel-pads bearing. This difference in θ indicates a 40 % higher temperature for the copper-pads. Moreover, compared to the steel-pads bearing, a larger θ for the copper-pad bearing indicates a higher hot oil carryover which leads to a higher leading edge temperatures[20].

The maximum pad defect temperature (θ_{max}) occurs on the loaded pad # 2 for both bearings. For the steel-pads bearing it occurs at the 75 % pad arc length whereas for the copper-pads bearing it occurs at 90 % pad arc length. For operation at 6 krpm (32 m/s) and 9 krpm (48 m/s), the copper-pads bearing operate at θ_{max} = 2.3 (25 ºC ΔT_{pad}) and 1.9 (29 ºC ΔT_{pad}), respectively. Whereas, for the steel-pads bearing, θ_{max} = 2.5 (28 ºC ΔT_{pad}) and 2.0 (34 ºC ΔT_{pad}) at 6 krpm and 9 krpm, respectively. Thus, the copper-pads bearing runs cooler than the steel-pads bearing for operation at 32 m/s and 48 m/s. At a high shaft speed of 12 krpm (64 m/s) and 14 krpm (74 m/s), both bearings have about the same ΔT_{pad} i.e ~ 38 ºC at 12 krpm and 44 ºC at 14 krpm, respectively.

[20] Both bearings receive the same speed-dependent oil flow rates.

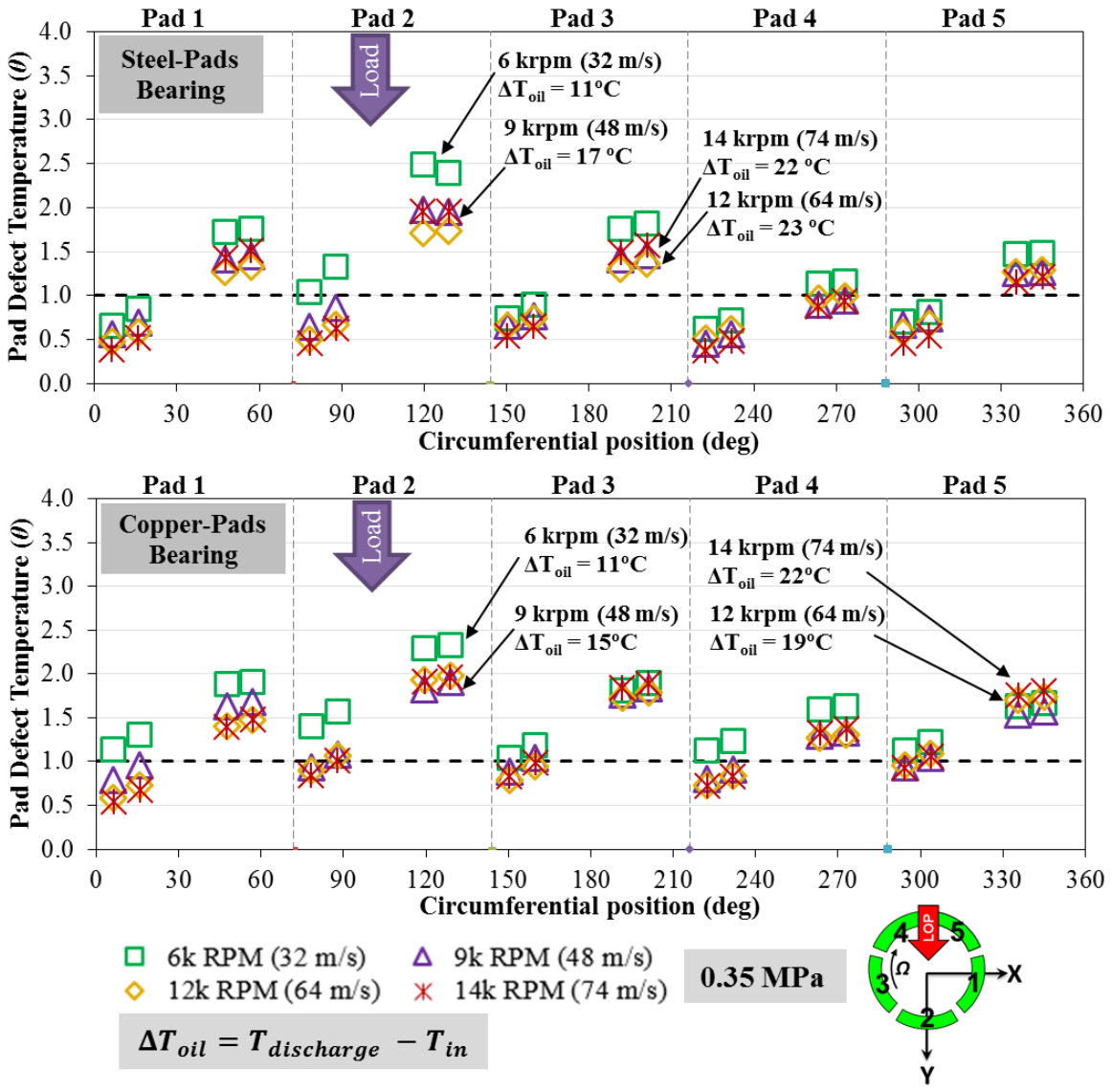

Figure 34 Measured pad defect temperature (θ) for (top) steel-pads bearing and (bottom) copper-pads bearing at various circumferential locations along mid-plane and operation at 0.35 MPa specific load and four shaft surface speeds (32-74 m/s).

Figure 35 shows the circumferential pad defect temperatures (θ) for the steel-pads bearing and the copper-pads bearing for operation at shaft speeds ranging from 32 m/s (6 krpm) to 64 m/s (12 krpm), and bearing specific load of 2.1 MPa. Compared to the low load (0.35 MPa) operation, the maximum θ is higher for the bearing under a 2.1 MPa specific load. For example, for operation at 6 krpm and 0.35 MPa θ_{max} = 2.5 (28 ºC) and 2.3 (25 ºC) for the S-PB and the C-PB, respectively. A load increment of 2.1 MPa results in θ_{max} = 4.0 (44 ºC) and 3.0 (36 ºC) for the S-PB and the C-PB, respectively.

A comparison of the S-PB and the C-PB loaded pad (#2) leading edge θ (thermocouple at 10% of arc length) shows that for operation at low speed (32 m/s), θ is higher for the steel-pads bearing (2.2) than that for the C-PB (2.0). For operation at a high shaft speed of 64 m/s the C-PB θ is higher, i.e, 1.4 vs 1.0 for the S-PB. For each θ, the corresponding ΔT_{pad} also follows the same trend. The pad leading edge θ*'s* show that the hot oil carryover factor (λ)[21] for the S-PB is larger at low shaft speed and smaller at a high shaft speed. Note that, the carryover factor for the C-PB may be smaller at a low shaft speed and larger at a high shaft speed.

The unloaded pads'(#4 and #5) leading edge θ decreases with an increase in load from 0.35 MPa to 2.1 for both the C-PB and S-PB. For example, for operation at 6 krpm, θ for S-PB pad #4 drops from 0.6 to 0.3 (50 % relative drop) as the specific load increases from 0.35 MPa to 2.1 MPa. Similarly for the C-PB, θ decreases from 1.1 to 0.5 (~ 55 % relative drop). With an increase in load, the operating clearance between the unloaded pads and the shaft increases. The clearance increase allows for more oil flow between the pads and the shaft and hence lowers the pad leading edge temperatures.

[21] The carryover factor (λ) is the fraction of hot oil carried over from the upstream pad into the downstream pad.

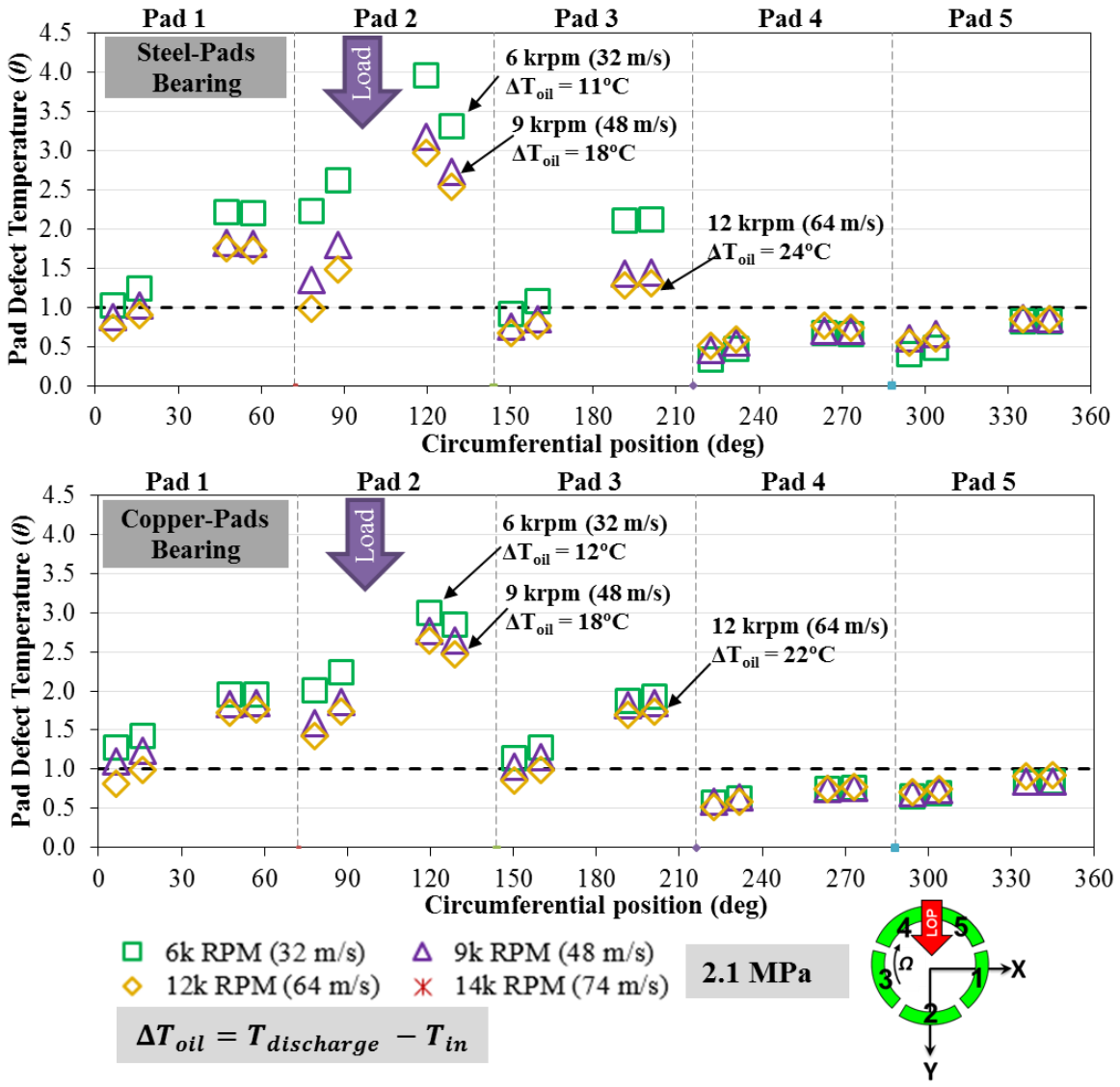

Figure 35. Measured pad defect temperature (θ) for (top) steel-pads bearing and (bottom) copper-pads bearing at various circumferential locations along mid-plane and operation at 2.1 MPa specific load and three shaft surface speed (48-64 m/s).

Figure 36 details the pads defect temperature (θ) along the axial direction for the steel-pads bearing and the copper-pads bearing. As shown in Figure 13, each pad at 75% of the pad arc length has two axial thermocouples and one circumferential thermocouple embedded 2.5 mm below the pad surface. The pad defect temperatures shown in Figure 36 are derived from the temperatures acquired through the axial thermocouples shown in Figure 13. In the figure, NTS = Non-drive end thermocouple, C = Center thermocouple, and TS =

Drive-end thermocouple. The operating conditions include four shaft speeds ranging from 32 m/s (6 krpm) to 74 m/s (14 krpm), and a specific load of 0.35 MPa (low load).

Both the S-PB and the C-PB shows pad misalignment of the loaded pad #2. The S-PB has a higher θ at the NTS side while the C-PB has it on the TS side. Moreover, for the S-PB the change[22] in θ along the axial direction, i.e. $\Delta\theta$ = 0.4 is constant over the range of operating shaft speed whereas for the C-PB $\Delta\theta$ it varies form 0.2~0.4. Since spherical pivoted pads can self-align axially, a small $\Delta\theta$ indicates a good alignment of a rotor with respect to a pad.

Considering the unloaded pads, pad # 1 and #3 of the S-PB show $\Delta\theta$ = 0.3 and 0.2 respectively. Pad # 4 and pad #5 show a negligible defect temperature difference along the axial direction. All the unloaded pads of the C-PB, except for pad # 3 ($\Delta\theta$ = 0.4), show insignificant difference in θ along the axial direction.

[22] The maximum difference in θ along a pad axial length is represented as $\Delta\theta=\theta_{max}-\theta_{min}$, where θ_{max} is the maximum θ and θ_{min} is the minimum θ along the pad length.

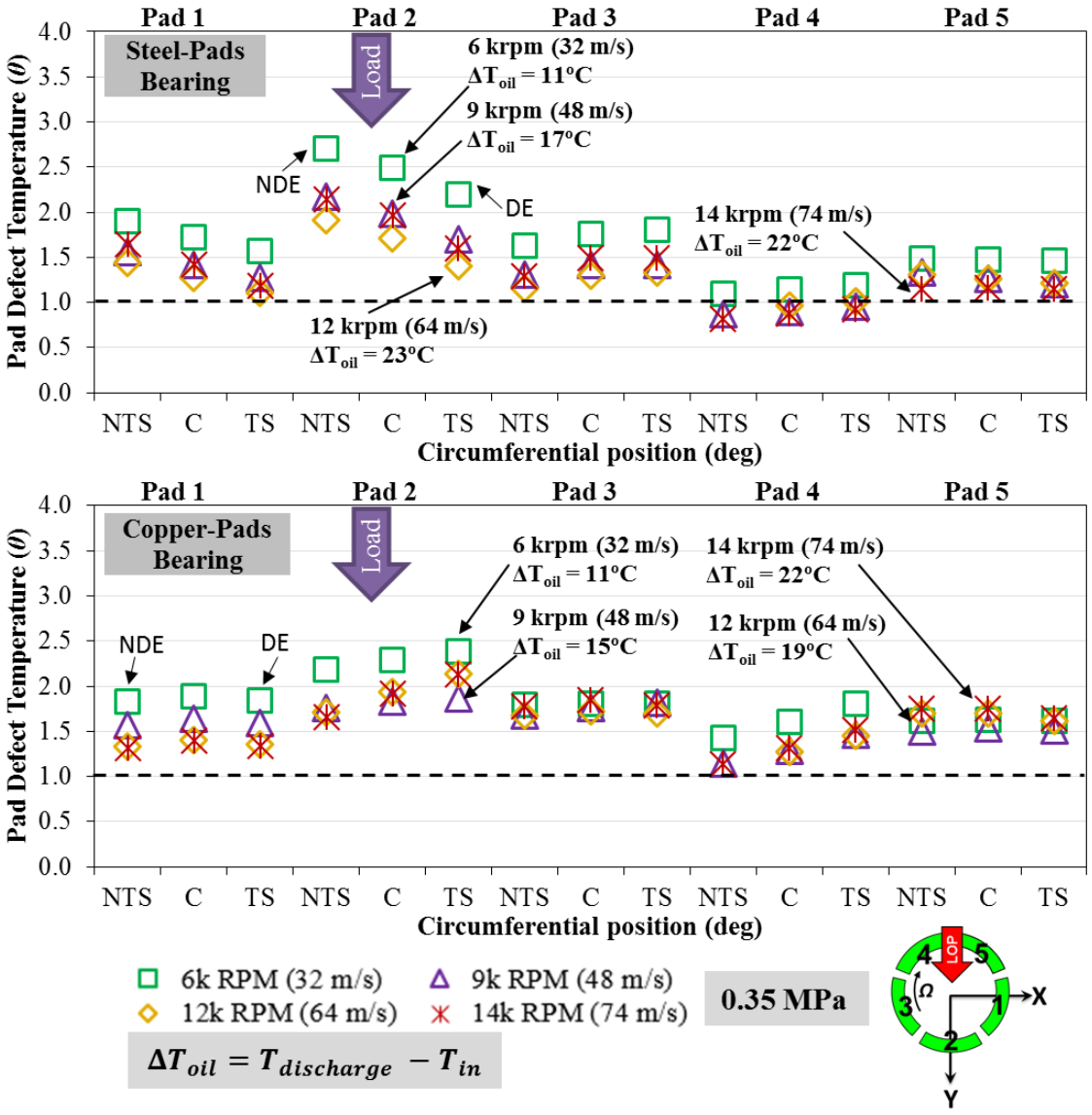

Figure 36 Measured pad defect temperature (θ) for (top) steel-pads bearing and (bottom) copper-pads bearing along the axial direction at 75% pad arc length for operation at 0.35 MPa specific load and four shaft surface speed (32-74 m/s).

Figure 37 presents the pad defect temperatures along the axial direction for the steel-pads bearing and the copper-pads bearing. The operating conditions include three shaft speeds ranging from 32 m/s (6 krpm) to 64 m/s (12 krpm), and a bearing specific load of 2.1 MPa. Figure 37 shows that for both bearings, the maximum $\Delta\theta$ is 0.4 and it occurs at the loaded pad # 2. For the S-PB the maximum θ occurs at the NTS side whereas for the C-PB it occurs at the TS side.

For the S-PB, the unloaded pads show a small change in θ, i.e. $\Delta\theta$ ranges from 0.3-0.4. This difference in θ corresponds to a very small axial temperature difference of ~ 3-4 ^{o}C. In contrast to that, all the unloaded pads of the C-PB show negligible defect temperature gradient. Thus indicating good pad-rotor alignment.

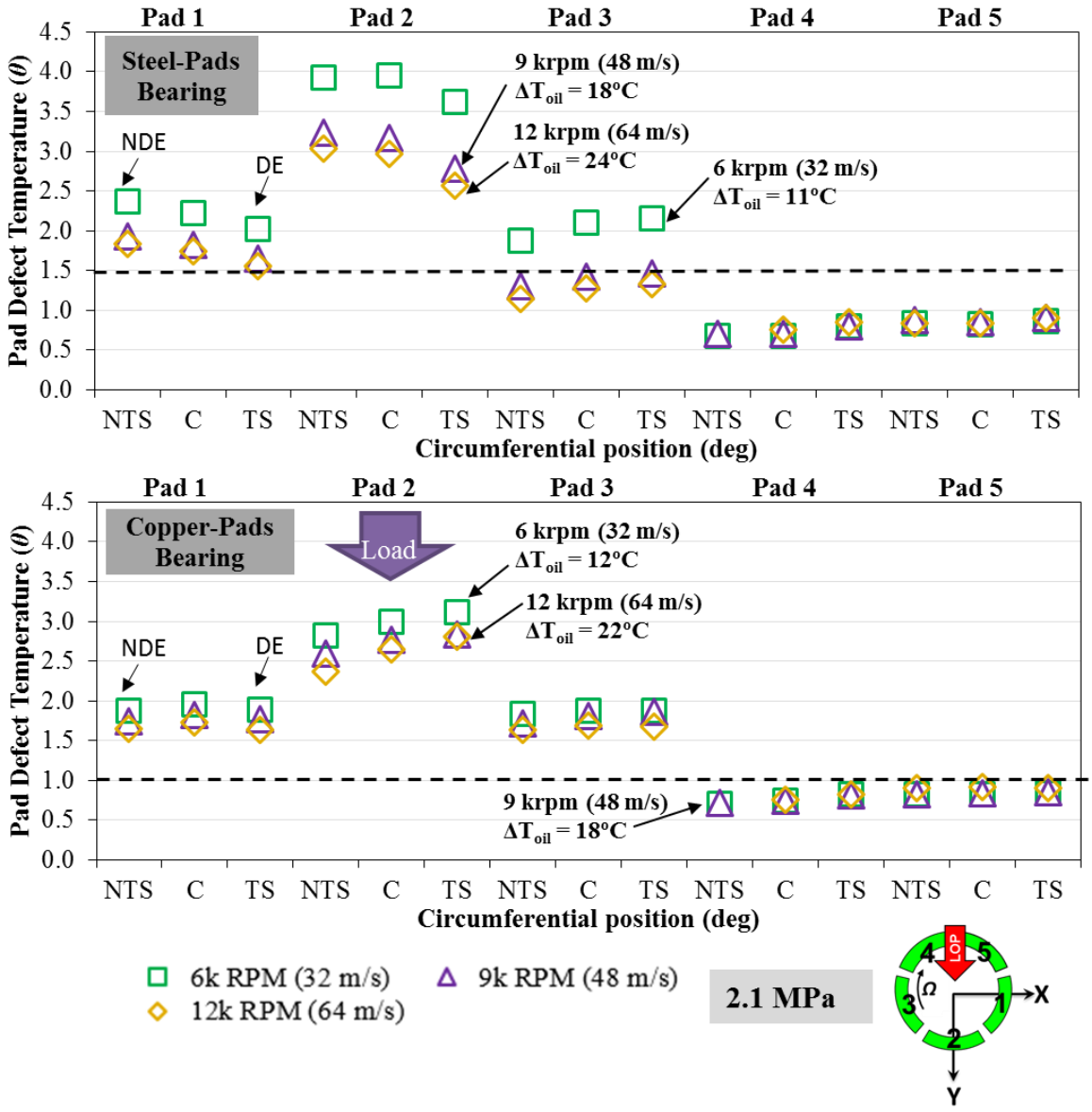

Figure 37 Measured pad defect temperature (θ) for (top) steel-pads bearing and (bottom) copper-pads bearing along the axial direction at 75% pad arc length for operation at 2.1 MPa specific load and three shaft surface speed (48-64 m/s).

6.7.1 Comparison of the Measured and Predicted Pad Temperatures

Figure 38 details the measured and predicted pad defect temperatures (θ) for the steel-pads bearing. The bearing operating conditions include a 0.35 MPa bearing specific load, four shaft operating speed ranging from 32 m/s (6 krpm) to 74 m/s (14 krpm), and a 49 ºC oil supply temperature.

A comparison of the maximum measured and predicted pad temperatures shows that the predicted pad temperatures are greater than the measured pad temperatures for operation at shaft speeds of 32 m/s. For example, the maximum measured pad defect temperature is 2.5 as compared to the predicted θ of 2.7 (8 % higher). However, at the high speed operation (74 m/s) the predicted maximum θ is lower than the measured θ (10 % difference).

The predicted pad temperatures follow the same trend as the measured temperature profile. With an increase in speed, as the oil shear rate increases, the pad temperature increases. For example, the maximum pad temperature rise ΔT_{pad} = 29 ºC at 32 m/s, whereas at 48 m/s ΔT_{pad} increases to 39 ºC. One more thing to notice is the maximum pad defect temperature. Similar to the measured temperatures, at each operating speed, pad # 2 (loaded) has the maximum predicted θ.

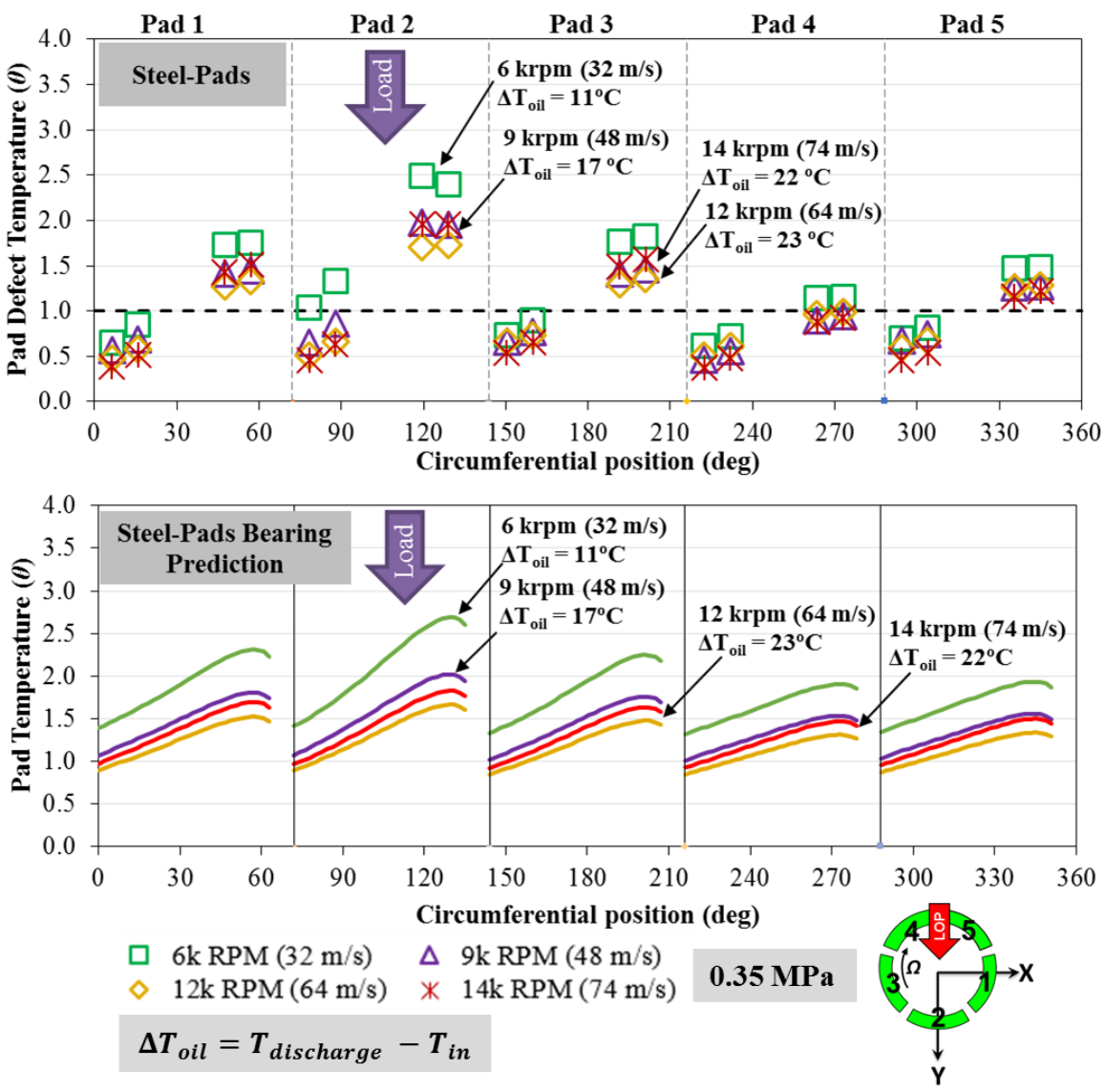

Figure 38 Measured (top) and predicted (bottom) pad defect temperature (θ) for steel-pads bearing at various circumferential locations along mid-plane and operation at 0.35 MPa specific load and four shaft surface speeds (32-74 m/s).

Figure 39 compares the measured and the predicted pad defect temperatures (θ) for the copper-pads bearing. The bearing operating conditions include a 0.35 MPa bearing specific load, four shaft operating speed ranging from 32 m/s (6 krpm) to 74 m/s (14 krpm), and a 49 ºC oil supply temperature.

The figure shows that the analytical results over predict the leading edge (10 % and 25 % of arc length) temperatures over the range of operating speeds. At 32 m/s, the leading edge predicted θ is ~ 20 – 30 % larger than the measured θ. The predicted $\theta > 1$ at the pads

leading edge is the result of the hot oil being carried over from the upstream pad to the downstream pad. There are two factors which effect the leading edge pad temperatures; the upstream pad temperature and the amount of oil being carried over from the downstream pad to upstream pad. The figure shows that the difference between the measured and predicted trailing edge temperature is significant. Thus, the predictive computational model overestimates the heat carry over factor (λ) oil flow which results in a predicted $\theta > 1$.

At each operating speed, pad # 2 (loaded pad) yields the maximum θ for both predicted and measured temperature data. At 32 m/s, the analytical results over predicts the maximum pad defect temperature i.e. measured θ_{max} = 2.3 and predicted θ_{max} = 2.6 (13 % larger). However, the difference keeps on decreasing with an increase in shaft speed. At 48 m/s, both predicted and the measured θ_{max} equal to 1.9.

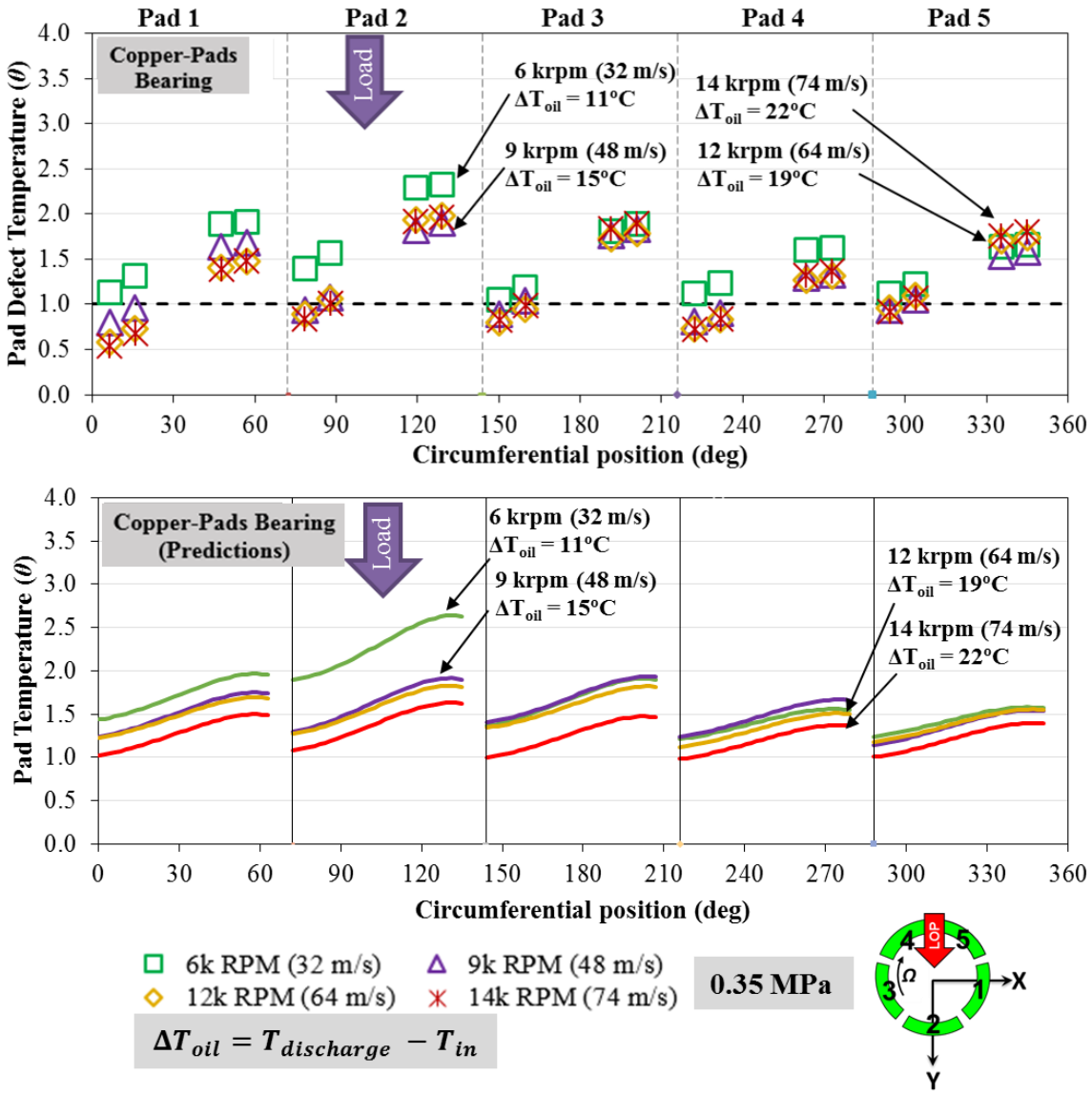

Figure 39 Measured (top) and predicted (bottom) pad defect temperature (θ) for copper-pads bearing at various circumferential locations along mid-plane and operation at 0.35 MPa specific load and four shaft surface speeds (32-74 m/s).

Figure 40 details the measured and predicted pad defect temperatures (θ) for the steel-pads bearing. The bearing operating conditions include a 1.38 MPa bearing specific load, three shaft operating speed ranging from 64 m/s (9 krpm) to 74 m/s (14 krpm), and a 49 ºC oil supply temperature.

A comparison of the measured and predicted θ shows that, except for operation at 9 krpm (48 m/s), the predictive code overestimates the leading edge pads' temperatures. For

example at 14 krpm (74 m/s), the loaded pad measured leading edge θ = 0.7 whereas the predicted θ = 1.4 (2 times). The larger θ is result of the overestimated hot oil carryover from the upstream pad to the downstream pad. In contrast to the leading edge temperatures, the code slightly under predicts the loaded pad $\theta_{max.}$ For operation at 12 krpm (64 m/s), the measured θ_{max} = 2.7 whereas the predicted θ_{max} = 2.5.

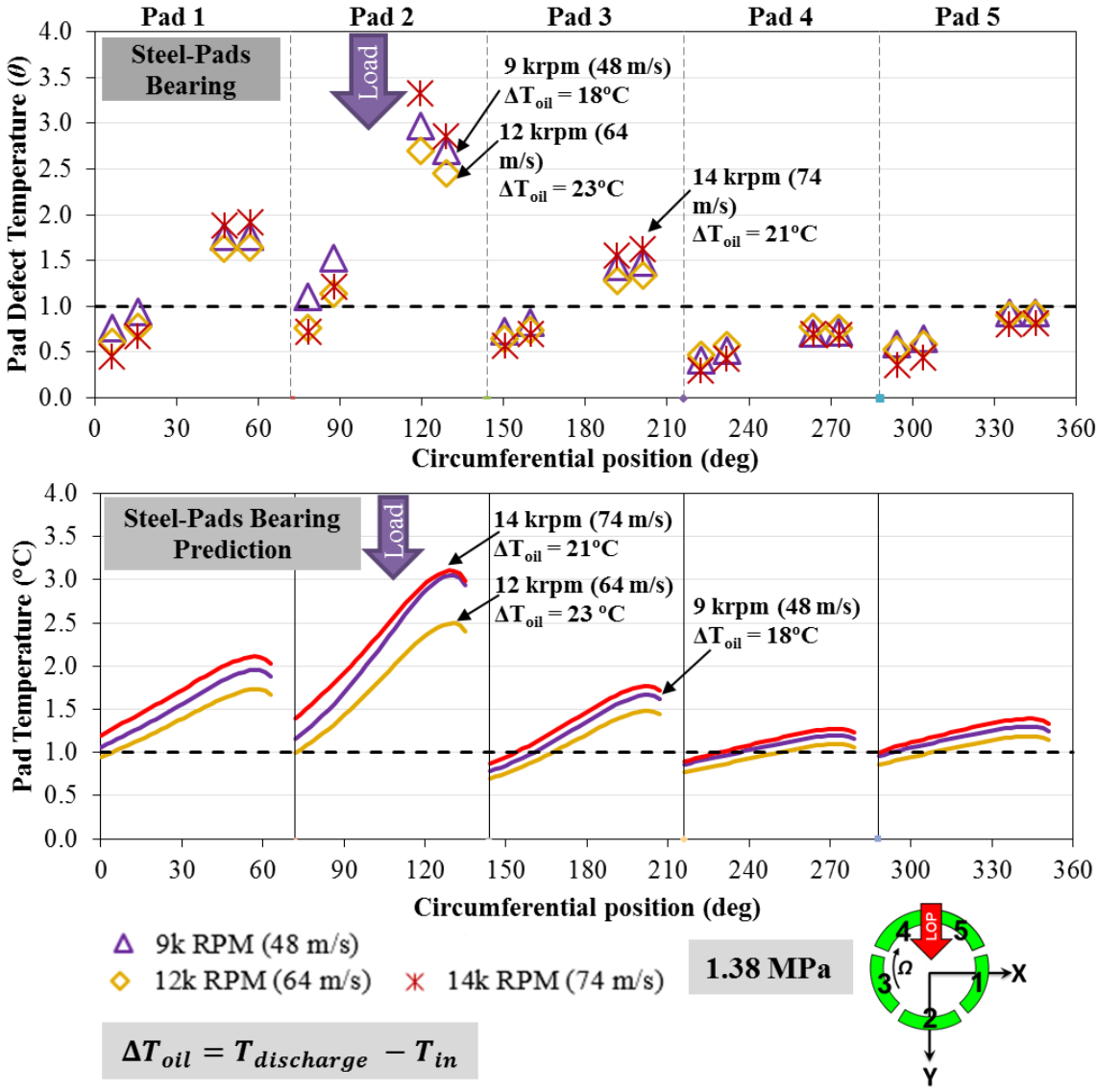

Figure 40 Measured (top) and predicted (bottom) pad defect temperature (θ) for steel-pads bearing at various circumferential locations along mid-plane and operation at 1.38 MPa specific load and four shaft surface speeds (48-74 m/s).

Figure 41 presents both the measured and predicted pad defect temperatures (θ) for the copper-pads bearing (C-PB). The bearing operating conditions include shaft speed varying from 9 krpm (48 m/s) to 14 krpm (74 m/s) and specific load of 1.38 MPa.

The predicted θ follows the same trend as the measured θ, however, the predictive code over estimates the leading edge temperatures of all five pads (10 % of arc length). For example, for operation at 9 krpm (48 m/s) the leading edge measured θ = 1.4 whereas the θ from predictions is 1.8 i.e ~ 28 % high. The difference in θ decreases with an increase in speed such that at 12 krpm (64 m/s) shaft speed, the predicted θ = 1.4 whereas the θ from measurements is 1.2 i.e. ~ 14 % larger.

Unlike the measured data, as shown in Figure 40 and Figure 41, the analytical results yield the leading edge $\theta > 1$. The larger value of θ shows that the code overestimates the hot oil carry over from an upstream pad to the (next) downstream pad.

A comparison of the results show that the difference between the θ_{max} of the predicted and measured results is small. For example at 14 krpm (74 m/s), the θ_{max} from measurements is 2.4 whereas θ_{max} from the prediction is ~ 2.5.

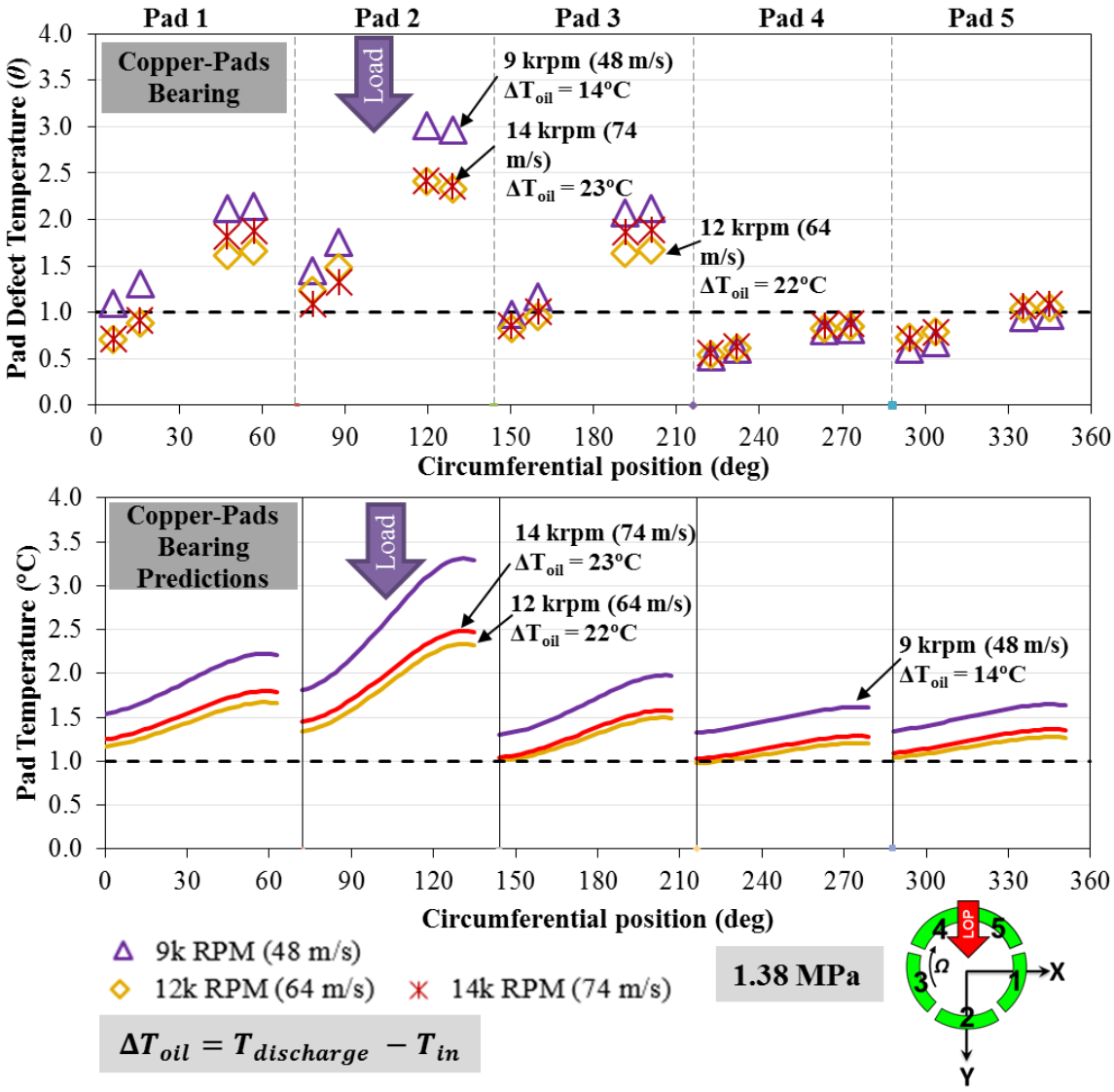

Figure 41 Measured (top) and predicted (bottom) pad defect temperature (θ) for copper-pads bearing at various circumferential locations along mid-plane and operation at 1.38 MPa specific load and four shaft surface speeds (48-74 m/s).

7. BEARINGS' DYNAMIC LOAD CHARACTERISTICS

As the system achieves a thermal steady state at an operating test point, the operator activates the DAQ system through a LabVIEW program. The program triggers the hydraulic shaker heads and dynamically excites the stator-bearing assembly with a pseudo-random waveform. Each excitation consists of frequency ranging from 10 Hz to 320 Hz with increments of 10 Hz. Thus, equaling to 32 excitation altogether. To check the repeatability of the data the same process is repeated 10 times. Thus, in total there are 320 excitations. Initially the shakers excite (320 excitations) the system along the *x*-direction and then the same process is repeated along the *y*-direction. As discussed in the "parameter identification model" section, conversion of the time-domain data into the frequency domain and the curve fitting data on to a KCM model yields the dynamic force coefficients (stiffness, damping and virtual-mass) of the bearing. The real part of the complex dynamic stiffness $(K - \omega^2 M)$ gives a stiffness (K) and a virtual-mass (M) coefficient, whereas the imaginary part of the complex dynamic stiffness (ωC) gives a damping (C) coefficient.

This section details the dynamic force coefficients of the bearing at various operating conditions of applied load and shaft speed. It includes the direct stiffness, direct damping and direct virtual-mass coefficients. The current bearing geometry is similar to the one tested by Jani [38], hence as with his test results, the current ones show negligibly small cross-coupling coefficients. Thus, for the brevity of the discussion this thesis does not include cross-coupling stiffnesses, damping and virtual-mass coefficients.

Figure 42 shows the experimental and predicted real part of the complex dynamic stiffness for the steel-pads bearing (left) and the copper-pads bearing (right) operating at a shaft speed of 48 m/s (9 krpm) and under a specific load of 0.35 MPa (top) and 1.38 MPa (bottom). The figure details the real part of the direct complex dynamic stiffness [Re(H_{xx}) and Re(H_{yy})] versus excitation frequency (ω). Considering the experimental results, the steel-pads bearing yields Re(H_{yy})> Re(H_{xx}) for operation at both low load (0.35 MPa) and high load (1.38 MPa). Since the bearing is loaded along the *y*-direction, this yields a high stiffness in the loaded direction and thus produces bearing stiffness orthotropy. Contrary to

the steel-pads bearing, the copper pad bearing Re(H_{xx}) is ~ 12% higher than Re(H_{yy}) at 0.35 MPa. However at a high load (1.38 MPa), Re(H_{yy})> Re (H_{xx}) by ~20%.

Comparison of the S-PB and C-PB experimental results show that for operation at 0.35 MPa, Re(H_{yy}) is identical for both bearings. However, along the orthogonal *x*-direction, the S-PB Re(H_{xx}) is ~ 40 % lesser than the C-PB Re(H_{xx}). For operation at the high load, difference between the copper-pads bearing and steel-pads bearing Re(H_{xx}) and Re(H_{yy}) increases. Along the *y*-direction, the steel-pads bearing Re(H_{yy}) is 14 % higher than the copper-pads bearing Re(H_{yy}) whereas along the *x*-direction the steel-pads bearing Re(H_{xx}) is ~ 43% less than the copper-pads bearing Re(H_{xx}). As discussed in the earlier section, the pads' temperatures of the C-PB are cooler than those of the S-PB. The cooler oil film results in a higher film viscosity which in turn results in a larger film stiffness.

For operation at 48 m/s (9 krpm) and 0.35 MPa, a comparison of the S-PB experimental and predicted results from XLTPJB® shows that the model under predicts Re(H_{yy}) by 28% while Re(H_{xx}) correlates well with the experimental data. Running the predictive code to analyze the copper-pads bearing shows that the *y*-intercept of the Re(H_{yy}) correlates well with the experimental data however, the slopes of the Re(H_{yy})and Re(H_{xx}) curve-fit do not compare well. A higher slope of the predicted data indicates a larger virtual mass coefficient. Moreover, the code under predicts the copper-pads bearing's Re(H_{xx}) by 28% in comparison to the experimental values. When increasing the load from 0.35 MPa to 1.38 MPa and keeping the operating speed constant at 48 m/s (9 krpm), excellent correlation of the steel-pad bearing Re(H_{xx}) and Re(H_{yy}) is observed. For the copper-pads bearing, as compared to the experimentally derived results, predictions of Re(H_{yy}) and Re(H_{xx}) are 23% and 15% higher, respectively.

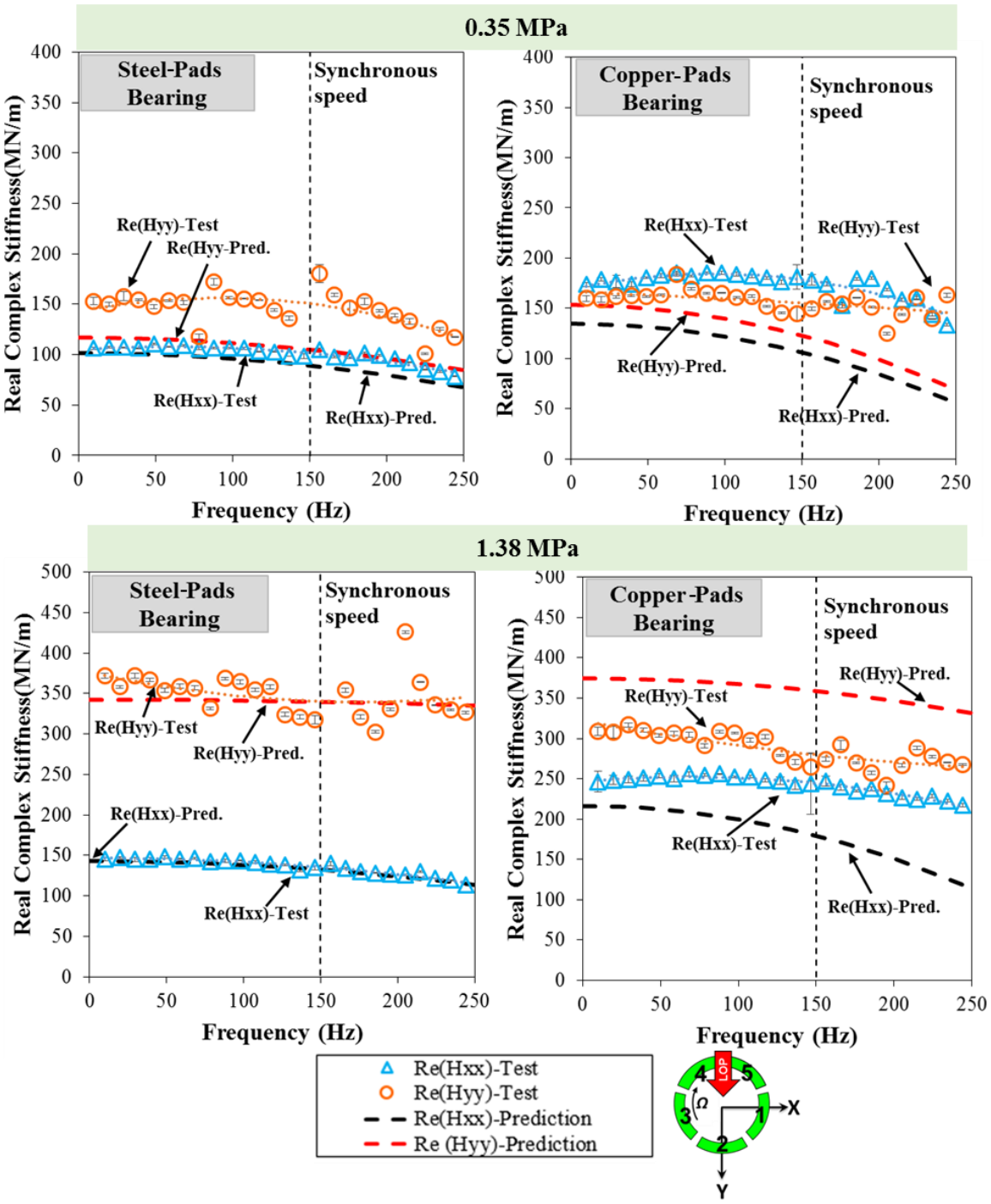

Figure 42 Predicted and experimental real part of complex direct dynamic stiffness [Re(H_{xx}) and Re(H_{yy})] for (left) steel-pads bearing and (right) copper-pads bearing vs. excitation frequency for operation at 0.35 MPa and 1.38 MPa specific load and 9 krpm (150 Hz) shaft speed.

Figure 43 presents the experimental and predicted imaginary part of the complex dynamic stiffnesses [Im(H_{xx}) and Im(H_{yy})] for the steel-pads bearing and the copper-pads

bearing; left and right graphs respectively. The operating conditions include shaft speed of 48 m/s (9 krpm) and specific load of 0.35 MPa and 1.38 MPa. In the graphs, Im(H_{yy}) presents the imaginary part of the complex stiffness along the direction of the load, i.e. *y*-axis, and Im(H_{xx}) represents the imaginary part of the complex stiffness along the orthogonal *x*-direction. Each plot in the figure presents Im(H_{xx}) and Im(H_{yy}) test points over the range of frequencies from 0- 250 Hz. The slope of the line curve fit over the test points yields the damping coefficient. For operation at both the 0.35 MPa and 1.38 MPa, both bearings show a very small difference in slope (~ 10 %). This indicates that regardless of the change in applied load, the damping coefficients do not change along the *x* and *y* directions.

Comparison of the experimental Im(H_{xx}) and Im(H_{yy}) for the steel-pads bearing and the copper-pads bearing indicate that at a low load (0.35 MPa) operation, both Im(H_{xx}) and Im(H_{yy}) for the C-PB are slightly higher than those for the S-PB i.e. Im(H_{xx}) is 40% higher and Im(H_{yy}) is 18 % higher. With an increase in load from 0.35 MPa to 1.38 MPa, Im(H_{xx}) for the C-PB is still higher than that for the S-PB (relatively ~ 38 % higher). However, Im(H_{yy}) for both bearings is nearly identical.

Comparison of the predicted and experimental results shows that for the steel-pads bearing operating at low load (0.35 MPa) and 48 m/s (9 krpm), the model under predicts both Im(H_{xx}) (slope ~ 10 % less) and Im(H_{yy}) (slope ~ 17% less). At the same operating condition, for the copper-pads bearing the predicted results show that the slope of Im(H_{xx}) is 22% less than the measured magnitudes. And that of Im(H_{yy}) is 7% less than the measured values. Keeping the operating speed constant and increasing the load to 1.38 MPa produces a good correlation of the steel-pads bearing Im(H_{xx}), however the tool over predicts Im(H_{yy}) as its slope is 21% higher than the slope of the test derived Im(H_{yy}). For the copper-pads bearing, with an increase in load, the computational model over predicts both Im(H_{xx}) and Im(H_{yy}).

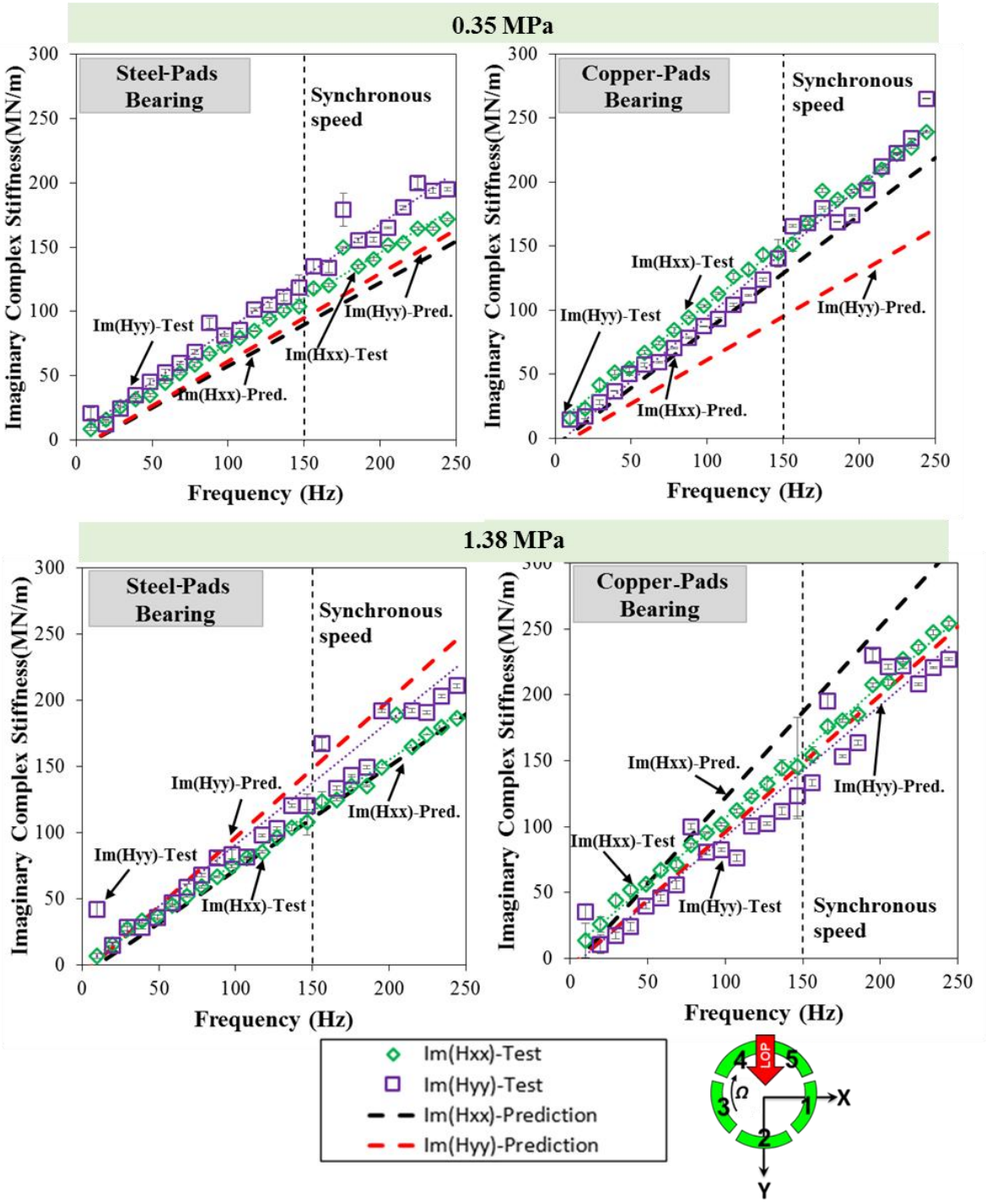

Figure 43 Predicted and experimental imaginary part of complex dynamic stiffnesses [*Im(H_{xx})* and *Im(H_{yy})*] for (left) steel-pads bearing and (right) copper-pads bearing vs. excitation frequency for operation under 0.35 MPa and 1.38 MPa specific load and 9 krpm (150 Hz) shaft speed.

7.1 Dimensionless Direct Stiffness Coefficients

A dimensionless direct stiffness coefficients is

$$k = \frac{K\, C_b}{W} \tag{20}$$

where K is the direct stiffness coefficient, C_b is the nominal radial bearing clearance, and W is the static load applied on the bearing.

Figure 48 shows the dimensionless stiffness k_{yy} for both the steel-pads bearing and the copper-pads bearing along the y (load)-direction. The operating conditions for the test data presented include three shaft speeds from 48 m/s (9 krpm) to 74 m/s (14 krpm), and specific loads ranging from 0.7 MPa to 2.0 MPa.

The figure shows that for the steel-pads bearing, keeping the load constant and changing the speed results in a very small change in direct stiffness k_{yy}. The maximum increases in stiffness is ~ 10 % with an increase in shaft speed from 48 m/s to 74 m/s at 0.7 MPa of specific load. In contrast that the copper-pads bearing shows a significant increase in stiffness with an increase in speed at a constant load. For example at 1.03 MPa, k_{yy} increases from 3.6 to 5.1 (42% increment) with an increase in shaft speed from 48 m/s to 74 m/s. However, k_{yy} decreases with an increase in specific load at constant speed. For example, at 64 m/s with an increase in specific load from 0.7 MPa to 2.1 MPa, k_{yy} decreases by ~ 40%.

Since both bearings have the same radial bearing clearance, comparison of the absolute stiffness coefficients can be directly made from the dimensionless stiffness (k_{yy}) vs. load. Figure 48 shows that for operation at low loads (< 1.7 MPa) and high shaft speeds (> 48 m/s) the copper-pads bearing stiffness is higher than that of the steel-pads bearing. For example at 0.7 MPa and 64 m/s, the C-PB stiffness is ~ 13 % higher than the S-PB stiffness. Similarly, at 0.7 MPa and 74 m/s, the C-PB stiffness is ~ 32 % higher than that of the S-PB. Further, for operation at 64 m/s shaft speed and a high load of 1.38 MPa, k_{yy} for both C-PB and S-PB is 4.0.

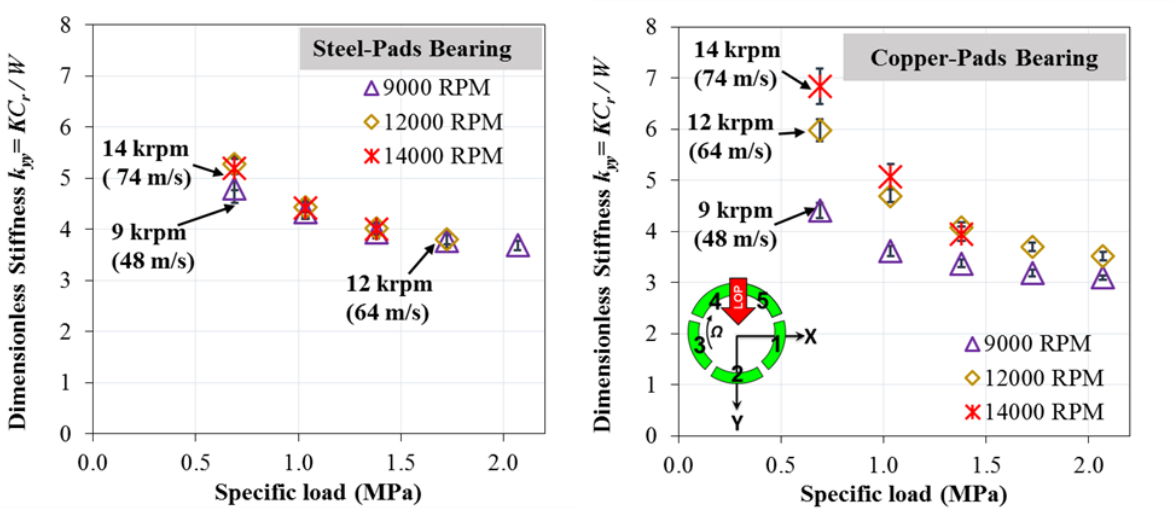

Figure 44 Test derived stiffness (k_{yy}) coefficient for (left) steel-pads bearing and (right) copper-pads bearing vs. specific load (0.35 to 2.1 MPa) for operation at three shaft surface speed (48-74 m/s).

Figure 45 compares the static load derived k_{stat} and the dynamic load derived k_{yy} for the steel-pads bearing at various shaft speeds (9 to 14 krpm) and specific loads (0.3 to 2.1 MPa). k_{stat} is defined as

$$k_{stat} = \frac{K_{STAT}\, C_b}{W} \tag{21}$$

where K_{STAT} is the static stiffness of a bearing derived from slope of the load vs. shaft eccentricity data, see Figure 20

Figure 45 shows that, at any operating shaft speed, both k_{stat} and k_{yy} decrease with an increase in specific load. For example at 12 krpm, k_{stat} decrease from 4.1 to 2.3 with an increase in specific load from 0.7 MPa to 2.0 MPa.

A comparison of k_{stat} and k_{yy} shows that for any operating point k_{stat} is smaller than k_{yy}. For example, for operation at 12 krpm (64 m/s) shaft speed and at a specific 0.7 MPa, k_{stat} is 4.1 where as k_{yy} is 5.2. This difference shows that k_{yy} is consistently 27 % higher than k_{stat}.

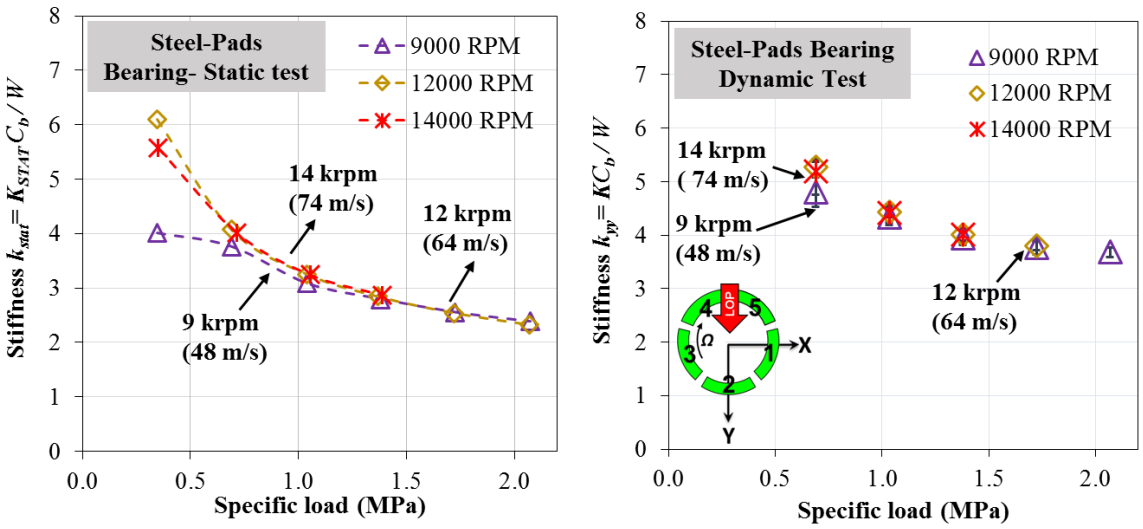

Figure 45 Test derived stiffnesses (left) k_{stat} and (right) k_{yy} for steel-pads bearing vs. specific load (0.31 to 2.1 MPa) for operation at three shaft surface speed (48-74 m/s).

Figure 46 presents the test derived k_{stat} and k_{yy} for the copper-pads bearing for operation at various shaft speeds (9 to 14 krpm) and specific loads (0.5 to 2.1 MPa). Similar to the results discussed for S-PB in the prior section, the C-PB k_{stat} and k_{yy} follow the same trend, i.e at any shaft speed, both k_{stat} and k_{yy} decreases with an increase in specific load.

The test data shows that k_{yy} is larger than the k_{stat}. For operation at a low load (0.7 MPa) and low speed 48 m/s (9 krpm), k_{yy} is ~ 5 % larger than k_{stat} whereas at at a high load (1.38 MPa) and high speed 74 m/s (14 krpm), k_{yy} is ~ 55 % larger than k_{stat}.

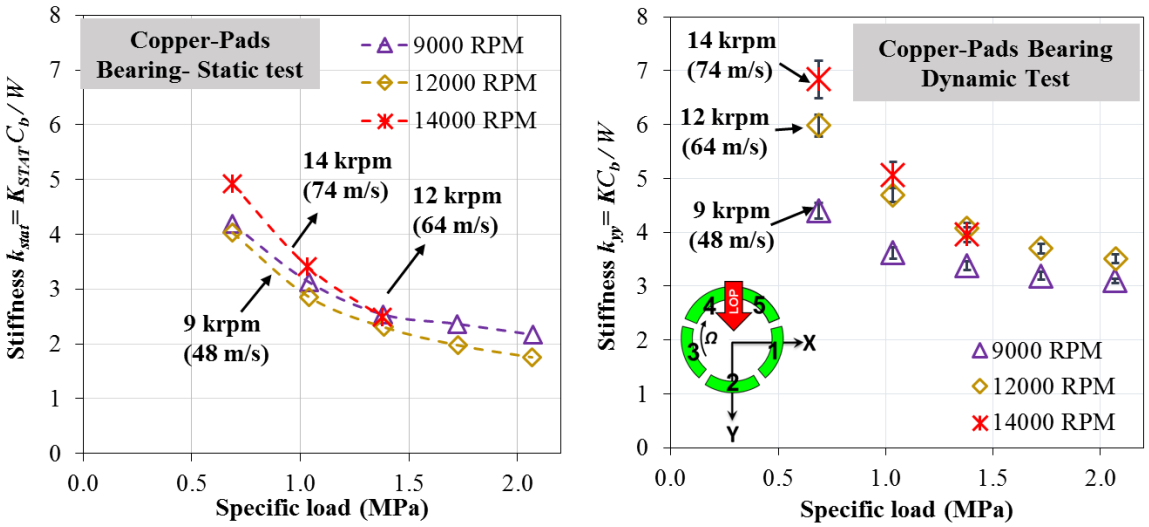

Figure 46 Test derived stiffnesses (left) k_{stat} and (right) k_{yy} for copper-pads bearing vs. specific load (0.31 to 2.1 MPa) for operation at three shaft surface speed (48-74 m/s).

Figure 46 presents the ratio K_{STAT} / K_{YY} for the S-PB and the C-PB for operation at various shaft speeds (9 to 14 krpm) and specific loads (0.5 to 2.1 MPa). For both the bearings, the ratio decreases with an increase in applied load.

For S-PB, the ratio is independent of shaft speed and ranges from 0.65 to 0.75 i.e. K_{STAT} is ~ 25-35 % smaller than K_{YY}. The ratio decreases with both operating speed and load for C-PB. The C-PB ratio ranges from 0.7 to 0.85 i.e K_{STAT} is ~ 15-30 % smaller than K_{YY}.

Carter [40] tested a 5-pad rocker pivot bearing under load-on configuration. Similar to the present results, Carter's test results show $K_{STAT} < K_{YY}$ and that the ratio of K_{STAT} / K_{YY} decreases with an increase in load. The ratio ranges from 0.65 to 0.90 over the range of operating conditions. Moreover, Jani [38] tested the same S-PB under a Load-Between-Pad configuration; his test results show that $K_{STAT} < K_{YY}$ i.e. the K_{STAT} / K_{YY} ratio ranges from 0.52 to 0.73.

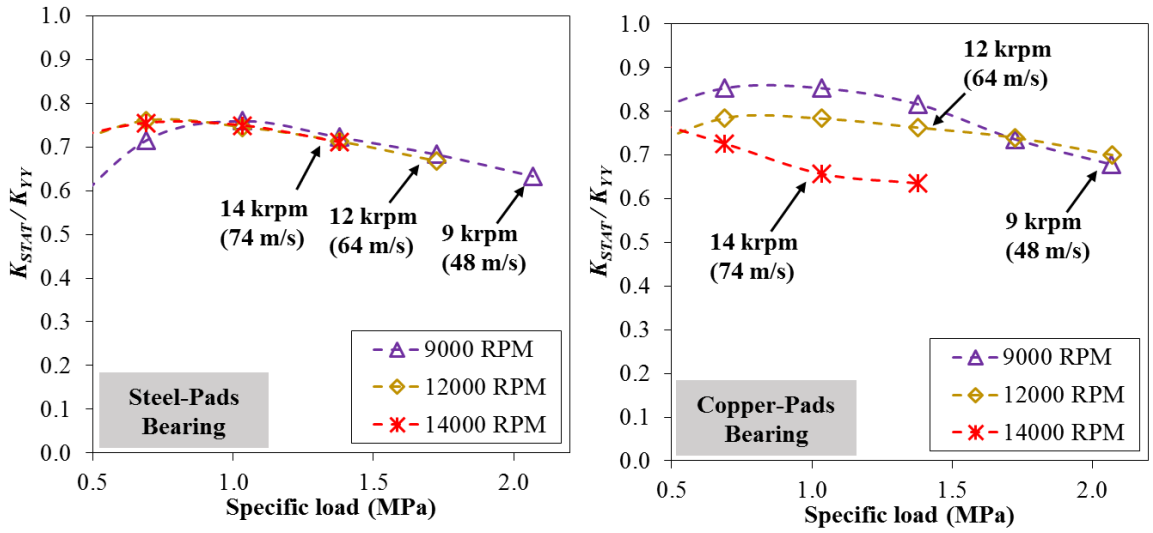

Figure 47 Ratio K_{STAT} / K_{YY} for (left) steel-pads bearing and (right) copper-pads bearing vs. specific load (0.35 to 2.1 MPa) for operation at three shaft surface speeds (48-74 m/s).

Figure 44 shows the test direct stiffness coefficients (k_{xx}) along the *x*-direction for both bearings. The operating conditions for the test data presented include three shaft speeds from 48 m/s (9 krpm) to 74 m/s (14 krpm) and specific loads ranging from 0.7 MPa to 2.0 MPa.

For the steel-pads bearing, at any given specific load, k_{xx} increases with an increase in shaft speed. For example at 0.7 MPa, increasing the shaft speed from 48 m/s (9 krpm) to 74 m/s (14 krpm) increases the stiffness coefficient by 38 %. However, at a higher load of 1.38 MPa, the percentage increase in stiffness reduces to 30 %. Thus, an increase in shaft speed results in an increase in oil-film stiffness. At a constant speed, the figure shows that k_{xx} of the steel-pads bearing decreases with an increase in load. However, since the dimensionless stiffness is a function of *W*, the physical stiffness coefficient does not decrease. For example, at 9 krpm, doubling the load from 0.69 MPa to 1.38 MPa lowers the value of k_{xx} from 2.6 to 1.6 (38 % decreases). However, multiplying k_{xx} by 2 (double load) to eliminate the effect of *W* yields k_{xx} = 3.2. Thus, in actuality the physical stiffness (K_{XX}) coefficient increases by 23 %.

The copper-pads bearing (C-PB) show similar trends as those of the steel-pads bearing (S-PB). At a constant speed the stiffness increases with an increase in load. For

examples at 48 m/s (9krpm), k_{xx} decreases by ~ 32 % as the applied load increases from 0.7 MPa to 1.38 MPa results. In contrast to that, keeping the load constant at 0.7 MPa and increasing the shaft speed from 48 m/s (9 krpm) to 74 m/s (9 krpm) results in 52 % increase in stiffness coefficient.

Comparison of the S-PB and the C-PB results show that at each operating point the stiffness coefficient of the C-PB is higher than that of the S-PB. For operation at a low load (0.7 MPa) and low speed 48 m/s (9 krpm), the stiffness of C-PB is 70 % higher than that of the S-PB. Similarly, at a high load (1.38 MPa) and high speed 74 m/s (14 krpm), the stiffness is 75 % higher.

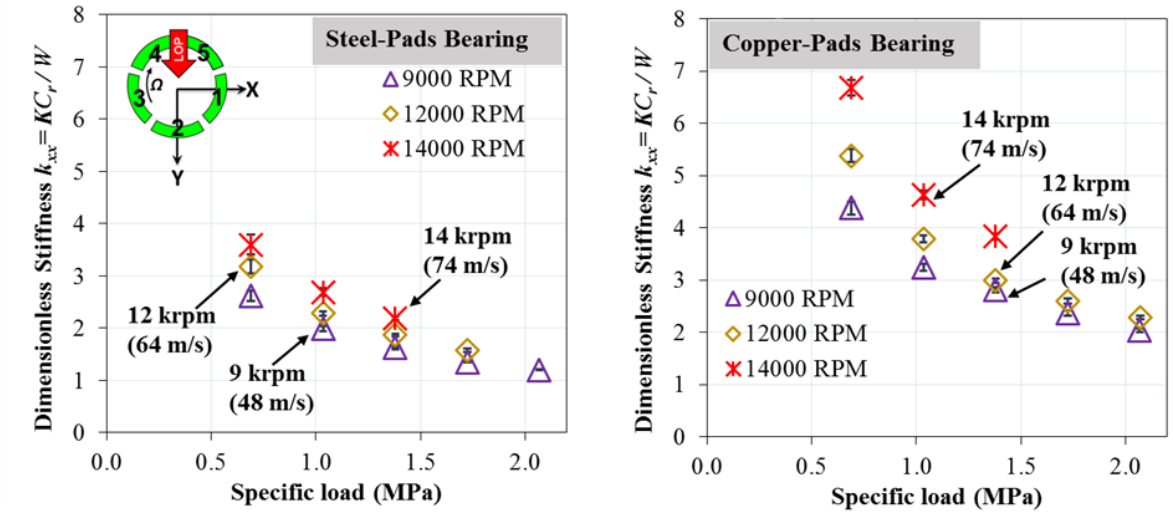

Figure 48 Experimental stiffness coefficient (k_{xx}) for (left) steel-pads bearing and (right) copper-pads bearing vs. specific load (0.35 to 2.1 MPa) for operation at three shaft surface speed (48-74 m/s).

Figure 49 shows k_{yy} vs. k_{xx} for the steel-pads bearing and the copper pads-bearing. The operating conditions include three shaft speeds at 48 m/s, 64 m/s, and 74 m/s, and a specific loadranging from 0.7 MPa to 2.1 MPa. The figure basically illustrates the orthotropy of the bearing stiffnesses ($k_{yy} > k_{xx}$). The test results for the S-PB shows a high stiffness orthotropy i.e $k_{yy} > k_{xx}$ for all test points. For operation at a low load specific (0.35 MPa) and high speed (74 m/s) k_{yy}/k_{xx} = 1.4 whereas for operation at a high specific load (2.1 MPa) and low speed (48 m/s) k_{yy}/k_{xx} = 2.8. This increase in (k_{yy}/k_{xx}) dictates 100 % increases in bearing stiffness orthotropy. One of the reason for the stiffness orthotropy is the result of uni-directional

loading (LOP configuration) of the bearings in y-direction. As compared to the orthogonal *x*- direction, the LOP configuration develops a smaller film thickness between a pad and the rotating shaft along the load direction. A smaller film thickness yields a higher stiffness along that direction. Also, changes in the *hot* clearance for both bearings effect the stiffnesses along the *x* and *y* directions.

Contrary to the S-PB stiffness test results, the C-PB shows a lesser bearing orthotropy. The C-PB shows a zero orthotropy k_{yy}/k_{xx} = 1.0 for operation at a high shaft speed (74 m/s) and low specific load (0.35 MPa). However, for operation at a high load (2.1 MPa) and low shaft speed (48 m/s), k_{yy}/k_{xx} increases to 1.6. Comparing the S-PB and the C-PB results show that over the range of test points, the S-PB is 40%-75% more orthotropic than the C-PB. Since the *hot* clearance of the C-BP is smaller than that of the S-PB, the lower orthotropy of the C-PB is likely due to the lower hot clearance of the bearing along the *x* direction.

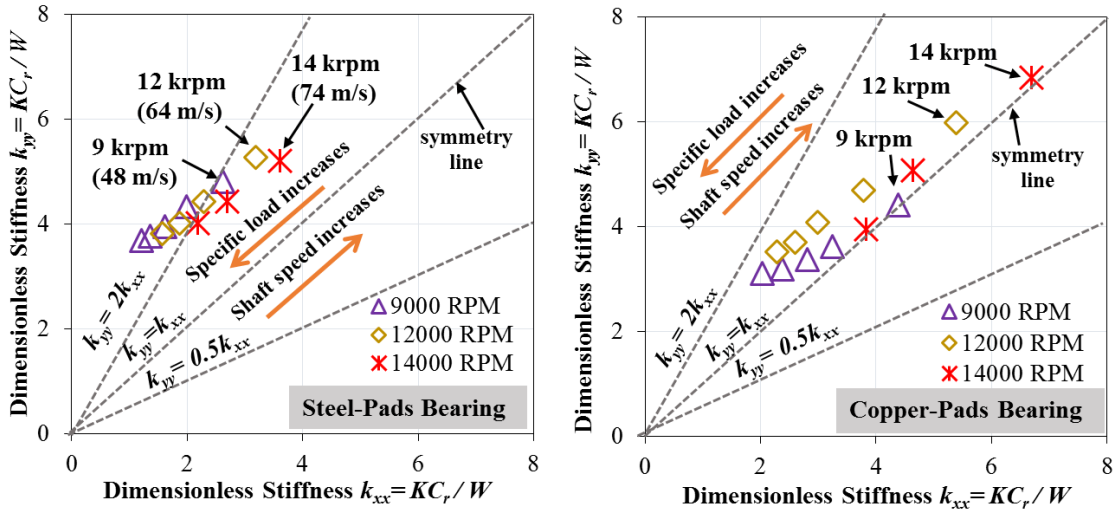

Figure 49 Experimental stiffness coefficients k_{yy} *vs.* k_{xx} for (left) steel-pads bearing and (right) copper-pads bearing as a function of increasing specific load (0.35 to 2.1 MPa) and shaft surface speed (48 to 74 m/s).

Figure 50 presents the predicted and measured k_{xx} and k_{yy} for the steel-pads bearing and the copper-pads bearing. The operating conditions include specific loads ranging from 0.35 MPa to 2.1 MPa, and shaft speeds ranging from 48 m/s (9 krpm) to 74 m/s (14 krpm).

The S-PB shows a high orthotropy, in particular at low $S < 2$. At $S = 0.9$ the experimental k_{yy}/ k_{xx} is 2.5 and the predicted k_{yy}/ k_{xx} is ~ 2.4. Thus, indicating a high

orthotropy and a good correlation of the predicted and experimental results. At a high Sommerfeld number, orthotropy tends to decrease. For example at S = 4, the experimental k_{yy}/k_{xx} is 1.3, whereas the predicted k_{yy}/k_{xx} is 1.1. The reason is that at a high Sommerfeld number (high speed and low load), the shaft eccentricity is low and the fluid film thickness is large which results in nearly a symmetric bearing clearance along the x and y directions. Thus, resulting in an identical stiffnesses along the x and y directions.

For the S-PB, a comparison of the predictions shows good correlation with the measured results. A quantitative analysis of the results show that for S< 2 both predicted k_{xx} and k_{yy} are within 20% of the experimental results. The difference increases with an increase in S and reaches to about 35 % maximum for k_{yy} at S = 3.5. Both k_{xx} and k_{yy} show a lowest difference of ~ 2% at S = 0.8.

For the C-PB, k_{xx} and k_{yy} from test data and prediction increases with an increase in Sommerfeld Number (S). Also both test data show stiffness orthotropy for S >2 (high speed and low load operation). The orthotropy decreases with an increase in S. At S= ~ 2.5, the experimental k_{yy}/k_{xx} is 1.1 whereas the predicted k_{yy}/k_{xx} ~ 1.4.

An overall comparison shows that the computational model accurately predicts C-PB k_{yy} within 20% and C-PB k_{xx} within 40% of the experimental results for 90 % of the test points. At some test points the computational model is accurate to within 10 %. For example at S=1, the predicted and the experimental k_{xx} differ by ~ 10%. Moreover, compared to predictions, the experimental results do not show a significant increase in bearing orthotropy. For example at S=0.7, the experimental k_{yy}/k_{xx} =1.5 and the predicted k_{yy}/k_{xx} = ~ 2.0.

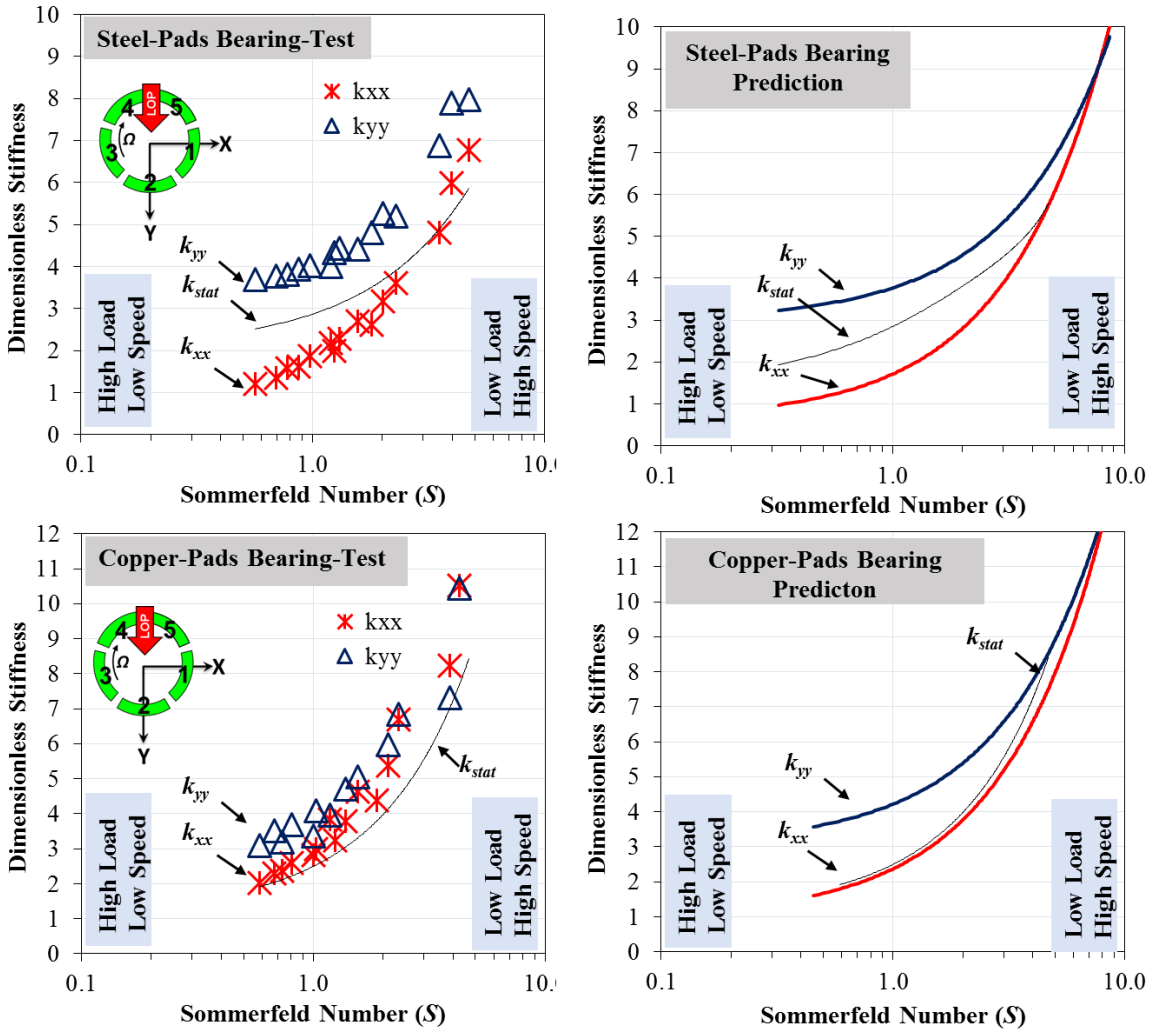

Figure 50 Experimental and predicted stiffness coefficients (k_{xx}, k_{yy}) for (top) steel-pads bearing and (bottom) copper-pads bearing for operation at various shaft surface speeds (48-74 m/s) and specific loads (0.35-2.1 MPa).

7.2 Dimensionless Direct Damping Coefficients

The bearing damping coefficients are non-dimensionalized as

$$c = \frac{C\ C_b\ \Omega}{W} \tag{22}$$

where C is the direct damping coefficient and Ω is shaft speed (in rad/s).

Figure 51 shows the direct damping (c_{yy}) for the steel-pads bearing and the copper-pads bearing along the load (y-axis) direction. The operating conditions for the test results include

three shaft speeds ranging from 48 m/s (9 krpm) to 74 m/s (14 krpm), and specific loads ranging from 0.35 MPa to 2.1 MPa. For both the C-PB and the S-PB with an increase in speed, at a constant load, c_{yy} increases. And with an increase in load, at a constant shaft speed, c_{yy} decreases. For the S-PB, at 0.35 MPa c_{yy} increases by ~ 64 % with an increase in shaft speed form 48 m/s (9 krpm) to 74 m/s (14 krpm). Further, keeping the shaft speed constant at 48 m/s, the S-PB's c_{yy} decreases from 5.4 to 0.9 (6 times reduction) with an increase in load from 0.35 MPa to 2.1 MPa.

A comparison of c_{yy} of the S-PB and C-PB shows that the damping coefficients of the copper-pads bearing is higher than that of the steel-pads bearing at all the operating conditions. At low load (0.35 MPa) and low shaft speed (48 m/s) C-PB offers 18 % a higher damping than the S-PB. Similarly at high load (1.7 MPa) and high shaft speed (64 m/s), C-PB c_{yy} is ~ 20 % higher than that of S-PB.

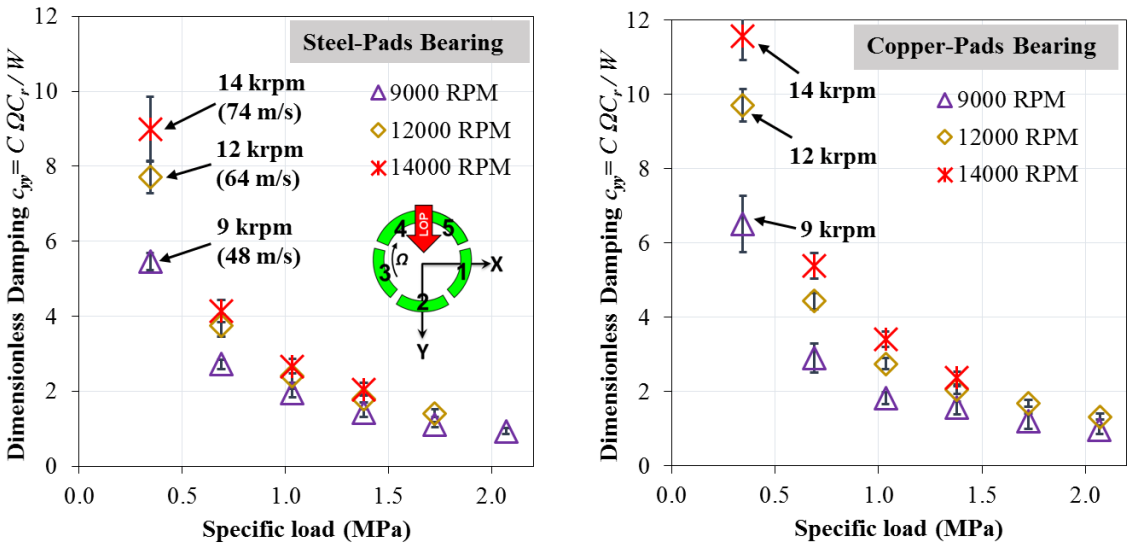

Figure 51 Experimental damping coefficient (c_{yy}) for (left) steel-pads bearing and (right) copper-pads bearing vs. specific load (0.35 to 2.1 MPa) for operation at three shaft surface speeds (48-74 m/s).

Figure 52 shows the direct damping coefficients (c_{xx}) along the *x*-direction for the steel-pads bearing (left) and the copper-pads bearing (right). The operating conditions include three shaft speeds from 48 m/s (9 krpm) to 74 m/s (14 krpm), and specific loads ranging from 0.7 MPa to 2.0 MPa.

The figure shows that for the S-PB, at any applied load, c_{xx} increases with an increase in shaft speed. For example, at 0.35 MPa, c_{xx} increases from 4.8 to 8.0 (67% increases) with an increase in speed from 48 m/s (9 krpm) to 74 m/s (14 krpm). Further, at any constant speed c_{xx} decreases with an increase in a specific load. For example at 48 m/s (9 krpm) c_{xx} decreases from 4.8 to 0.8 (6 times) with an increase in specific load from 0.35 MPa to 2.1 MPa.

The damping coefficients for the copper-pads bearing follows a similar trend as those for the steel-pads bearing. At a constant load c_{xx} increases with an increase in speed. At 0.35 MPa c_{xx} increases from 6.8 to 11.1 (63 % increase). Moreover, at a constant shaft speed c_{xx} decreases with an increase in load. For example at 12 krpm (64 m/s) c_{xx} decreases from 9.2 to 1.4 (~ 6.5 times) with an increase in load from 0.35 MPa to 2.1 MPa.

Since the both the C-PB and S-PB have the same nominal bearing clearance, operate at the same shaft speed, and under the same specific load, a comparison between the actual damping (C_{XX}) can be directly extracted from the results shown. The C-PB offers a higher damping than the S-PB. For operation at a high speed (74 m/s) and low specific load (0.35 MPa), the C-PB C_{XX} is ~ 39% higher than that of the S-PB. Further, for operation at a low speed of 48 m/s (9 krpm) and high specific load of 2.1 MPa the C-PB damping is ~ 32 % higher than that of the S-PB.

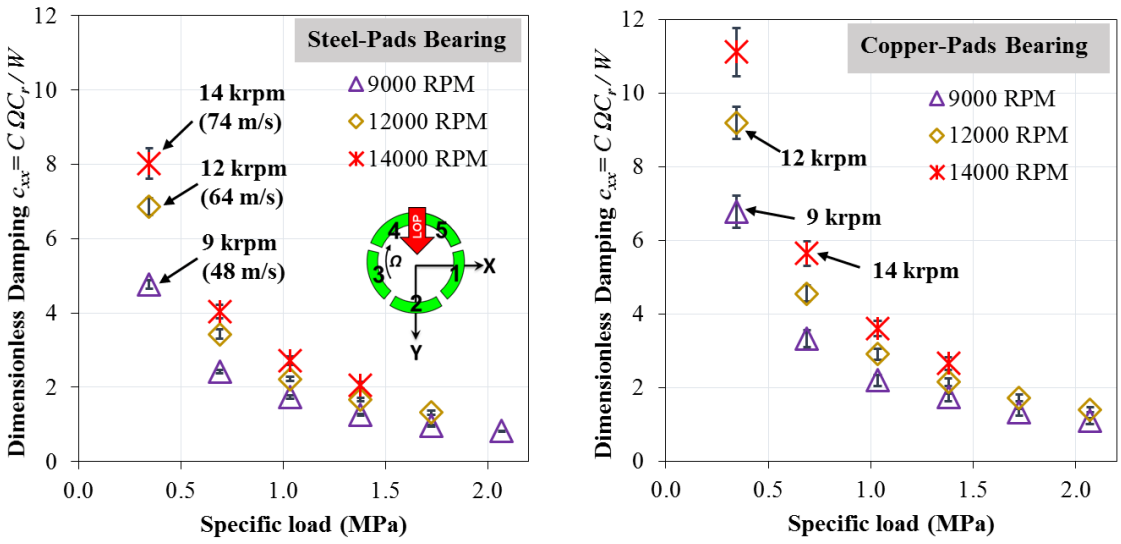

Figure 52 Experimental damping coefficient (c_{xx}) for (left) steel-pads bearing and (right) copper-pads bearing vs. specific load (0.35 to 2.1 MPa) for operation at three shaft surface speed (48-74 m/s).

Figure 53 shows c_{yy} vs. c_{xx} for the steel-pads bearing (S-PB) and the copper-pads bearing (C-PB). The operating conditions include three shaft speeds 48 m/s (9krpm), 64 m/s (12 krpm) and 74 m/s (14 krpm) and six specific loads ranging from 0.35 MPa to 2.1 MPa. The line of symmetry in the figure indicates the $c_{yy} = c_{xx}$ point. Thus, for any point above the line of symmetry $c_{yy} > c_{xx}$, and for any point below the line symmetry $c_{yy} < c_{xx}$.

The test results for the S-PB shows negligible damping orthotropy i.e ($c_{yy} \approx c_{xx}$). For example at a low load (0.35 MPa) and high shaft speed of 14 krpm (74 m/s), $c_{yy}/c_{xx} = 1.12$ (12 % higher). Similarly, at 2.1 MPa (high load) and 9 krpm (low speed) $c_{yy}/c_{xx} = 1.15$ (15 % higher). Also, over the range of test points, the difference between c_{yy} and c_{xx} is ~ < 20 %.

The C-PB results show identical trends in damping coefficients as those noted for the S-PB. The c_{yy} and c_{xx} are nearly identical with a difference of ~ less than 10%. For example, for operation at a low load (0.35 MPa) and high speed (14 krpm), $c_{yy}/c_{xx} = 1.0$. Similarly, at a high load (2.1 MPa) and low speed (9 krpm) operation, $c_{yy}/c_{xx} = 0.9$.

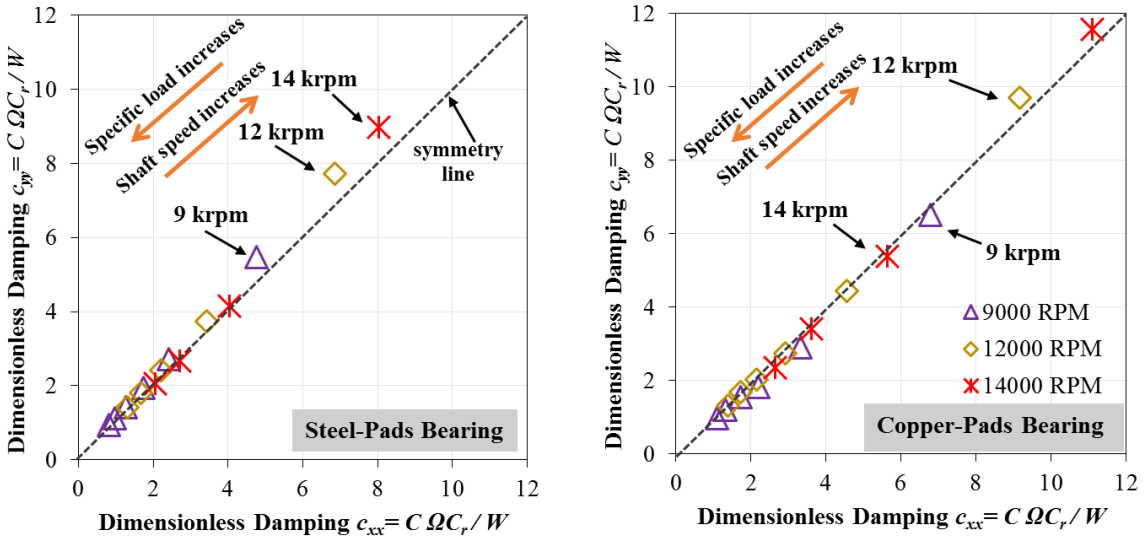

Figure 53 Experimental damping coefficients c_{xx} vs. c_{yy} for (left) steel-pads bearing and (right) copper-pads bearing as a function of increasing specific load (0.35 to 2.1 MPa) and shaft surface speed (48 to 74 m/s).

Figure 54 shows the experimental and predicted c_{xx} and c_{yy} for the steel-pads bearing and the copper-pads bearing. The operating conditions for the measurements include three shaft speeds ranging from 48 m/s (9 krpm) to 74 m/s (14 krpm), and specific loads ranging from 0.35 MPa to 2.1 MPa. Both measured and predicted steel-pads bearing damping coefficients increase with an increase in S. Further, the damping coefficients are symmetric along the orthogonal x and y directions ($c_{xx} \approx c_{yy}$).

The S-PB damping coefficients (c_{xx} and c_{yy}) increase from 0.9 to 9.0 with an increase in S from 0.5 to 4.7. The predictive code correlates well with the measured results as the predicted values are within ~20 % of the measured data for $S < 2$. For $S > 2$ the code underestimates both c_{xx} and c_{yy} by 20- 40 %

A comparison of the experimental and predicted damping coefficient (c_{yy} and c_{xx}) for the C-PB shows that both measured and predicted damping coefficients are symmetric ($c_{yy} \sim c_{xx}$) over the entire range of Sommerfeld Number. Also, both c_{yy} and c_{xx} increases with an increase in S.

For C-PB c_{xx}, the predictive results correlates well with the test data for $S < 2$ (percentage difference < 20 %) and under predicts for $S > 2$. However, for C-PB c_{yy} the predictive model

results correlate well for 0.8< S < 2 (percentage difference < 25%) and under predict for S >2.

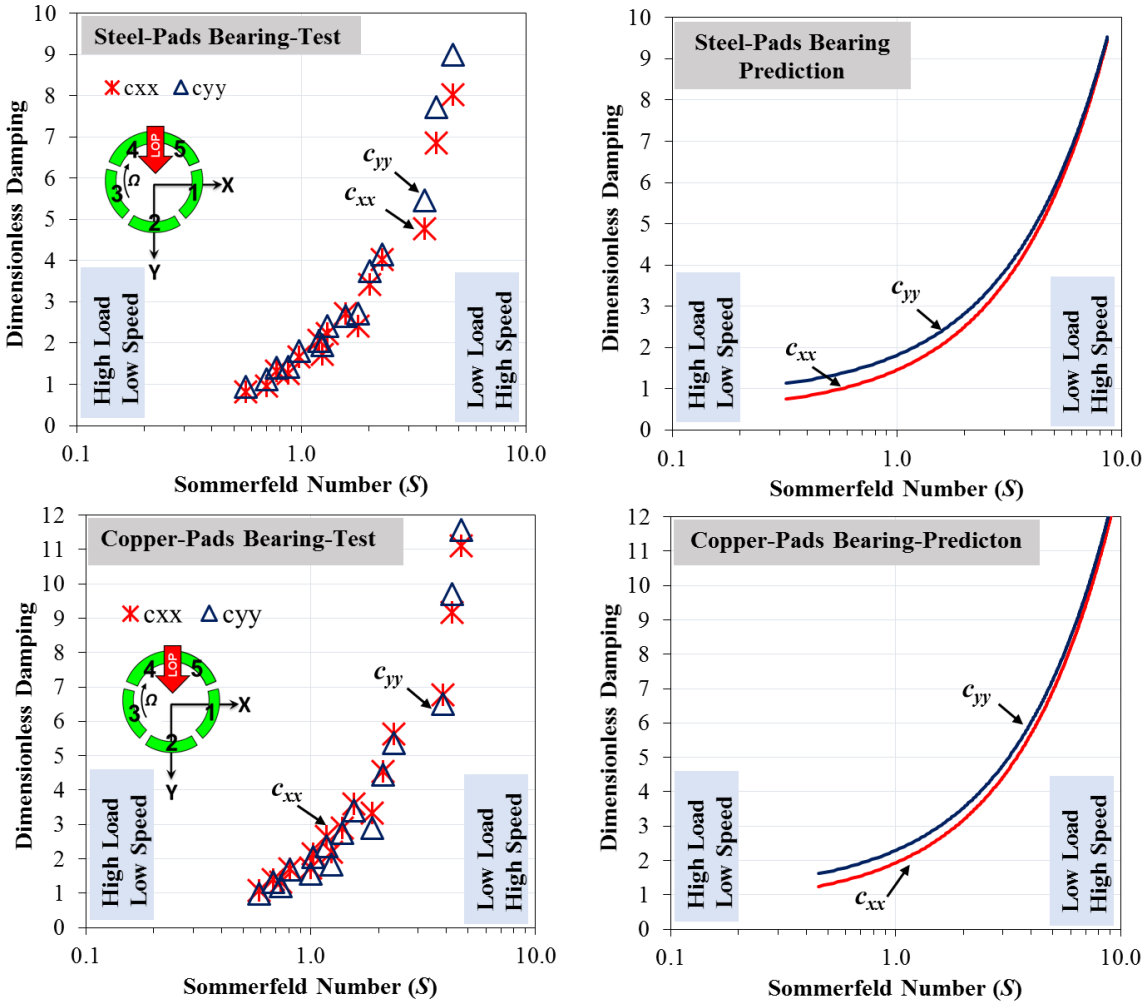

Figure 54 Experimental and predicted damping coefficients (c_{xx}, c_{yy}) for (top) steel-pads bearing and (bottom) copper-pads bearing for operation at various shaft surface speeds (48-74 m/s) and specific loads (0.35-2.1 MPa).

7.3 Virtual Mass Coefficients

The virtual mass coefficient is non-dimensionalized as

$$m = \frac{M\, C_b\, \Omega^2}{W} \tag{23}$$

where M is the direct virtual mass coefficient.

Figure 55 shows the virtual mass coefficient m_{yy} for the steel-pads bearing (S-PB) and for the copper-pads bearing (C-PB) along the loaded (y-axis) direction. The figure presents results at three operating speeds 48 m/s (9 krpm), 64 m/s (12 krpm) and 74 m/s (14 krpm) and six specific load points ranging from 0.35 MPa to 2.1 MPa. For both bearings mass coefficients, the uncertainties in the values are very high i.e. ranging from 20 % to 200%. Thus, a reasonable comparison of the C-PB and the S-PB m_{yy} cannot be made. Also, for both bearings the correlation factor for Re (H_{yy}) is low. For operations at load < 1.38 MPa and shaft speed > 48 m/s (9 krpm) the correlation factor between the KCM model and experimental results vary from 0.2 to 0.5. The low correlation factor for the specified operation shows that the identified m_{yy} are not accurate i.e. the assumed physical model K-$M\omega^2$ is not adequate.

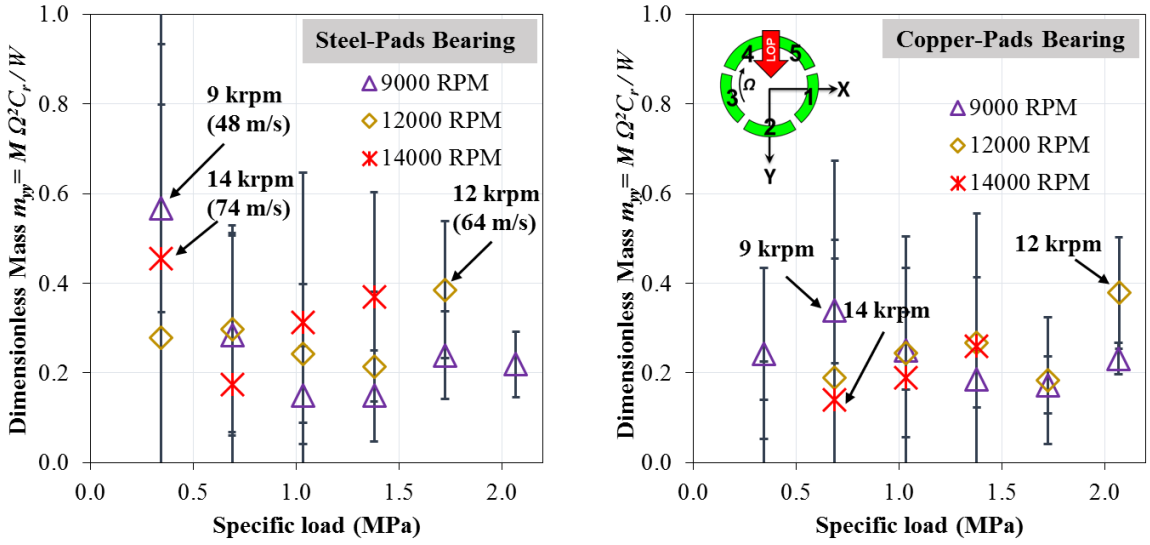

Figure 55 Experimental virtual mass coefficient (m_{yy}) for (left) steel-pads bearing and (right) copper-pads bearing vs. specific load (0.35 to 2.1 MPa) for operation at three shaft surface speed (48-74 m/s).

Figure 56 shows the direct virtual mass coefficient m_{xx} for the steel-pads bearing (S-PB) and for the copper-pads bearing (C-PB) and along the x-direction. The operating conditions include specific loads ranging from 0.35 MPa to 2.1 MPa, and three shaft speeds 48 m/s (9 krpm), 64 m/s (12 krpm) and 74 m/s (14 krpm). For the S-PB, m_{xx} decreases with an increases in shaft speed at a low load operation (< 1.0 MPa). For example at 0.35 MPa m_{xx} decreases from 0.42 to 0.35 (16 % decrease) with an increase in speed from 48 m/s to 74

m/s. For the copper-pads bearing m_{xx} increases with an increase in speed at any specific load. For example at 1.03 MPa, an increase in speed from 48 m/s to 74 m/s results in 25 % increment of m_{xx}.

Both bearings yield high experimental uncertainty in mass coefficients. The uncertainties ranges from 10% to 90 %. Moreover, for operation at specific loads < 1.0 MPa, the correlation factor (r^2) of the KCM model and Re (H_{xx}) ranges from 0.5 to 0.7. The low correlation factor indicates a weak fit of the model on the experimental data. Hence, for operation at specific load < 1.0 MPa, the derived m_{xx} are not accurate.

Further comparison shows that at load < 1.03 MPa, the copper-pads bearing yields a higher virtual mass as compared to the steel-pads bearing. For example, at 0.7 MPa and 74 m/s (14 krpm) C-PB m_{xx} is 0.5 as compared to 0.17 of S-PB (3 times larger). Similarly, for operation at a high load of 1.7 MPa and 64 m/s (12 krpm), the difference between the copper-pads bearing and the steel-pads bearing m_{xx} is ~ 6%.

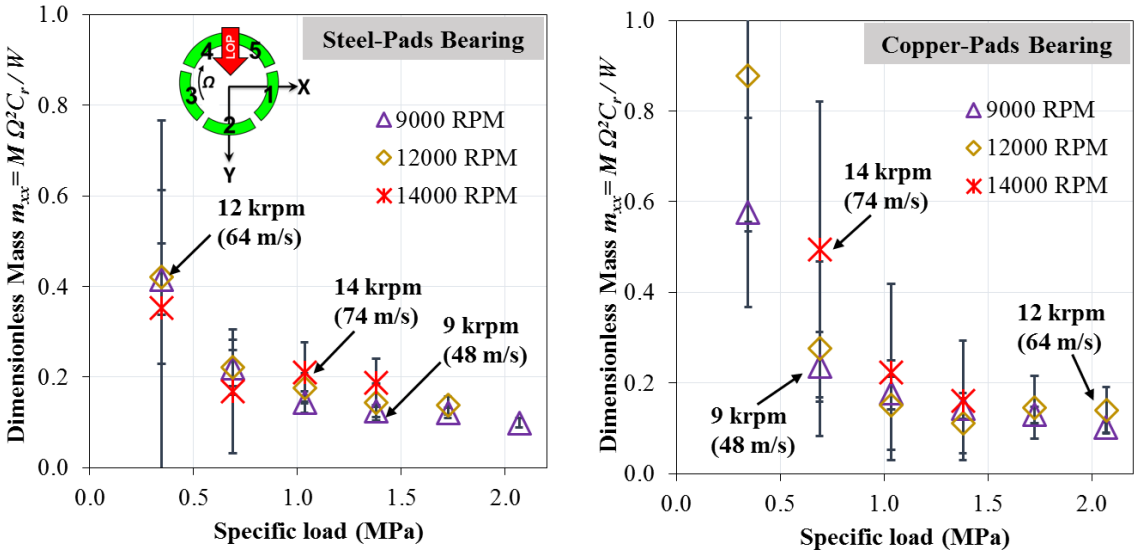

Figure 56 Experimental virtual mass coefficient (m_{xx}) for (left) steel-pads bearing and (right) copper-pads bearing vs. specific load (0.35 to 2.1 MPa) for operation at three shaft surface speed (48-74 m/s).

Figure 57 compares the experimental and predicted m_{xx},and m_{yy} for the steel-pads bearing and the copper-pads bearing as a function of Sommerfeld Number (S). The operating conditions include three shaft speeds ranging from 48 m/s (9 krpm) to 74 m/s (14 krpm) and

six specific loads ranging from 0.35 MPa to 2.1 MPa. The experimental virtual mass coefficients (m_{xx}, m_{yy}) of both bearings are small (~ <1.0). However the experimental uncertainties are very large for both bearings, particularly at high S. For S-PB at $S > 2.0$ the code over estimates m_{xx}. Similarly for $S < 0.8$ and $S > 3.5$ the code overestimates m_{yy}. Also for the C-PB the code over predicts both the m_{xx} and m_{yy}.

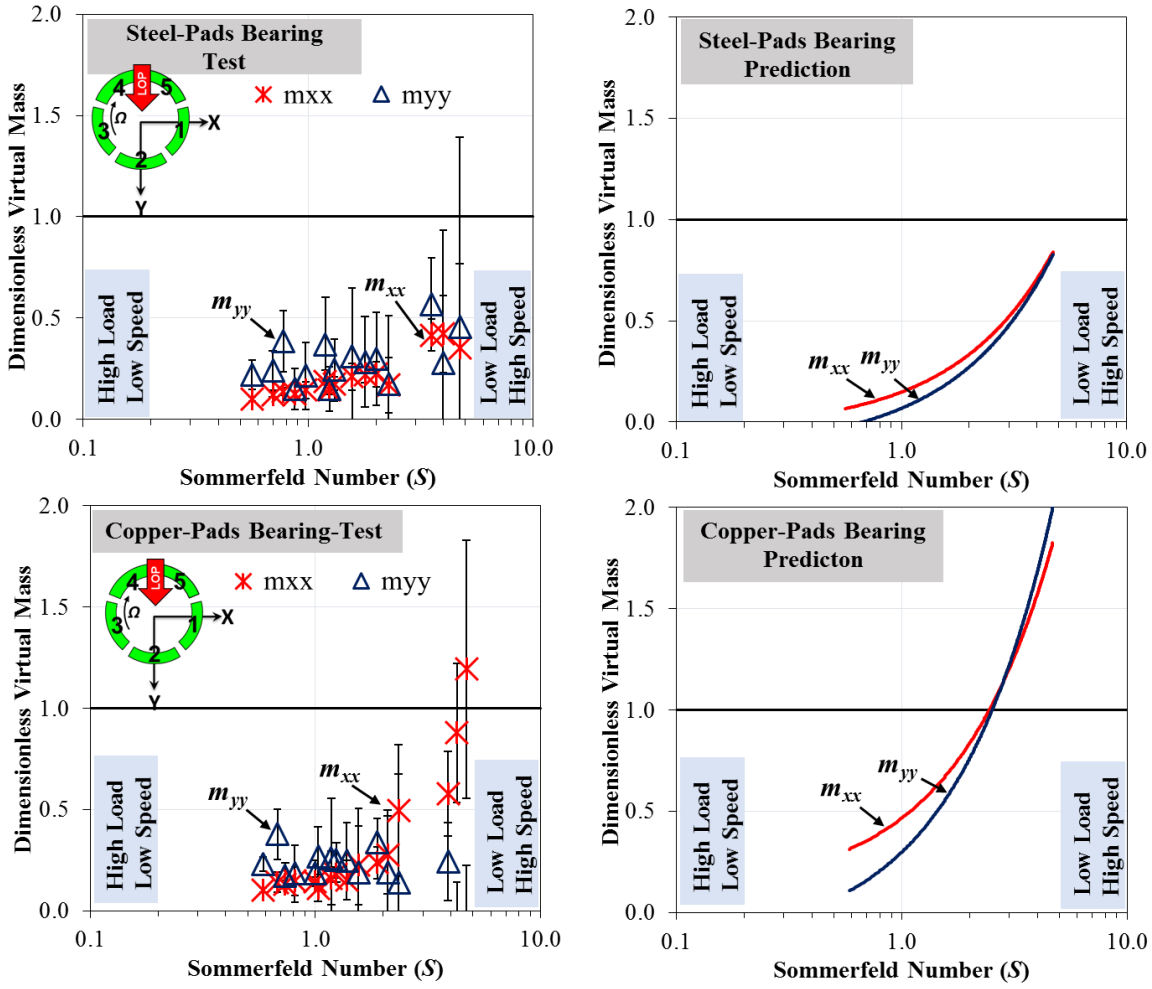

Figure 57 Experimental and predicted virtual mass coefficients (m_{xx}, m_{yy}) for (top) steel-pads bearing and (bottom) copper-pads bearing for operation at various shaft surface speeds (48-74 m/s) and specific loads (0.35-2.1 MPa).

8. CONCLUSION

The thesis presents measurements and compare the static and dynamic load characteristics of a copper-pads bearing (C-PB) vs. an identical steel-pads bearing (S-PB). Both bearings have five pads, 101.6 mm bearing nominal diameter, 0.4 *L/D* ratio, ball-in-socket pivot type, 50 % pivot offset, 63.5 µm nominal bearing radial clearance (C_b), and an average pad preload (*m*) of 0.42. The bearings operate at four shaft speeds ranging from 6 krpm (32 m/s) to 14 krpm (74 m/s) and multiple bearing specific loads ranging from (0.17 MPa to 2.1 MPa). ISO VG 32 oil, at a supply temperature of 49 ºC, lubricates the bearings under a flooded lubrication configuration.

The performance parameters revealing the static performance characteristics of a bearing include drag power loss, shaft eccentricity, attitude angle, oil discharge temperature, and pads' sub-surface temperatures.

A bearing shaft eccentricity depends significantly on the rotor speed and applied specific load. Moreover, similar to results presented by Pettinato et al. [16], the shaft eccentricity for both the bearings decreases with an increase in Sommerfeld Number. The test results show that at any operating point the C-PB shaft attains a lower shaft eccentricity than the S-PB shaft does. Over the range of operating conditions, the difference in *e* for both bearings shaft eccentricity is ~ 20 - 40 %. The attitude angles for both bearings are low (~ <10 º) at a majority of the operating speeds and load conditions.

The oil discharge temperature is a strong function of the shaft speed and does not depend on the applied load. The results show that the exit oil temperature difference between both bearings is not significant as the maximum temperature difference is ~ 6 º at an operating speed of 34 m/s and specific load of 2.1 MPa.

Since oil exit temperature and drag power are directly related, the measured power loss shows similar trends, i.e. the drag power loss increases significantly with an increase in shaft speed and is nearly independent of applied load. The power loss vs. shaft speed and vs. specific load trends are similar to the experimental results presented in Refs. [16, 23, 31]. A comparison of the results show that both bearings show an insignificant difference in power loss, i.e. no greater than 5 %.

The pad temperatures for both bearings highly depend on the operating shaft speed (at a constant load) and change little with specific load (at a constant shaft speed). A comparison of the C-PB and the S-PB pads temperatures show that, at the same operating condition, the S-PB pads operate at a higher temperature as compared to the C-PB. The maximum pad sub-surface temperatures for both bearings differ by ~15 %. Moreover, for operation at any shaft speed and applied load, the maximum pad temperature for both bearings is measured on loaded pad #2. Multiple past experimental studies on TPJBs, Refs. [11, 29, 31, 32, 41], show a similar dependency of pad temperatures vs. shaft speed and evidence that a copper-pads bearing operates cooler than a steel-pads bearing.

As the C-PB loaded pad operates cooler than the S-PB, the local film viscosity of the C-PB is higher than that of the S-PB, especially at the high load operation. For operation at specific loads > 1.0 MPa, the C-PB viscosity is ~ 10- 35 % higher than that of the S-PB. Thus, larger viscosity of the C-PB lubricant results in the lower shaft eccentricity and produces larger stiffness and damping coefficients. Oil viscosity is one of the factors influencing the stiffness and shaft eccentricity. Also, as discussed in Section 6, the *hot* clearance (HC) of the C-PB and the S-PB are not equal. The unequal HC of both bearing is also responsible for the difference in shaft eccentricity and stiffness.

The stiffness, damping and virtual mass coefficients represent the dynamic load characteristics of a bearing. The experimental results show that the dimensionless stiffness coefficients ($k_{xx,}$ k_{yy}) ~ K (C_b/W) for both the C-PB and the S-PB increases with an increase shaft speed and decreases with an increase in specific load. The C-PB offers higher stiffnesses along both x (k_{xx}) and y directions (k_{yy}). The C-PB k_{xx} is ~ 60-70 % higher than the S-PB $k_{xx,,}$ whereas the C-PB k_{yy} is ~ 15-30 % higher than that of the S-PB. Further, since both the bearings operate under a Load-On-Pad configuration, both the C-PB and the S-PB yield bearing stiffness orthotropy. However, the stiffness orthotropy is higher for the S-PB as compared to the C-PB. A bearing under LOP configuration has a smaller clearance between the pads and the rotating shaft along the load direction (y-axis) as compared to those along the unloaded orthogonal direction. The smaller clearance results in the bearing stiffness orthotropy ($k_{yy} > k_{xx}$).

A comparison of the derived (from static load) static stiffness k_{stat} and the stiffness k_{yy} (derived from dynamic load) shows that, for S-PB, k_{stat} is ~ 25-35 % smaller than k_{yy}; whereas for the C-PB, k_{stat} is ~ 15-30% smaller than k_{yy}. These k_{stat} vs. k_{yy} results are similar to those presented by Carter [40].

Similar to the direct stiffness coefficients, the dimensionless damping coefficients ($c_{xx,}$ c_{yy}) ~ ($C\ \Omega\ C_b/W$) also increase with an increase in shaft speed and decrease with an increase in specific load. The damping coefficients of both bearing show symmetry along the *x* and *y* directions i.e. ($c_{yy} \approx c_{xx}$). Along both the *x* and *y* directions the C-PB offers higher damping than the S-PB. The C-PB's c_{xx} is ~ 30-40 % and c_{yy} is ~ 20 % higher than the c_{xx} and c_{yy} of the S-PB, respectively.

The dimensionless stiffness (k_{xx}, $k_{yy,}$) and damping coefficients (c_{xx}, c_{yy}) for both bearings increase with an increase in Sommerfeld number. In 1999, Wygant [8] presents dynamic coefficients for a five-pad, spherical pivoted TPJB. Compared to the present study, the results from Wygant show similar trends in stiffness and damping coefficients vs. Sommerfeld number (*S*). However, Wygant's data shows that the stiffness along the load direction (k_{yy}) changes insignificantly with an increase in *S*.

The virtual mass (dimensionless) coefficients of both bearings are <1.0 though showing a high measurement uncertainty and low correlation. The coefficients of both bearings are positive and change little with an increase in specific load.

Both test bearings have similar drag power loss and oil exit temperature; however, the pad sub-surface temperatures for the C-PB are slightly lower than those of the S-PB. Based on the test results at the specific operating conditions, the C-PB is a better choice for an application involving high shaft surface speed as the pad temperatures are low. The S-PB bearing has a higher elastic modulus and can bear higher specific loads as compared to the C-PB. For operation at high specific loads and shaft speeds, the C-PB could have an excessive thermal crowing which can alter the characteristics of the bearing.

The better choice of bearings solely depends on a particular application. Both test bearings have dissimilar load carrying capacity and provide adequate stiffness and damping coefficients. Thus, both bearings can be utilized in variety of applications.

The current research include operating shaft speed ranging from 32 m/s to 74 m/s and applied specific loads up to 2.0 MPa. A future study to compare the static load and dynamic load characteristics of the C-PB and the S-PB involving higher specific load (> 2 MPa) and higher surface speed (> 74 m/s) would be beneficial as it would cater to the increasing demand for high power density turbomachinery.

REFERENCES

[1] Childs, D. W., 1993, "*Turbomachinery Rotordynamics: Phenomenon, Modelling and Analysis*," Chapter 3, John Wiley & Sons, Inc, pp. 183-192.

[2] Zeidan, F. Y., and Paquette, D. J., 1994, "Application of High Speed and High Performance Fluid Film Bearings In Rotating Machinery," Proc. 23rd Turbomachinery Symposium, The Turbomachinery Laboratory, Texas A&M University, September 13-15, Dallas, TX, USA, pp. 209-234. doi: 10.21423/R1N654. https://oaktrust.library.tamu.edu/handle/1969.1/163490.

[3] Brugier, D., and Pascal, M. T., 1989, "Influence of Elastic Deformations of Turbo Generator Tilting Pad Bearings on the Static Behavior and on the Dynamic Coefficients in Different Designs," ASME J. Tribol., **111**(2), pp. 364-371.

[4] Dmochowski, W., and Brockwell, K., 1995, "Dynamic Testing of the Tilting Pad Journal Bearing," Trib. Trans., **38**(2), pp. 261-268.

[5] Fillon, M., Bilgoud, J. C., and Frene, J., 1992, "Experimental Study of Tilting Pad Journal Bearings-Comparison with Theoretical Thermoelastohydrodynamic Results," ASME J. Tribol., **114**(3), pp. 579-587.

[6] Simmons, L. E. J., and Dixon, J. S., 1994, "Effect of Load Direction, Preload, Clearance Ratio, and Oil Flow on the Performance of a 200 mm Journal Pad Bearing," Trib. Trans., **49**(2), pp. 227-236.

[7] Wygant, K. D., Flack, R. D., and Barett, L. E., 1999, "Influence of Pad Pivot Friction on Tilting-Pad Journal Bearing Measurements—Part I: Steady Operating Position," Trib. Trans., **42**(1), pp. 210-215.

[8] Wygant, K. D., Flack, R. D., and Barett, L. E., 1999, "Influence of Pad Pivot Friction on Tilting-Pad Journal Bearing Measurements—Part II: Dynamic Coefficients," Trib. Trans., **42**(1), pp. 250-256.

[9] Coghlan, D. M., and Childs, D. W., 2017, "Characteristics of a Spherical Seat TPJB with Four Methods of Directed Lubrication- Part 2: Rotordynamic Performance," ASME J. Eng. Gas Turbines Power, **139**(12), pp. 122503-122513.

[10] Armentrout, W. R., and Paquette, D. J., 1993, "Rotordynamic Characteristics of Flexure-Pivot Tilting-Pad Journal Bearings," Trib. Trans., **36**(3), pp. 443-451.

[11] Dmochowski, W., Brockwell, K., DeCamillo, S., and Mikula, A., 1993, "A Study of the Thermal Characteristics of the Leading Edge Groove and Conventional Tilting Pad Journal Bearings," ASME J. Tribol., **115**, pp. 219-226.

[12] Leopard, A. J., 1976, "Tilting Pad Bearings-Limits of Operation," ASLE Lubrication Engineering, **32**(2), pp. 637-644.

[13] Nicholas, J. C., 2003, "Tilting Pad Journal Bearings With Spray-Bar Blockers and By-Pass Cooling for High Speed, High Load Applications," Proceedings of the 32nd Turbomachinery Symposium, The Turbomachinery Laboratory, Texas A&M University,September, Houston, Texas, USA, pp. 27-38. doi: 10.21423/R19S81. https://oaktrust.library.tamu.edu/handle/1969.1/163299.

[14] Abdollahi, B., 2017, "A Computational Model For Tilting Pad Journal Bearings: Accounting For Thermally Induced Pad Deformations and Improving a Feeding Groove Thermal Mixing Model," M.S. Thesis, Texas A&M University, College Station, TX, USA.

[15] Pettinato, B., and DeChoudhury, P., 1999, "Test Results of Key and Spherical Pivot Five-Shoe Tilt Pad Journal Bearings-Part II: Dynamic Measurements," Trib. Trans., **42**(3), pp. 675-680.

[16] Pettinato, B., and DeChoudhury, P., 1999, "Test Results of Key and Spherical Pivot Five-Shoe Tilt Pad Journal Bearings-Part I: Performance Measurements," Trib. Trans., **42**(3), pp. 541-547.

[17] Wygant, K. D., Flack, R. D., and Barett, L. E., 2004, "Measured Performance of Tilting-Pad Journal Bearings over a Range of Preloads—Part I: Static Operating Conditions," Trib. Trans., **47**(4), pp. 576-584.

[18] Wygant, K. D., Flack, R. D., and Barett, L. E., 2004, "Measured Performance of Tilting-Pad Journal Bearings over a Range of Preloads—Part II: Dynamic Operating Conditions," Trib. Trans., **47**(4), pp. 585-593.

[19] Kukla, S., Hagemann, T., and Schwarze, H., 2013, "Measurement and Prediction of the Dynamic Characteristics of a Large Turbine Tilting-Pad Bearing Under High Circumferential Speeds," ASME Proceedings, Paper No. GT2013-95074, pp. 1-12.

[20] Kukla, S., Hagemann, T., and Schwarze, H., 2013, "Measurement and Prediction of the Static Characteristics of a Large Turbine Tilting-Pad Bearing Under High Circumferential Speeds," ASME Proceedings, Paper No. GT2013-95074, pp. 1-12.

[21] Coghlan, D. M., and Childs, D. W., 2017, "Characteristics of a Spherical Seat TPJB with Four Methods of Directed Lubrication- Part 1: Thermal and Static Performance," ASME J. Eng. Gas Turbines Power, **139**(12), pp. 1-13.

[22] Tripp, H., and Murphy, B., 1985, "Eccentricity Measurements on a Tilting-Pad Bearing," Trib. Trans., **28**(2), pp. 217-224.

[23] Simmons, L. E. J., and Dixon, J. S., 1996, "Performance Experiments with a 200 mm, Offset Pivot Journal Pad Bearing," Trib. Trans., **39**(4), pp. 969-973.

[24] Zeidan, F. Y., and Herbage, B. S., 1991, "Fluid Film Bearing Fundamentals and Failure Analysis," Proc. 20th Turbomachinery Symposium, The Turbomachinery Laboratory, Texas A&M University, Houston, TX, USA, pp. 162-186. doi: 10.21423/R1D950. https://oaktrust.library.tamu.edu/handle/1969.1/163546.

[25] ASTM-B23, 2014, "Standard Specification for White Metal Bearing Alloys (Known Commercially as "Babbitt Metal")," ASTM International, West Conshohocken, PA, doi: 10.1520/B0023-00R14.

[26] Ettles, C. M., Knox, R. T., Ferguson, J. H., and Horner, D. D., 2003, "Test Results for PTFE-Faced Thrust Pads, With Direct Comparison Against Babbitt-Faced Pads and Correlation With Analysis," ASME J. Tribol., **125**(4), pp. 814-823.

[27] Thorat, M. R., Pettinato, B. C., and DeChoudhury, P., 2014, "Metal Temperature Correlations in Tilting Pad Journal Bearings," ASME. J. Eng. Gas Turbines Power, **136**(11), p. 112503.

[28] Kingsbury-Inc, "How to Estimate Babbitt Temperature," https://www.kingsbury.com/how-to-estimate-babbitt-temperature.

[29] Gardner, W. W., 1975, "Performance Tests on Six-Inch Tilting Pad Thrust Bearings," ASME J. Lubr. Technol., **97**(3), pp. 430-438.

[30] Mikula, A. M., 1988, "The Effect of Shoe-Backing Material on the Thermal Performance of a Tilting-Pad thrust Bearing," Lubr. Engg, **44**(12), pp. 969-973.

[31] Bouchoule, C., Fillon, M., Nicolas, D., and Barresi, F., 1995, "Thermal Effects In Hydrodynamic Journal Bearings Of Speed Increasing And Reduction Gearboxes," Proceedings of the 24th Turbomachinery Symposium, Turbomachinery Laboratory, Texas A&M University, Houston, Texas, September 26-28, pp. 85-96. doi: 10.21423/R1BW8C. https://oaktrust.library.tamu.edu/handle/1969.1/163469.

[32] Edney, S. L., 1995, "Pad Temperature in High Speed, Lightly Loaded Tilting-Pad Journal Bearings," Proc. 24th Turbomachinery Symposium, The Turbomachinery Laboratory, Texas A&M University, September 26-28, Houston, TX, USA, pp. 73-83. doi: 10.21423/R1GM2K. https://oaktrust.library.tamu.edu/handle/1969.1/163468.

[33] Galvatskih, S. G., 2003, "Evaluating Thermal Performance of a PTFE-Faced Tilting Pad Thrust Bearing," ASME J. Tribol., **125**, pp. 814-823.

[34] Zhou, J., Blair, B., Argires, J., and Pitsch, D., 2015, "Experimental Performance Study of a High Speed Oil Lubricated Polymer Thrust Bearing," *Lubricants*, **3**, pp. 3-13.

[35] Jani, H., Kaizar, H., and San Andres, L., 2016, "Internal Progress Report Texas A&M University #3," pp. 1-5.

[36] Jani, H., Kaizar, H., and San Andres, L., 2016, "Internal Progress Report Texas A&M University #4," pp. 1-5.

[37] Childs, D. W., and Hale, K., 1994, "A Test Apparatus and Facility to identify the Rotordynamic Coefficients of High-Speed Hydrostatic Bearings," ASME J. Tribol., **116**, pp. 337-343.

[38] Jani, H., 2018, "Measurements of The Static And Dynamic Force Performance On A Five-Pad, Spherical-Pivot Tilting-Pad Journal Bearing: Influence Of Oil Flow Rate," M.S. Thesis, Texas A&M University, College Station, TX, USA.

[39] San Andres, L., 2009, "Turbulence flow in thin film bearings : Characteristics and Modeling," Modern Lubrication Theory, Notes 08, Libraries Texas A&M University Repository, http://hdl.handle.net/1969.1/93248.

[40] Carter, C. R., 2007, "Measured and Predicted Rotordynamic Coefficients and Static Performance of a Rocker-Pivot Tilt Pad Bearing In Load-On-Pad and Load-Between-Pad Configurations," M.S. Thesis, Texas A&M University, TX, USA, College Station.